THE COUPLED EFFECTS OF ENVIRONMENTAL COMPOSITION, TEMPERATURE AND CONTACT SIZE-SCALE ON THE TRIBOLOGY OF MOLYBDENUM DISULFIDE

by

Harmandeep S. Khare

A dissertation submitted to the Faculty of the University of Delaware in partial fulfillment of the requirements for the degree of Doctor of Philosophy in Mechanical Engineering

Spring 2014

ProQuest LLC.
789 East Eisenhower Parkway
P.O. Box 1346
Ann Arbor, MI 48106 - 1346

THE COUPLED EFFECTS OF ENVIRONMENTAL COMPOSITION, TEMPERATURE AND CONTACT SIZE-SCALE ON THE TRIBOLOGY OF MOLYBDENUM DISULFIDE

by

Harmandeep S. Khare

Approved: _____
Suresh G. Advani, Ph.D.
Chair of the Department of Mechanical Engineering

Approved: _____
Babatunde Ogunnaike, Ph.D.
Dean of the College of Engineering

Approved: _____
James G. Richards, Ph.D.
Vice Provost for Graduate and Professional Education

I certify that I have read this dissertation and that in my opinion it meets the academic and professional standard required by the University as a dissertation for the degree of Doctor of Philosophy.

Signed: _____

David L. Burris, Ph.D.
Professor in charge of dissertation

I certify that I have read this dissertation and that in my opinion it meets the academic and professional standard required by the University as a dissertation for the degree of Doctor of Philosophy.

Signed: _____

Joshua L. Hertz, Ph.D.
Member of dissertation committee

I certify that I have read this dissertation and that in my opinion it meets the academic and professional standard required by the University as a dissertation for the degree of Doctor of Philosophy.

Signed: _____

Chaoying Ni, Ph.D.
Member of dissertation committee

I certify that I have read this dissertation and that in my opinion it meets the academic and professional standard required by the University as a dissertation for the degree of Doctor of Philosophy.

Signed: _____

Michael H. Santare, Ph.D.
Member of dissertation committee

This dissertation is dedicated to my parents

ACKNOWLEDGMENTS

I thank the Air Force Office of Scientific Research (AFOSR), the University of Delaware Office of Graduate and Professional Education, and the University of Delaware Department of Mechanical Engineering for financial support of this work.

I thank my dissertation committee, Dr. Joshua Hertz, Dr. Chaoying Ni and Dr. Michael Santare, for their support and contributions to this research and my graduate training. I thank the staff and members of the Keck Advanced Microscopy Facility, especially Dr. Fei Deng and Dr. Laurel Kegel for their time and effort in making available the microscopy instrumentation. I also thank the administrative staff at the Department of Mechanical Engineering, especially Lisa Katzmire and Lita Toto for all their work and support during the past six years. A very special thank you to Steve Beard for helping me mill and lathe all those *doozies*, for being accommodating of my incessant demands of the shop, for the music and trivia, conversations and friendship.

I thank Andy Korenyi-Both for valuable discussions and for providing the MoS_2 coatings used in this study, and to Alan Ponder for all his efforts and support to keep our AFM on its feet. A special thanks to the tribology community for the camaraderie, and for inciting, critiquing and facilitating research ideas over the years. I extend a very special thanks to all current and former members of the Materials Tribology Laboratory, for the invaluable discussions, collaborations, 80s music and above all, friendship. I thank all my friends here at Delaware, especially Ananth and Tulasi for their friendship through the years of graduate school.

I owe a debt of gratitude to my parents for their selflessness, sacrifice and support through the years. They have been an inspiration to me since before I knew what the word meant. I owe an equal measure of gratitude to my sisters, especially Baldeep, for her love, humor and steadfast support. I thank Shannen for all the love, laughter and optimism. Finally, I would like to express my heartfelt gratitude to my graduate mentor, Dr. David Burris for his unfaltering support, patience and encouragement of my graduate research and training during the last five years. His enthusiasm and dedication to tribology research is an inspiration which will remain a hallmark of my time in graduate school.

TABLE OF CONTENTS

LIST OF TABLES

LIST OF FIGURES

LIST OF ABBREVIATIONS

A6061	Aluminum 6061 Alloy (T6)
AES	Auger Electron Spectroscopy
AFM	Atomic Force Microscope/Microscopy
BSG	Borosilicate Glass
DMT	Derjaguin-Muller-Toporov
EDS	Electron Dispersive X-ray Spectroscopy
FIB	Focused Ion Beam
HOPG	Highly Oriented Pyrolytic Graphite
HTT	High Temperature Tribometer
JKR	Johnson-Kendall-Roberts
LFM	Lateral Force Microscopy
LVDT	Linear Variable Differential Transformer
MoO_2	Molybdenum (IV) Oxide
MoO_3	Molybdenum (VI) Oxide
MoS_2	Molybdenum Disulfide
PEEK	Polyether ether ketone
ppm	Parts Per Million (by volume)
PSD	Photo-sensitive Diode
PTFE	Polytetrafluoroethylene
RH	Relative Humidity
Sb_2O_3	Antimony Trioxide

SEM	Scanning Electron Microscope/Microscopy
$SrTiO_3$	Strontium Titanate
SWLI	Scanning White Light Interferometer
TEM	Transmission Electron Microscopy
XPS	X-Ray Photoelectron Spectroscopy
XRD	X-Ray Diffraction

ABSTRACT

Liquid lubricants are precluded in an exceedingly large number of consumer as well as extreme applications as a means to reduce friction and wear at the sliding interface of two bodies. The extraterrestrial environment is one such example of an extreme environment which has motivated the development of advanced solid lubricant materials. Mechanical systems for space require fabrication, assembly, transportation and testing on earth before launch and deployment. Solid lubricants for space are expected to not only operate efficiently in the hard vacuum of space but also withstand interactions with moisture or oxygen during the terrestrial storage, transportation and assembly prior to deployment and launch. Molybdenum disulfide (MoS_2) is considered the gold standard in solid lubricants for space due to its excellent tribological properties in ultra-high vacuum. However in the presence of environmental species such as water and oxygen or at elevated temperatures, the lubricity and endurance of MoS_2 is severely limited. Past studies have offered several hypotheses for the breakdown of lubrication of MoS_2 under the influence of water and oxygen, although exact mechanisms remain unknown. Furthermore, it is unclear if temperature acts as a driver solely for oxidation or for thermally activated slip and thermally activated desorption as well. The answers to these questions are of fundamental importance to improving the reliability of existing MoS_2-based solid lubricants for space, as well as for guiding the design of advanced lamellar solid lubricant coatings. This dissertation aims to elucidate: (1) the role of water on MoS_2 oxidation, (2) the role of water on MoS_2 friction, (3) the role of oxygen on MoS_2

friction, (4) the contribution of thermal activation to ambient-temperature friction, and (5) effects of length-scale. The results of this study showed that water does not cause oxidation of MoS_2. Water increases ambient-temperature friction of MoS_2 directly through a combination of both surface adsorption and diffusion into the coating subsurface. Thermally activated desiccation effectively dries the bulk of the coating, yielding low values of friction coefficient even at ambient humidity and temperature. Friction of MoS_2 decreases with increasing temperature between 25°C and 100°C in the presence of environmental water and increases in the presence of oxygen alone. At temperatures greater than 100°C, friction generally increases with temperature only in the presence of environmental oxygen; at these elevated temperatures, friction *decreases* with increasing humidity. The transition from room-temperature increase to elevated-temperature decrease in friction with increasing humidity is found to be a strong function of the contact history as well as coating microstructure. Lastly, the contribution of nanoscale tribofilms to macroscale friction was studied through nanotribometry. Friction measured on the worn MoS_2 coating with a nano-scale AFM probe showed direct and quantifiable evidence of sliding-induced surface modification of MoS_2; friction measured on the perfectly ordered single crystal MoS_2 was nearly an order of magnitude lower than friction on worn MoS_2. Although friction coefficients measured with a nanoscale probe showed high surface sensitivity, micron-sized AFM probes gave friction coefficients similar to those obtained in the macroscale, suggesting the formation of surface films *in-situ* during sliding with the colloidal probe. A reduction in friction is observed after annealing for both the nanoscale and microscale probes, suggesting a strong overriding effect of the desiccated bulk over surface adsorption in driving the friction response at these length-scales.

This dissertation is based mainly on the following peer-reviewed articles:

1. Surface and sub-surface contributions of oxidation and moisture to room temperature friction of molybdenum disulfide
   H.S Khare, D.L. Burris, *Tribology Letters,* 53(1), 329-336 (2014)

2. The effect of environmental water and oxygen on temperature-dependent friction of sputtered molybdenum disulfide
   H.S. Khare, D.L. Burris, *Tribology Letters*, 52(3), 485-493 (2013)

3. The extended wedge method: AFM friction calibration for improved error tolerance to AFM misalignment, tip-offset and blunt probes
   H.S. Khare, D.L. Burris, *Rev. of Sci. Instruments,* 84, 055108 (2013)

Chapter 1

INTRODUCTION

Tribology and the Importance of Lubrication

Complex mechanical systems consist of and rely on constituent subassemblies for the transmission of motion and power. Movement in these mechanical systems require relative motion between contacting bodies. These sliding interfaces introduce opportunities for frictional energy dissipation, surface failure and wear of the interacting materials.

Tribology is the study of materials in sliding contact and associated phenomena such as friction, wear, and contact mechanics, and includes the design and development of lubricants and bearing materials. The term tribology came to be widely known following 'The Jost Report' in 1966, which was constituted to investigate increasing failures in industrial machinery due to friction and wear, often causing substantial financial losses [1, 2]. The Jost Report, and several other findings that succeeded it highlighted the role of tribology in the efficiency and reliability of industrial machines. The cost of frictional losses to the US economy has since been pegged anywhere between several hundred million to several hundred billions of dollars annually. Rabinowicz [3] notes that most early authors severely underestimated the economic impact of tribological losses by ignoring cost of wear; the economic cost associated with the wear of materials, including cost of downtime and replacement has been projected to be as high as ten times the cost of frictional losses.

Although studies of friction and wear date back to the work of daVinci [3], friction and interfacial phenomena remain among the least appreciated or thoroughly understood of physical sciences. Friction is recognized as an interfacial force which resists mechanical motion. At the microscopic level, friction and wear between two bodies arises due to the mutual contact of their respective microscale asperities. A common strategy to reduce friction and wear at the interface is to reduce the likelihood of direct asperity contact during sliding. Lubricants such as oils and greases work by creating a physical barrier between the sliding surfaces, separating individual asperities and reducing the likelihood of wear. Furthermore, lubricants such as oils and greases impart a low shear strength interface at the sliding contact which also facilitates low friction coefficients. In the absence of effective lubrication (which can include contaminant and oxide layers) clean surfaces can adhere strongly resulting in high friction, surface failure, and eventual system failure.

The underlying goal of modern day tribology research is to identify the fundamental mechanisms of interfacial friction and wear of materials and mitigate their consequences through materials design. At the most fundamental level, macroscale friction and wear originates at the atomic and nano-scale. Understanding the atomistic and molecular origins of friction and wear of materials at the macro-scale has emerged as a key area for tribological advancement today. An understanding of friction and wear mechanisms across length-scales is a key prerequisite in the development of materials with reduced friction and wear.

Introduction to Solid Lubricants

Liquid lubricants appear in visible applications like the automobile and industrial machinery where the cost of failures is high. However, the added cost and complexity of pumps, chillers, filters, and plumbing in a lubricant system is not justified in nearly every other consumer product. Furthermore, there are applications where failures are disastrous but traditional lubrication strategies are precluded by environmental extremes. Space is one such example.

Soft solid films interposed between harder surfaces limit the interfacial shear strength and effectively lubricate the tribological contact; this solid lubrication strategy is employed in many demanding environments. The first solid lubricants were thin soft coatings of materials like PTFE and indium [4]. These thin solid lubricant coatings are functionally similar to liquid lubricants in that they reduce interfacial shear strength while the harder substrate limits the real area over which contact occurs. This effect however does not explain low *bulk* friction observed for PTFE and graphite and it initially remained unclear if low friction of unsupported solid lubricants conformed to existing theories of friction. Bulk lamellar shear, the solid analogue to fluid flow was for long the accepted model for low friction sliding.

An insight into this anomaly has been offered by several recent microstructural and chemical studies of solid lubricant surfaces which reveal the presence of highly ordered tribological films at the sliding interface. Tribological films are ubiquitous features of low friction sliding; they form in response to the tribological action between two sliding surfaces. They are formed either due to entrapment and consolidation of solid lubricant wear debris during sliding on the counter body, known specifically as *transfer films*; or as in *tribofilms,* due to mechano-chemical modification of the solid lubricant surface itself. These films have in general been

strongly correlated to tribological performance; thinner transfer films are often more coherent and achieve higher friction and wear performance [5-11]. It is widely hypothesized that transfer films reduce wear rates of solid lubricants by acting as barriers to abrasion against surface asperities. Sawyer [12, 13] further showed that the surfaces created by these films are fantastically stable (100's of cycles for a single atomic layer to be removed) even during environmental transitions where friction coefficients increase by an order of magnitude. This is in direct contrast with the bulk lamellar shear model of conventional wisdom. The ability of tribological films formed during sliding to reduce friction coefficients across the interface is widely attributed to 'interfacial sliding' [14]; films once formed provide a lower shear strength interface which sustains low coefficients of friction across the interface [15, 16]. Recent nanomechanical and high resolution electron imaging studies have also confirmed the presence of highly anisotropic tribofilms the thickness of a few tens of nanometers, present on the surface of low friction nanocomposite solid lubricants [17-19]. Given the relative length-scales of tribofilms, solid lubricants and the bulk substrate, the tribofilms may be viewed as the superficial lubricant layer above the solid lubricant 'substrate', since the chemical and/or microstructural heterogeneity of tribofilms is expected to render them with vastly different mechanical properties.

While the importance of tribofilms to low friction and low wear solid lubricants has been established, there remains a lack of understanding of the properties and functional mechanisms of these films. This lack of understanding is underscored by the fact that most studies probe the chemical and compositional structure of tribofilms; an effort at characterizing mechanical properties of these thin films and their role on macroscale friction and wear has thus far been lacking.

Solid Lubricants in Extraterrestrial Environments

Mechanical systems for space application require fabrication, assembly and testing on earth before launch and deployment. Although the operational kinematics of these sub-assemblies remain unchanged between terrestrial and extra-terrestrial operation, the latter occurs in the absence of atmospheric pressure and constituents such as water vapor and oxygen. The lack of atmospheric pressure precludes the use of conventional lubricants – liquid lubricants such as oils desorb and evaporate in a hard vacuum environment, leaving behind bare, unlubricated interfaces which would quickly seize. This has motivated the development of a variety of solid lubricants, most notably surface coatings of materials such as molybdenum disulfide [20].

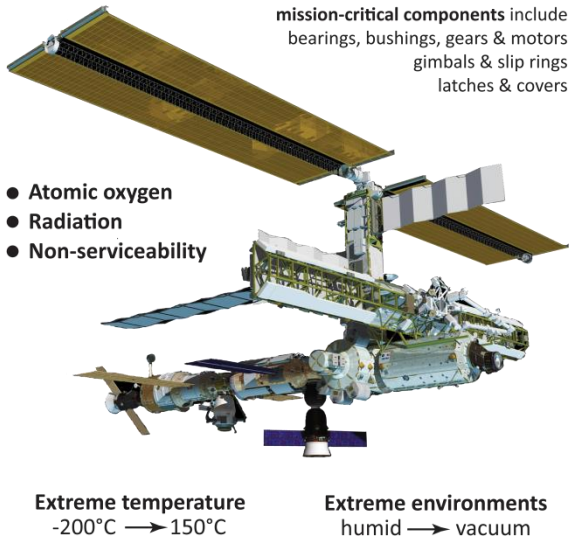

Figure 1 Successful operation in space presents several tribological challenges, as illustrated *(image source: NASA).*

Many solid lubricants have been shown to exhibit strong tribological sensitivity to the operating environment. For example, lubrication by graphite is benefitted from the presence of moisture in the environment. Friction coefficients of graphite may reduce by an order of magnitude or more with the introduction of water vapor, presumably due to the weakening of the π-bond interactions across individual lamellae [21]. In contrast, lubrication in molybdenum disulfide is benefitted from the *absence* of environmental contaminants, which make it the gold standard for space lubrication. The operational challenge arises due to the fact that space components are fabricated, tested, transported and launched in the presence of atmospheric contaminants, but deployed and operated in their absence. As a consequence, solid lubricants which give exceptional performance in space run the risk of premature damage during pre-launch assembly and testing. A classic example of this was the failure of the high-gain antenna of the Galileo spacecraft, which was later determined to have been caused by pre-launch storage and transport of environmentally-sensitive bearings [22].

Together with environmental contamination, space vehicles are also subject to a wide range (often ±100°C) of thermal extremes, occurring during launch and re-entry, as well as during orbit. This is in addition to challenges of material and functional degradation by atomic oxygen, cosmic radiation and the long service lifetimes necessitated by inaccessibility for replacement and repair. The key challenge in the design of bearing materials for such demanding applications is an understanding of both the mechanisms of lubrication as well as the mechanisms responsible for the breakdown of lubrication.

Chapter 2

MOLYBDENUM DISULFIDE AS A SOLID LUBRICANT

Molybdenum disulfide (MoS_2) is a member of the family of transition metal dichalcogenides (TMD), which includes other solid lubricants such as molybdenum diselenide, and tungsten disulfide and diselenide. Generally, TMDs are of the form MX_2, where M is any of the transition metals Mo, W, Nb or Ta and X is any of the group16 elements S, Se or Te [23]. As shown in figure 2, MoS_2 exhibits a hexagonal, layered lattice structure where each $Mo^{(4+)}$ occupies the center of a trigonal prismatic geometry, while each $S^{(2-)}$ occupies the apex of a pyramidal geometry and is connected to three molybdenum atoms [24-26]. In this layered lattice structure, the strong S-Mo-S covalent bonding alternates with a weak S-S van der Waals bond; the easy shear at the S-S plane is credited with the low shear strength and thus, lubricious nature of basally oriented MoS_2 [26, 27]. The basal-slip mechanism of MoS_2 lubrication is often compared to a similar mechanism in graphite, however while graphite requires the presence of intercalated species (such as water) to reduce the shear strength across its basal planes, easy shear is intrinsic to MoS_2 [21, 24].

MoS_2 has been used as a solid lubricant since before the 20^{th} century although interest in MoS_2 lubrication was renewed in the mid-20^{th} century in large part due to its unique ability to provide low friction in evacuated environments. The ability of MoS_2 to sustain ultra-low friction in vacuum made it an ideal candidate for lubrication in space; expectedly, some of the pioneering work into understanding the tribology of

MoS_2 was carried out by governmental organizations such as the USAF and NACA (later as NASA) [24].

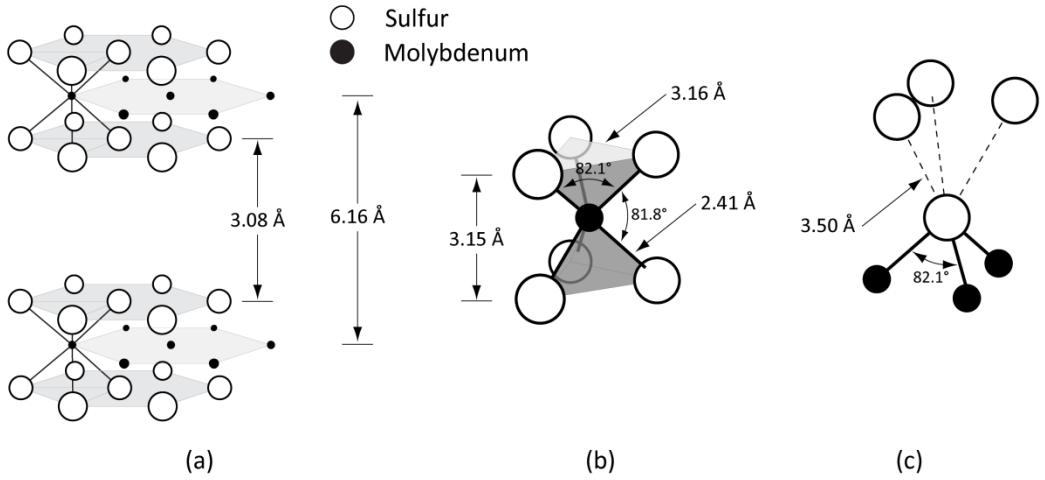

Figure 2 MoS_2 exhibits a hexagonal layered lattice crystal structure where each molybdenum atom is equidistant from six sulfur atoms. The large inter-lamellar distance (0.31nm) enables easy lamellar shear in MoS_2.

Through the mid-20th century, tribological studies of MoS_2 were performed on films which may broadly be classified as either bonded or unbonded. Unbonded films were formed either by evaporating MoS_2 solutions applied onto surfaces or by the mechanical 'rubbing' of pulverized MoS_2 powder on the sliding surface. Bonded films traditionally consisted of MoS_2 mixed with a resin paste, which was applied on the sliding surface followed by high temperature curing to form an adherent film [28-32]. Although resin-bonded MoS_2 films are in use to the present day, a significant development in the synthesis of adherent MoS_2 solid lubricant films came with the advent of advanced deposition methods, such as chemical and physical vapor

deposition in the 1980s [25, 33-38]. Sputter deposition not only improved the adhesion of MoS_2 coatings to the substrate, but also helped drive fundamental research into the role of MoS_2 microstructure on its tribology. From the early beginnings of sputter-deposition, variations were observed in the tribological properties of MoS_2 as direct consequence of the deposition technique or deposition parameters. An extensive body of research has been dedicated to understanding the effects of deposition parameters and conditions which lead to improved lubrication, as well as those which cause higher friction and rates of wear.

MoS_2 lubricity shows a strong dependence on the operating environment and temperature, which has presented a challenge to the reliability of systems employing MoS_2 as a bearing material. MoS_2 is known to sustain ultra-low friction and wear in clean environments, such as ultra-high vacuum although it is known to break into high friction in the presence of moisture [16, 26]. Although several hypotheses have been proposed to explain the breakdown of lubrication in certain environments, as will be later discussed, exact mechanisms remain unclear. Hybrid MoS_2 solid lubricant nanocomposites have also been recently developed and show reduced friction and wear sensitivity to the operating environment [17, 39]. Nevertheless, understanding lubrication and failure mechanisms in MoS_2 is critical to understanding design limitations.

Tribofilms and Interfacial Friction

Easy shear along the S-S basal plane of MoS_2 is widely credited with its ability to sustain ultra-low friction, as noted earlier. Most applications of MoS_2 however employ a polycrystalline form of MoS_2 where individual grains are often randomly oriented within the MoS_2 coating, without preferential orientation of the basal planes.

A mechanism of reorientation is often hypothesized where sliding across the MoS_2 coating with disordered grains leads to the formation of highly oriented grains, aligned with the direction of sliding. Once aligned, these basally-oriented surface layers, also known as *tribofilms* sustain the easy shear that results in the ultra-low values of friction typical of MoS_2.

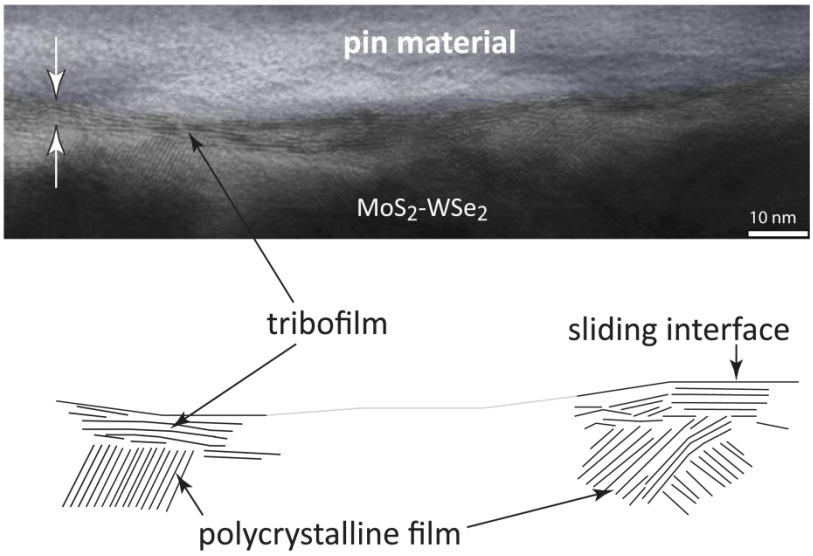

Figure 3 An *in-situ* TEM image of a sliding interface. Sliding causes the reorientation of interfacial grains, thus forming a thin surface tribofilm (adapted from [18]).

Several authors have recently suggested the role of oriented tribofilms and incommensurability of MoS_2 in achieving low friction [40]. For a MoS_2-WSe_2 composite coating, Hu *et al.* [18] demonstrated the presence of tribofilms at the sliding interface of an immobilized contact, as shown in figure 3. After sliding a silicon carbide pin on the surface of the coating, the contact was welded in place and the tip

then sectioned off using a FIB mill. Subsequent to a lift-out procedure, observing the frozen contact under a TEM clearly demonstrates the presence of a very thin (~10nm) surface tribofilm at the contact. These tribofilms have been hypothesized to accommodate interfacial shear in tribological contacts, although a direct probe of the properties of tribofilms has not been made.

Effect of Water on MoS_2 Tribology

A characteristic feature of MoS_2 lubrication is its sensitivity to the sliding environment, in particular the presence of moisture. Operation in the hard vacuum of space precludes any direct interaction of MoS_2 with moisture, however storage, transportation and assembly of spacecraft components after coating deposition and before deployment offers numerous opportunities for such an interaction. During this period, the MoS_2 coating may be subject to long durations of varying water vapor concentrations (during storage), mechanical strains due to fretting (transportation and pre-launch testing), as well as thermal fluctuations during lift-off, orbital flight and re-entry. Orbital operation of coatings previously exposed to moisture in the terrestrial environment run the risk of premature failure, jeopardizing mission success. The failure of the high gain antenna in the Galileo spacecraft is one such example, where premature failure of the bearings during deployment was traced to prolonged storage and transportation of the spacecraft components [22]. As a result, understanding mechanisms that drive breakdown of lubrication on earth is critical to successful operation in space.

Variable environment and variable humidity studies spanning several decades show that dry sliding friction of MoS_2 increases with increasing partial pressure of water in the sliding environment [24]. The frictional sensitivity to moisture has been

observed irrespective of the film deposition method. In spite of the universal observation of increased friction with increasing humidity, there is a lack of agreement about the mechanisms driving such an increase in friction. Mechanisms proposed to explain the increase in friction with humidity are broadly classified into two categories – one where water promotes the formation of high friction oxides and the other where water physically disrupts lamellar shear. With the oxidation hypothesis, exposure of MoS_2 to water vapor in the sliding environment ostensibly leads to the formation of MoO_3, usually at the grain boundaries which disrupts the easy lamellar shear of MoS_2 thereby causing increased friction. Ross and Sussman [41] were among the first authors to propose the ability of water to cause oxidation of MoS_2. Using a method of calorimetric determination, they studied the formation of surface oxides in low humidity (at 100°C) and high humidity (at 85°C) and observed that a higher humidity environment caused the formation of greater MoO_3. Haltner and Oliver [42] measured friction at various partial pressures of water and observed an increase in friction with increasing water vapor. They postulated that water causes the oxidation of MoS_2 to MoO_3, together with the release of SO_2 and H_2S. It was hypothesized that flash temperatures due to frictional heating at the real asperity contact facilitate the required rates for such a reaction. In measurements of friction of cured films of MoS_2 in humid environments by Pardee, an increased friction with humidity was attributed to the formation of the oxide MoO_3 [43]. Pardee hypothesized that low shear-strength layers of MoS_2 successively oxidize to high shear-strength layers of MoO_3 instantaneously at mechanically activated surfaces, resulting in high friction. Panitz observed increased friction of RF-sputtered MoS_2 coatings after prolonged storage in humid environments which was attributed to the water-driven oxidation of MoS_2 lattice edge sites [44].

Stewart and Fleischauer [45] used a combination of AES and XPS to detect oxidation of RF-sputtered MoS_2 in humid environments. They found evidence of accelerated oxidation, presumably at the grain boundary reaction centers [46] in the presence of excess water vapor, which caused deterioration of the lubricating properties of MoS_2 films. More recently, a study by Dudder *et al.* probed the environmental dependence of a MoS_2-Sb_2O_3-C composite coating [47]. Friction was measured in vacuum, humid air and in environments with either only oxygen or only water; additionally, surface chemistry was probed using XPS. For the composite coating, it was shown that friction coefficients increased in water and air, but remained low in oxygen and vacuum, suggesting that water was responsible for the frictional increase. The authors note that although frictional increase in humid environments was likely driven by tertiary components (such as Sb_2O_3) rather than oxides expressing at the surface, between oxygen and water environments, the latter was most likely to bring about whatever little oxidation did occur.

Several other studies suggest that water increases MoS_2 friction through mechanisms which do not rely on the water-driven formation of oxides. Midgely [31] measured friction on thick (500μm), unbonded MoS_2 films formed by applying an MoS_2 suspension in ethyl alcohol to bearing surfaces of steel. A decrease in friction with increased sliding cycles was attributed to the drying of the MoS_2 surfaces due to frictional heat, suggesting that water is physically adsorbed at the sliding interface. Johnson and Moore [48] measured changes in the mass of a pulverized MoS_2 sample when exposed to air with varying values of relative humidity. They found evidence of water being both physisorbed and chemisorbed on MoS_2; changes in mass only due to physisorbed water could be reversed by reversing the humidity of the environment.

Roberts measured changes in friction of RF-sputtered MoS_2 in order to elucidate the dependence of friction on sputtering conditions and environment [35]. Low friction was observed in a vacuum environment, into which water vapor was slowly introduced. Friction coefficient of the MoS_2 coating was observed to abruptly increase at two distinct water partial pressures which Roberts attributed to the physisorption of water to two distinct sites in the lattice with differing heats of adsorption. After re-establishing vacuum, low friction was only partially recovered and the residual increased friction was attributed to adsorption at the site of the higher heat of adsorption. Holinski and Gänsheimer [49] credited the increases in MoS_2 friction in the presence of water vapor to the strong polarity of sulfur in MoS_2. It was suggested that water adsorbs to the highly polar sulfur surface through a hydrogen bond linkage, disrupting the nominally easy shear at the S-S interface and thereby increasing friction. The increase in the water partial pressure (relative humidity) was hypothesized to directly increase the quantity of water available for adsorption, leading to the increased friction. Several other authors have performed sliding experiments where the environment is cycled between a dry state and a wet state [50, 51]. These 'pump and purge' experiments with MoS_2 or MoS_2 composites coatings show an almost instantaneous response to the change in environment (high friction for humid and low friction for dry), suggesting a reversible adsorption-desorption process in favor of an irreversible process like oxidation.

Effect of Temperature on MoS_2 Tribology

In general, friction of MoS_2 is observed to increase with increasing temperature of the interface [24]. Godfrey and Nelson [52] determined rates of oxidation of a compacted MoS_2 sample using XRD and also measured friction on a

resin-bonded MoS_2 coating at elevated temperatures. Rates of oxidation of MoS_2 were observed to be low below 400°C in air and 540°C in vacuum, with appreciable rates observed above 550°C in air. It was noted that MoS_2 oxidation is a function of temperature, exposure time, and oxygen concentration. Sliney showed that friction coefficients of resin-bonded MoS_2 only increased above 400°C in air and 600°C in argon [53-55]. Muratore et al. [56] made in situ Raman spectroscopy measurements of a sputtered MoS_2 coating during sliding in air and observed the appearance of an MoO_3 Raman intensity peak with an abrupt increase in friction at 350°C. These results suggest a direct relationship between friction and oxidation. Other studies have observed distinct transitions in the frictional response to temperature. Kubart *et al.* [57] noted that increasing temperature of a sputtered MoS_2 coating initially decreases the friction, followed by a subsequent increase. These measurements were made in an ambient humidity environment and the initial decrease was attributed to a 'reduced relative humidity of the environment surrounding the coating', while the higher friction at higher temperatures was attributed to oxidation. Similar trends of frictional increase following an initial reduction have been reported by other authors [58]. Interestingly, frictional studies at elevated temperatures have only been conducted in either an absence or surplus water vapors – the effect of varying humidity on the temperature-dependent friction of MoS_2 remains unknown. Furthermore, it is unclear if temperature acts as a driver for oxidation or thermally activated friction reduction [59].

Lubrication Mechanisms: Motivation for Current Studies

Despite the decades of research, several fundamental questions about the tribological response of MoS_2 to humidity remain unanswered. The answers to these

questions are of fundamental importance to improving the reliability of existing MoS_2-based solid lubricants for space, as well as for guiding the design of advanced lamellar solid lubricant coatings. This dissertation aims to elucidate the tribological mechanisms responsible for MoS_2 lubricity and their limitations.

Chapter 3

FRICTION AND WEAR IN MATERIALS

Background: Adhesive Theory of Friction

The history of tribology as a science traces its origins to the study of friction by da Vinci in the 15th century when through a series of experiments, he observed that 'frictional effort' was directly proportional to the applied normal load and was independent of the contact area between sliding bodies. Amontons in the 17th century formulated these observations into what are now the first two laws of friction. The mechanism of friction was proposed to stem from an interlocking of microscopic asperities on the surface of sliding materials, as shown in figure 4.

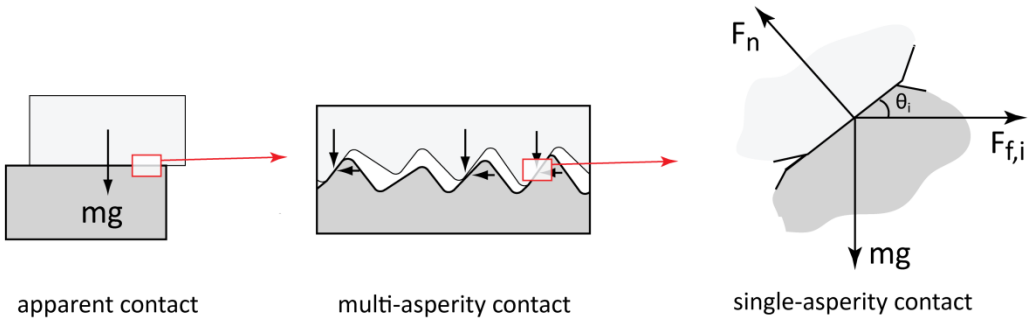

Figure 4 An illustration of the asperity interlocking mechanism of friction proposed by Amontons.

Friction was described as the effort that was required to overcome the interlocking across the peaks and valleys of two mated surfaces, thus explaining the

dependence on normal loads and the independence of contact areas. In 1734, Desanguliers hypothesized the contribution of adhesion between contacting surfaces to the measured force of friction. Given the theoretical dependence of adhesion on contact area and the observed independence of friction on area (daVinci's experiments), the adhesion hypothesis was rejected in favor of the conventional 'asperity interlocking' mechanism [3]. Pump-purge studies in the 1920's showed that friction increased by an order of magnitude when the environmental gasses were removed. These results helped reject the roughness hypothesis on the basis that the environment has no effect on roughness. Only the adhesion hypothesis could explain this result but it remained unclear how friction could be proportional to load and independent of area in such a model. It was not until the mid-20th century and the pioneering work of Bowden and Tabor that the contributions of adhesion were elucidated.

Bowden and Tabor measured contact resistance across the interface and showed that the resistance decreased when the load was increased [60]. They proposed that the 'real' contact area is very small when compared to the 'apparent' contact area because surfaces are rough and meet only at the highest opposing asperities. Further, due to the small contact areas, the contact pressures at these asperities are significantly higher which causes them to deform plastically to accommodate the impressed loads. At the contact of a hard and a relatively softer body, the effect of increasing load is to cause a proportional increase in the real contact area, due to deformation of the softer body. Archard showed this relationship held even for elastic contacts when increased loads bring more asperities into contact rather than increase the areas of existing contacts [61]. As an illustration, real-contact area measured *in-situ* between a ¼"

diameter polyethylene ball and a glass slide is shown in figure 5. Although apparent contact between a sphere and a flat surface would appear to be a circle, the real contact consists of discrete patches which grow in size and number with increasing normal load. As in figure 5, the real contact area is found to be much smaller than the apparent contact area.

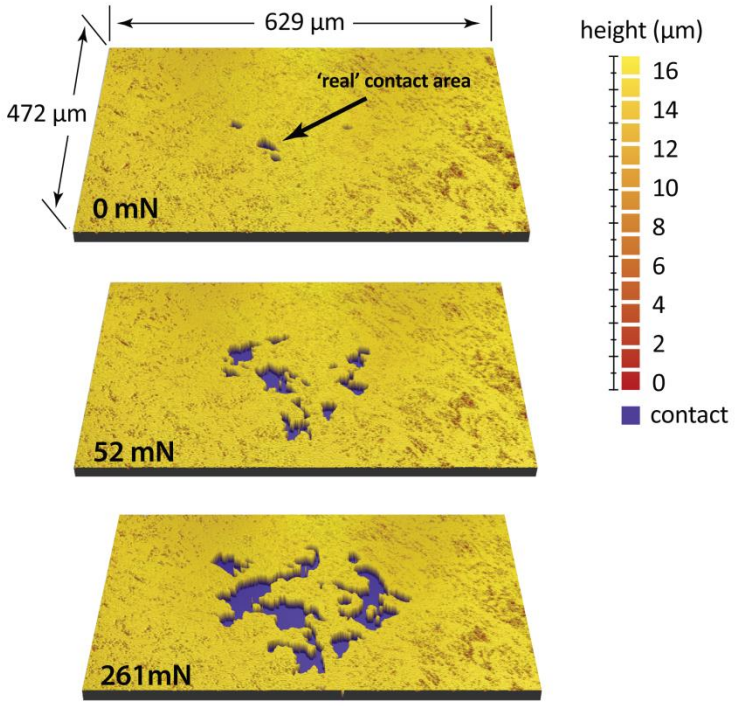

Figure 5 In-situ measurement of real contact area between a ¼" polyethylene ball indenting on a glass slide. Increase in normal load causes an increase in the real contact area (shown in purple).

When sliding motion is imposed on these loaded asperities, the shear strength of asperity junctions acting over the 'real' contact area produces the adhesive force of

friction. Bowden and Tabor's work on the adhesive theory of friction not only helped elucidate the contact mechanics of the sliding interface, but their work also underlined the importance of surface mechanics in tribology. Friction coefficient is usually defined as the ratio of the friction force and normal load. Friction at a contact area *A* due to a shear stress τ can be written as $F_f = \tau \cdot A$; the contact area of two bodies in contact is governed by the hardness, given by $H = F_n/A$. From these two expressions, the friction coefficient ($= F_f/F_n$) can be rewritten as:

$$\mu = {}^{\tau}/_{H}$$

Recognizing that shear strength is roughly 0.5 times the yield strength [62], and hardness is thrice the yield strength [63]; we see that $\mu \approx 0.2$. With progressive sliding, due to the asperities having already been plastically deformed, the contact area increases in what is known as junction growth, causing the contact area and friction coefficient to increase [4]. An enormous number of systems have been shown to initiate sliding at friction coefficients around this theoretic estimate before increasing due to contributions from junction growth, ploughing and debris.

Figure 6 shows the surface evolution of a steel flat when slid against a steel ball [13]. Initially, the friction coefficient is around 0.25 and increases rapidly as protective surface contaminants and oxides are removed. At cycle 50, the friction coefficient is significantly higher and the surface is characterized by pits from cohesive failure and the resulting debris. By 125 cycles, large-scale cohesive failure is evident, resulting in wear track growth and drastically increased friction.

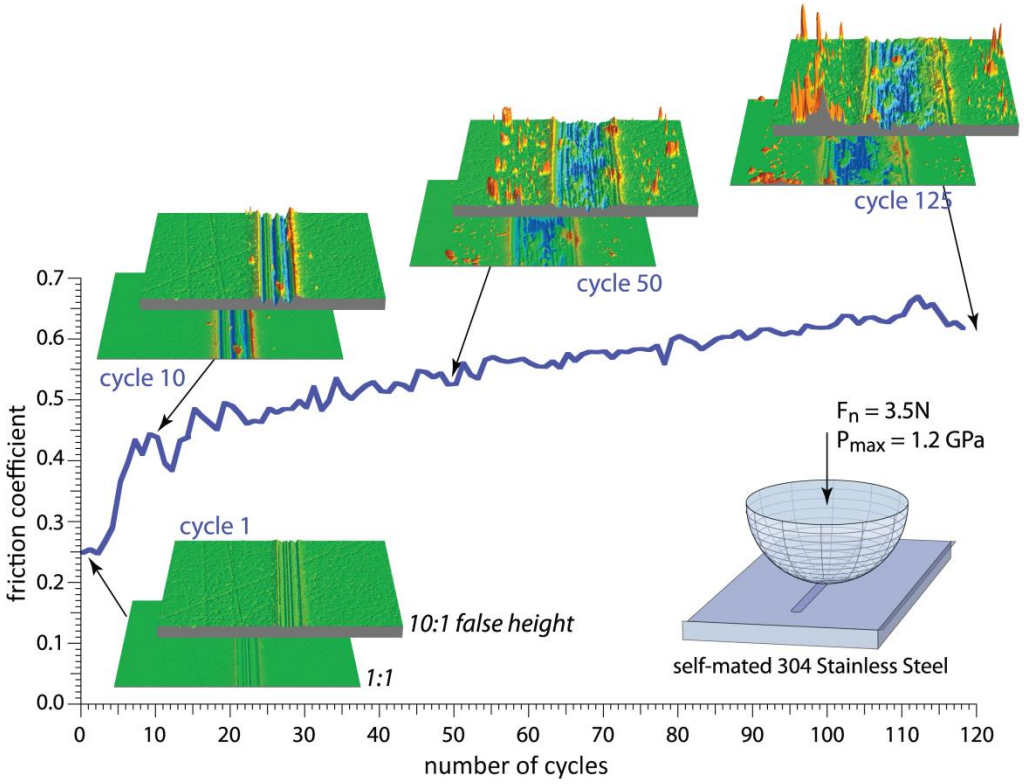

Figure 6 Steel-on-steel un-lubricated sliding shows starting friction coefficients of ~ 0.25 which quickly increase due to contributions from junction growth and cohesive welding/failure [13].

A broad range of polymers, metals and ceramics begin to slide at friction coefficients above 0.2 and increase over time to a steady state value; this behavior is well-explained by modern friction theories. The adhesive theory suggests that friction can be reduced by increasing substrate hardness while limiting the shear strength at the interface. It is this very interfacial shear strength that is limited by boundary lubricants like oils and greases; the rationale is that the substrate resists deformation and limits the contact area while the lubricant limits shear strength.

Elastic Contact Mechanics

The contact of two opposing bodies, even in the absence of interfacial shear leads to subsurface stress and deformations with finite contact geometries and poses a classical mechanics problem for which various mathematical models and solutions have been postulated. The most fundamental of these was given by Hertz for the contact of a sphere on an elastic half-space, in the absence of any surface forces [64]. The Hertzian contact model provides mathematical expressions for determining contact parameters of ball-on-flat elastic contacts. Three quantities most relevant to tribological contacts, as defined by the Hertz model [65] are:

$$Contact\ radius = \sqrt[3]{3PR/4E_r} \tag{1}$$

$$Indentation\ depth = \sqrt[3]{9P^2/16RE_r^2} \tag{2}$$

$$Mean\ contact\ pressure = 0.67 \cdot \sqrt[3]{6PE_r/\pi^3 R^2} \tag{3}$$

Where P is the applied normal force, E_r is the reduced modulus and R is the radius of the effective sphere. Real interfaces however are subject to non-zero surface forces. The two most widely used contact models which take into account surface adhesion are the Johnson-Kendall-Roberts (JKR) and the Derjaguin-Muller-Toporov (DMT) models of elastic contact [66]. Both JKR and DMT models are derived from the Hertz contact model, however they differ in their treatment of surface forces – the DMT model proposes that long-range adhesive forces act outside the area of contact, giving rise to tensile stresses whereas in the JKR model, adhesive forces and all associated stresses act within the area of contact. The DMT model is applicable in stiff

materials with low surface energy, whereas the JKR model is applied to soft materials with high surface energy [66].

Single and Multi-Asperity Contact

At the most fundamental level, macroscale friction originates due to a combination of elastic and inelastic atomic-scale interactions of surfaces in relative motion. A simplified, one-dimensional model of this interaction in the absence of stresses and deformation was described first by Prandtl in 1928 and later in 1929 by Tomlinson, commonly referred to as the 'Prandtl-Tomlinson' model of dry friction [67-69]. This model envisages the relative motion between a single atom against a surface, which is represented in the form of its energy landscape, consisting of energy peaks and valleys. When the atom is translated across this surface with a constant velocity, energetics favor the settling of the atom into the lower 'energy wells'; when the spring force exceeds the local energy derivative with respect to position (i.e. the local adhesive force), the atom breaks away and suffers slip. As a result, the atom undergoes periods of intermittent sliding due to displacement from a local energy maxima to a local energy minima, and stiction caused by the 'entrapment' of the atom in a local energy minima – this gives rise to 'atomic stick slip' motion.

Realistic single asperities, even those with sub-nanometer radii consist of many atoms. These individual asperities exhibit the $2/3^{rd}$ power law relationship between contact area and normal load, as postulated by Hertz. Archard noted that in a contact where increasing load increases the number of contacting asperities, contact area trends linearly with normal load even during elastic deformation. In practical systems however, the normal loads experienced by individual asperities are rarely small enough to justify a purely elastic contact; instead, these lead to the plastic deformation

of individual asperities. Additionally, the application of an increasing normal load causes a greater number of individual asperities to come into mutual contact, several of which also undergo plastic deformation leading to a growth in the overall *real contact* area. Although ideal single asperity contacts can be simulated under controlled laboratory conditions, for instance with the Atomic Force Microscope, nearly all interfaces larger than the atomic scale are in fact multi-asperity contacts. The contribution of nano- and micro-scale adhesion, abrasion, plastic deformation, junction growth and fracture at the multi-asperity contact between rough surfaces contribute to the macroscale observations of friction and wear.

Tribological Characterization

Single asperity contacts

Originally used as a tool for measuring the topography of surfaces with a sub-nanometer resolution, the Atomic Force Microscope (AFM) has since been extensively used for measuring interfacial forces and characterizing mechanical properties at the nanoscale. The earliest example of an AFM study of friction at the nanoscale was carried out by Mate *et al.* [70]. Mate *et al.* showed that a nanoscale tungsten stylus sliding across an atomically flat surface of highly oriented pyrolytic graphite (HOPG) gives rise to a characteristic saw-tooth stick-slip pattern of the lateral deflection signal, shown in figure 7. The periodicity of the peaks and valleys correspond to the lattice spacing of the surface.

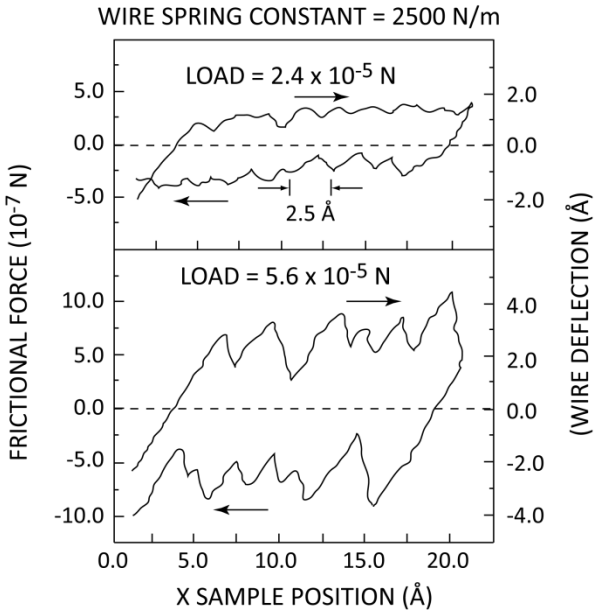

Figure 7 These friction loops obtained on a graphite surface with a tungsten probe were the first demonstration of atomic stick-slip (*adapted from* [70]).

The schematic of a typical AFM is shown in figure 8. The essential components of AFM sensing include a laser source, a microfabricated cantilever, guide mirrors and a photosensitive diode (PSD), together with the electronics interface. The primary component of motion control in an AFM is the piezoelectric stage, which is used for precise translation along any or all three axes of motion. Changes in the normal force applied at the probe-end of the cantilever, either due to vertical translation of the piezo or due to topography encountered on the scanned surface cause the cantilever to bend about the fixed end in the normal direction. A normal deflection at the free end of the cantilever causes the reflected laser spot on the PSD to shift in proportion to the slope of the cantilever free end, which is proportional to the force applied. In closed-loop AFM scanning, the tip-surface force is maintained at a constant ‘set-point’ value, specified by the user.

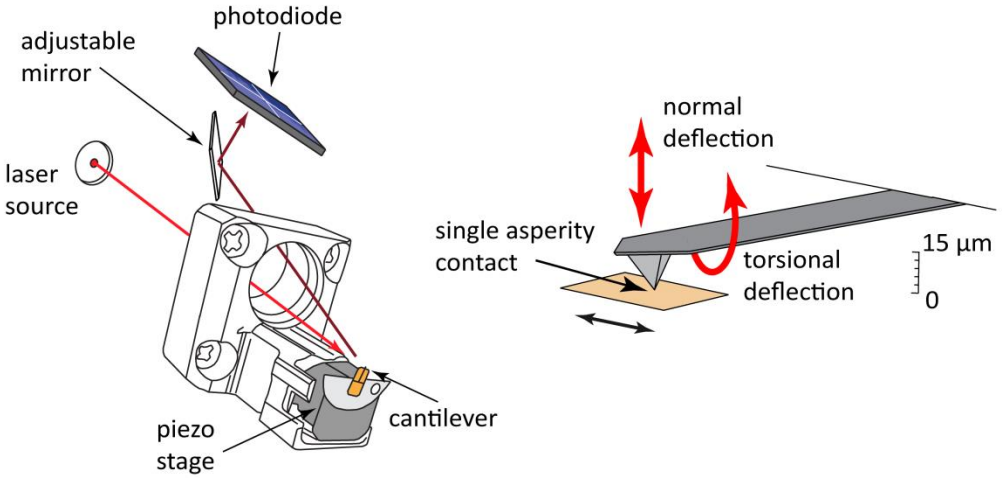

Figure 8 A schematic illustration of key components of the atomic force microscope. Interfacial friction at the tip creates a torsional moment, which is registered as lateral deflection on the PSD.

Changes in this force due to changes in the surface topography are registered by a change in the vertical position of the laser on the PSD; this change (measured as a change in vertical PSD voltage) serves as error signal for the piezoelectric feedback control system. The piezo moves vertically in proportion to this error signal in order to restore the tip normal force to its set-point; this vertical displacement of the piezo then serves as a measure of the height of the surface feature.

In addition to its use as a profilometer, the AFM is also used as a nanoscale tribometer to make fundamental measurements of friction at the probe-surface interface. These measurements of friction simulate a single-asperity contact, allowing the measurement of surface forces in the absence of gross wear. The reciprocating contact of an AFM probe and a surface results in torsional deflections of the cantilever free-end (figure 8), which cause a proportional *horizontal* deflection of the laser spot on the PSD. An increase in interfacial friction causes a greater torsional moment on

the cantilever, resulting in larger horizontal deflections of the laser spot on the PSD. The reciprocating motion of an AFM probe on a surface also results in the formation of friction loops, which can be used for determining the friction coefficient [71].

In addition to nanoscale friction measurement, the AFM is also frequently used for determining nanoscale mechanical properties such as hardness, modulus and adhesion [66, 72-76]. The measurement of these properties follows from the general technique of nanoindentation, where an AFM probe is indented on a surface to generate force-distance curves. By modulating indentation depth, area and force, these techniques allow the accurate quantification of mechanical properties with high surface specificity [77].

Multiasperity contact

Macroscale, multiasperity tribological characterization traces its roots to daVinci's seminal experiments investigating the effects of load and contact area on friction. A tribometer is any instrument which enables relative motion between two surfaces of interest and allows a measurement of contact forces. A tribological contact is typically characterized by its friction coefficient (μ) and/or wear rate (k). Friction coefficient of a contact is defined as the ratio of frictional force to the applied normal force, while wear rate of a material is defined as the volume of material lost, normalized to the product of the applied normal load and total sliding distance required to generate the lost volume. Mathematically,

$$\mu\,[-] = {F_f}\big/{F_n} \tag{4}$$

$$k\,[mm^3/Nm] = {\Delta V}\big/{F_n \cdot S} \tag{5}$$

Where F_f and F_n are friction and normal force, respectively, ΔV is volume loss and S is the corresponding sliding distance. Typically, tribological contacts are classified as either unidirectional or bidirectional/reciprocating depending on the direction of relation motion. In reciprocating contacts, the interfacial friction force vector alternates its direction at a half-cycle frequency.

A cycle-wise plot of instantaneous friction as a function of position along the sliding wear track results in the formation of a 'friction loop', depicted in figure 9. From the friction loop, friction coefficient (or force) is defined as the mean of the absolute values of forward and reverse friction coefficient (or force). This is often referred to as the *method of reversals* and has been shown to eliminate uncertainty in measured friction due to angular misalignments between the load cell and the substrate [78]. In the calculation of friction or friction coefficient values using the method of reversals, measurements from only the central part of the wear track are considered to avoid bias from measurements during the stick events at reversals and resulting transients.

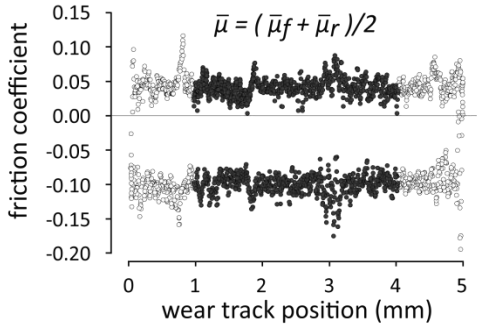

Figure 9 An illustration of a friction loop obtained in a reciprocating contact. Friction coefficient is calculated as the average of the forward and reverse values of friction coefficient, as shown.

For the calculation of wear rate, different strategies are employed depending on the configuration of the sliding contact [79, 80]. For ball-on-flat reciprocating contacts, optical profilometry measurements give a direct measure of worn volume for both the ball as well as the counterface. For these, wear volume of the counterface is sampled only from within a measurable window; this volume is assumed to be representative of the remainder of the track. In the case of pin-on-flat tests typical of polymer nanocomposites, mass or volume loss measurements of the polymer pin are used to determine worn volume. Mass loss measurements of the pin give a direct measure of the actual, total volume lost without any assumptions. In an alternative technique, the vertical position of the pin may be tracked with an LVDT to yield a measure of the uniform mass/volume lost at its surface. Wear *rate* is defined as the wear volume normalized with the product of normal force and corresponding sliding distance. A common graphical method of determining wear rate plots the wear volume against the product of normal force and sliding distance. The slope of this plot when populated, gives the instantaneous wear rate at any given number of sliding cycles.

Multi-Scale Tribometry of Molybdenum Disulfide

In the context of MoS_2 tribology, multi-scale tribometry offers a unique opportunity to investigate not only the individual contributions of water, oxygen and temperature to MoS_2 lubricity, but also to establish the role of nanoscale tribofilms in driving these macroscale phenomena. Through multi-scale tribometry with MoS_2, this dissertation tests for: (1) the role of water on MoS_2 oxidation, (2) the role of water on MoS_2 friction, (3) the role of oxygen on MoS_2 friction, (4) the contribution of thermal activation to ambient-temperature friction, and (5) effects of length-scale.

Chapter 4

EXPERIMENTAL MATERIALS AND METHODS

Materials

Pure molybdenum disulfide (MoS_2) coatings in this study were commercially sputter-deposited by Tribologix Inc. (Golden, CO). The pure MoS_2 coatings were deposited on a 440C stainless steel coupon measuring 25 mm by 38 mm, which was polished to an average surface roughness R_a ~ 30±5 nm prior to deposition. The MoS_2 coating was deposited to a nominal thickness of 1 μm (figure 10). Commercial 440C steel ball bearings with an average surface roughness R_a ~ 110 nm were used as the counterbody for all tests.

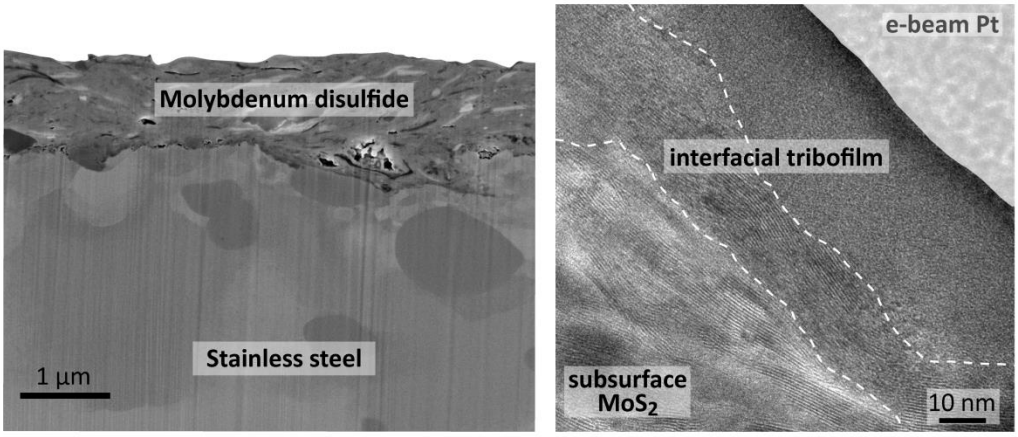

Figure 10 Cross-sectional micrograph of sputtered MoS_2 showing (a) the interface between the coating and the steel subsurface and (b) the interfacial tribofilm with a distinct lamellar microstructure.

Friction measurements in this work were made on interfaces consisting of either conditioned or unconditioned sputtered coatings. Unconditioned coatings had been previously exposed to thermal cycling between 25°C and 250°C, but no sliding either on MoS_2 or the steel ball. A 'conditioned coating' consisted of an interface which had experienced sliding contact during thermal cycling from 25°C to 250°C, thus resulting in the formation of a thermally seasoned wear track as well as transfer films prior to testing. Conditioned and unconditioned coatings are illustrated in figure 11.

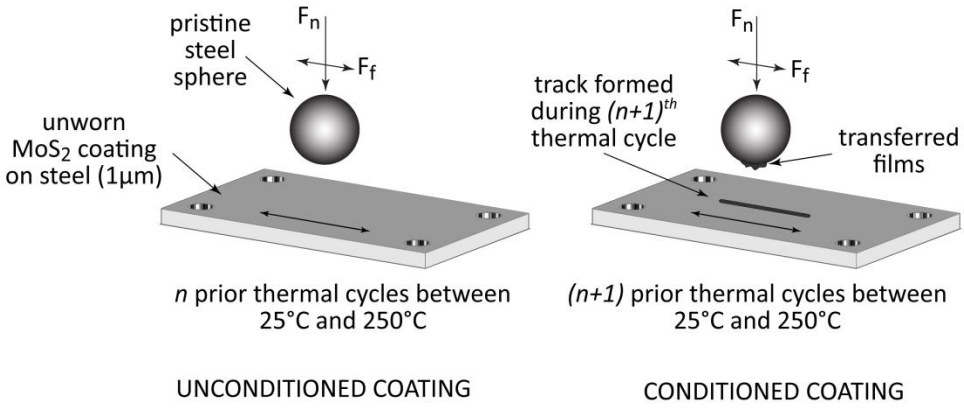

Figure 11 Schematic illustration of conditioned and unconditioned MoS_2 coating. A 'conditioned coating' is subject to sliding as well as an additional thermal cycle compared to the 'unconditioned coating'.

Macroscale Tribometry

Macroscale friction measurements were made on the High Temperature Tribometer (HTT). For all sliding tests performed on the HTT, a nominal normal force of 1N was maintained at the contact which is equivalent to a mean contact pressure of 100MPa, derived from the measurement of wear track width. The stepper motor was driven to generate a saw-tooth patterned motion with a wear track length of 5mm, and sliding velocity of 5mm/s. Stepper motion control was enabled with a custom LabView™ routine, which also allowed on-the-fly changes in the motion parameters, if required. Instantaneous values of contact forces and pin position were recorded with a second custom LabView™ routine, which was also used for generating cycle-wise friction loops and determining values of friction coefficient.

Each friction coefficient measurement, unless specified, consisted of 50 sliding cycles. Transient behavior during the 50 sliding cycles was identified using a definition from the literature, where deviations higher than 20% of the nominal value are considered transient. Steady state values of friction coefficient reported in this study were calculated from the final 30 of these 50 cycles, which were observed to consistently conform to this definition of steady-state behavior. Single cycle friction coefficients were determined using the method of reversals, described earlier, by considering only the central 60% of the friction loop. Temperature-dependent friction measurements were made by heating the substrate from 25°C to 250°C at an approximate rate of 25°C/minute.

High temperature tribometry

Macroscale friction measurements were carried out on a custom-built high temperature tribometer (HTT), shown schematically in figure 12. The tribometer

employs a reciprocating ball-on-flat contact configuration, with a ¼" 440C stainless steel ball sliding on an MoS_2 coated coupon. The tribometer consists of three key sub-assemblies, namely the force transduction stage, the thermal management stage and the reciprocating stage.

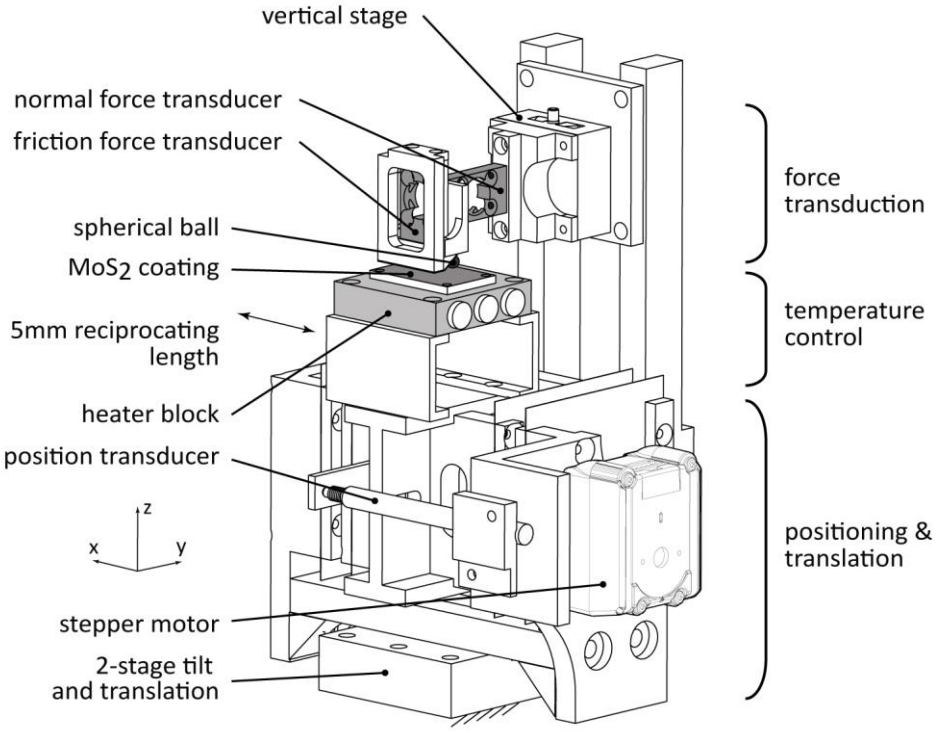

Figure 12 Schematic illustration of the custom-built High Temperature Tribometer (HTT) used for macroscale friction measurements.

Normal and tangential forces at the contact are measured by two strain-gage based load cells (Strain Measurement Devices Inc.) connected in series. The load cells are calibrated using mass standards, which have an uncertainty of 50μg. The overall uncertainty of the load cell transducers is 0.1mN. The load cell sub-assembly is fixed

to a manual vertical stage, which is used for loading and unloading the contact. Forces at the contact are transmitted to the load cells through a thin aluminum cantilever and PEEK spacers, which are incorporated to reduce thermal conduction pathways to transduction elements. As a result, the temperature of the load cell sub-assembly remained at 27±3°C throughout testing. Strain measured at the load cells is transmitted through a signal conditioning unit (National Instruments SCC-SG24), which is mounted integral to the data acquisition board (National Instruments SCC-68).

The thermal stage consists of a copper heater block, built to accommodate cartridge heaters. The MoS_2-coated coupon is mounted on top of the copper block and a K-type bolt-on thermocouple is attached to the surface to measure the surface temperature. The cartridge heaters are connected via a solid state relay to a PID-feedback temperature controller that allows accurate temperature control of the MoS_2 coating surface. The heater block itself is mounted on two steel C-sections, which connect to the reciprocating drive and help minimize thermal conduction into the stepper motor. The reciprocating stage consists of a leaf-flexure design, driven by a stepper motor through a leadscrew. A Linear Variable Differential Transformer (LVDT) attached to the stage is used for accurate position sensing.

In-situ wear measurement

MoS_2 and MoS_2-doped coatings are known to yield ultra-low wear in clean environments, similar to its lubrication response in such environments [59]. Accurate measurement of ultra-low wear with low uncertainty is inherently challenging due to the propagation of instrumental and measurement errors [80]. Accurate measurement of ultra-low wear with low uncertainty in MoS_2 does however provide the opportunity

for insights into lubrication mechanisms, which may rely on sacrificial wear of the MoS_2 surface layers.

Accurate measurements of MoS_2 coating wear were performed with the combination of a custom-built *in-situ* tribometer, shown in figure 13, and a scanning white light interferometer (SWLI). Similar to the HTT, the *in-situ* tribometer also employs a ball-on-flat reciprocating contact configuration which is driven by a stepper motor drive.

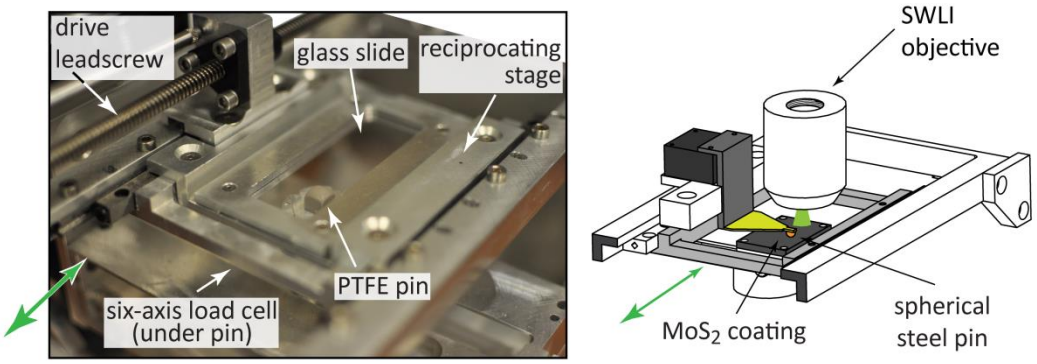

Figure 13 The *in-situ* tribometer in a (a) generic stationary-contact configuration and (b) *in-situ* coating wear measurement configuration.

The MoS_2 coating is fixed to a sample holder mounted on a 6-axis miniature load cell (ATI Industrial Automation), which is connected to the rigid base via a double leaf flexure support. A spherical steel ball serves as the countersurface and is attached to an aluminum cantilever, identical to the HTT, and fixed rigidly to the translating stage. In the *in-situ* tribometer, the SWLI objective, MoS_2 coating and load cell are held stationary and the steel ball reciprocates at a specified velocity. A Veeco

Wyko NT9100 SWLI is used for measuring the wear rate of MoS_2 coatings. Prior to measurement, the *in-situ* tribometer is mounted directly under the objective of the SWLI. The tribometer base and sample stage is adjusted such that the projected wear track lies directly under the SWLI beam.

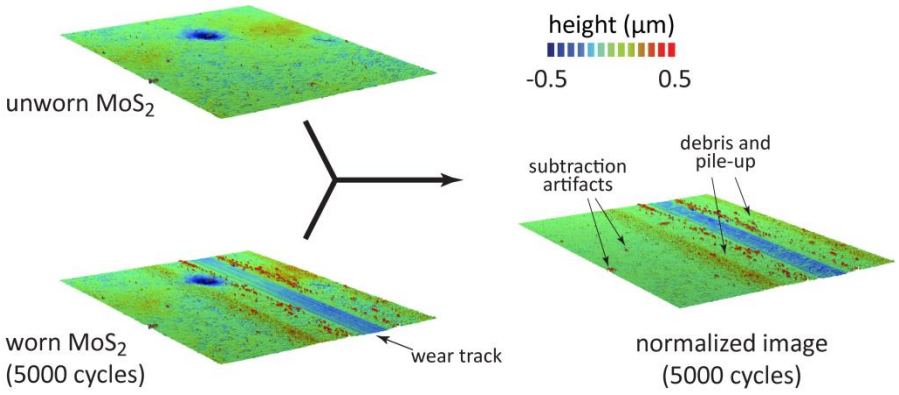

Figure 14 Illustration of *in-situ* wear measurement using reference subtraction. The topographical image of the wear track is normalized to a pre-sliding image in order to determine the actual wear volume.

Wear rate is determined by using a method of 'reference subtraction', illustrated in figure 14. In this method, the topographic image at a given number of sliding cycles is compared to an image collected at the same location prior to sliding. Translational and rotational transformations are applied to the two images based on two or more fiducial markers to align the images and ensure they directly overlay each other, within limits of uncertainty. Wear volume is next determined by calculating the simple pixel-wise difference of the z-values of the two images. As illustrated in figure 14 however, small offsets in the alignment step can contribute to subtraction artifacts which are proportional to the surface roughness.

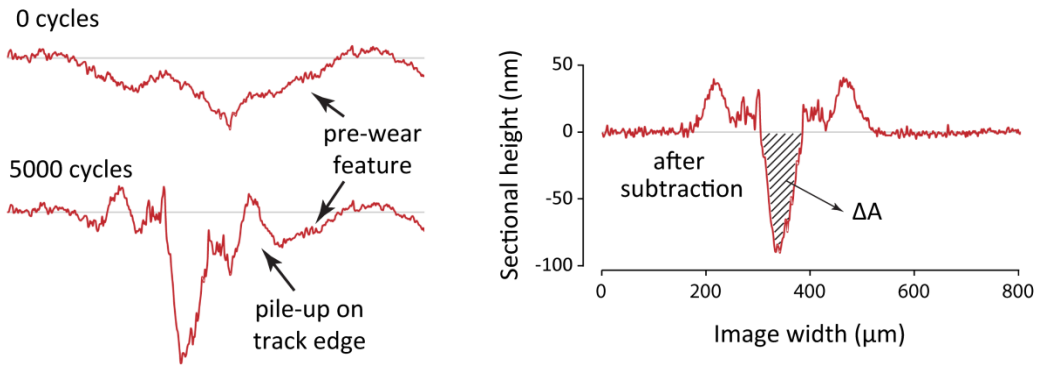

Figure 15 Illustration of the row-wise reference subtraction technique used for wear quantification. The representative cross-sections of the worn and unworn image (left) are normalized, yielding the actual wear cross section (right). The equivalent wear is given by the area enclosed by the track below the reference line.

The sensitivity of the wear measurement can be increased by reducing the 'false wear volume' contributions from poorly-matched asperities outside the wear track. The latter can be minimized by considering a *representative* wear profile at a given number of cycles which is evaluated by row-wise averaging of z-values, in a direction parallel to the wear track, as shown in figure 15. The representative wear profile is normalized to the unworn profile, similar to the pixel-wise normalization discussed earlier. The normalized wear profile shows distinct regions of positive wear volume, marked by the wear track and 'negative wear volume' consisting of the material pile-up near the track edge. In this study, wear is explicitly defined as the removal of material strictly under the reference line (figure 15), which also avoids confounding effects of loose debris and plastically deformed regions (small in this study) of pile-up. In order to determine the net wear volume, the area under the y=0 line is evaluated and multiplied by the image depth.

Nanoscale Tribometry

A key hypothesis in the lubrication of MoS_2 is that basally oriented nanoscale tribofilms drive its macroscale friction response [18]. Similar to the accurate measurement of ultra-low wear rates, accurate and quantitative measurement of nanoscale friction of sliding-induced tribofilms is critical to an improved understanding of their contributions to macroscale lubrication. Although AFM-based techniques in nanoscale friction measurements are uniquely suited to making such a probe, the absence of nanoscale force calibration standards make quantitative lateral force microscopy prohibitively challenging. In this section, existing calibration techniques and limitations are reviewed to create a foundation for method developed for this work.

Lateral force calibration: Background and challenges

As noted earlier, changes in the normal force or interfacial friction force in an AFM result in changes in the laser spot position on the PSD in the vertical and horizontal directions, respectively. The position of the laser spot and any changes due to interfacial forces are however registered as a voltage signal on the PSD. Calibration of the raw PSD voltage signal to units of force is a prerequisite to any meaningful quantification of nanoscale forces [74, 81, 82]. For the purpose of quantitative nanotribology, such calibration needs to be performed for both the normal as well as the torsional/lateral directions.

The development of calibration methods for normal force measurement has generally preceded development of lateral force calibration methods. The conversion of a raw voltage signal generated by pure bending of the cantilever to units of force essentially consists of two components – the relationship between force and tip-

deflection (i.e. bending stiffness) of the cantilever and the relationship between PSD laser position and PSD voltage output (i.e. PSD voltage sensitivity). The bending stiffness of a cantilever can be determined by using the geometry and material properties of the cantilever and expressions derived from the Euler-Bernoulli beam theory. In practice however, uncertainty in the measured dimensions (especially thickness) of the cantilever together with non-ideal material properties result in theoretical bending stiffness differing substantially from the actual value [74]. Several other methods have been proposed to circumvent these problems, such as the reference cantilever method; these methods however, either require specialty calibration components or involve complicated test setups [74]. A relatively straightforward method of calibrating AFM normal deflection proposed by Sader *et al.* [83] utilizes the cantilever plan-view dimensions together with resonant frequency and Q-factor – quantities which are easily determinable using a frequency drive feature available to most AFM systems. According to the Sader method, the stiffness k of a rectangular cantilever with an effective mass M_e, dimensions L, b and h, and density ρ_c is given as

$$k = M_e \rho_e b h L \omega_{vac}^2 \tag{6}$$

where ω is the fundamental resonant frequency of the system in vacuum [83].

In order to determine the voltage sensitivity of the PSD in the vertical direction, a force-displacement curve is generated on a nominally rigid substrate which resists elastic and inelastic deformation. With 'indentation' on a rigid substrate, changes in the position of the piezo (i.e. the horizontal axis on the force-distance plot) in the contact region reflect only the deflection of the cantilever. The slope of the force-distance plot in the contact region of such an indentation therefore yields a direct measurement of the sensitivity of the PSD to a given deflection of the cantilever. The

product of the PSD sensitivity and the cantilever stiffness then yields the required calibration for converting changes in the PSD voltage to the contact normal force in Newton.

The extension of these calibration strategies to lateral force measurement is beset by the difficulty in imposing a knowable pure torque at the tip (to induce a purely lateral motion of the laser on the PSD) as well as in accurately determining the torsional resonant frequency of the cantilever. As a result, calibration of AFM probes for lateral force measurement has remained a challenge in quantitative nanotribology. Several methods for quantifying measured lateral forces in an AFM have been developed, which adopt a variety of techniques for determining lateral calibration sensitivities.

The 'wedge method' for lateral force calibration, proposed by Ogletree *et al.* was perhaps the first methods for calibrating the AFM for quantitative nanotribology [84]. In the wedge method, calibration of an AFM cantilever probe is performed by the reciprocating motion of an AFM probe on the two sloped surfaces of a calibration substrate of annealed $SrTiO_3$. As shown in figure 16(a), the friction loops generated as a result are offset from the zero position by a value which is proportional to the wedge angle and direction; the value of the friction loop width (or half-width) is proportional to the friction at the interface, as before.

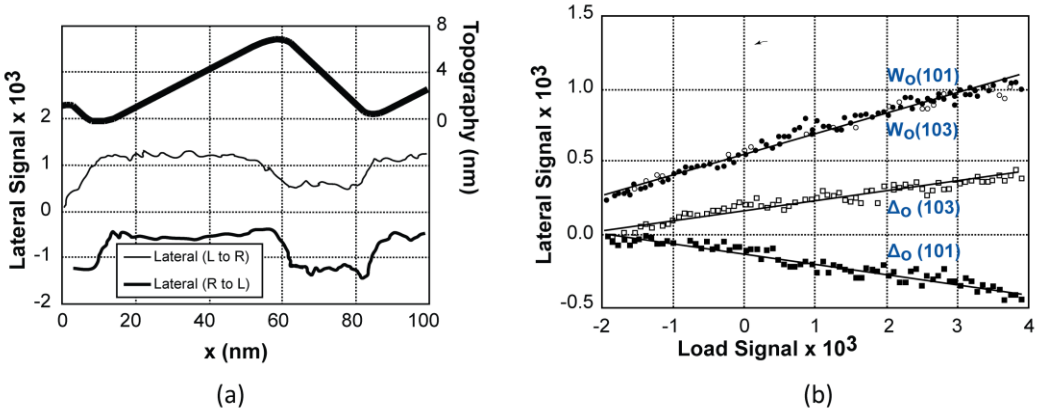

Figure 16 Illustration of the Ogletree method for LFM calibration (adapted from Ogletree *et al.* [84]). (a) Lateral scanning on the calibration ridges yields a corresponding friction loop, and (b) the values of W and Δ from the friction loop, as a function of impressed normal load are used as inputs to the method.

Calibration by the wedge method involves the generation of such friction loops for a range of applied normal loads, as shown in figure 16(b), in order to determine the rate of change of the friction loop offset and half-width with respect to normal load. A force balance during forward and reverse sliding at the tip-surface interface reveals two equations which are then solved for the unknown friction coefficients and the calibration ratio. Since the value of the calibration ratio is determined directly from the scanning motion of an AFM tip, the wedge method eliminates the need for separate calibration for spring torsional stiffness and the PSD voltage sensitivity.

The nature of the $SrTiO_3$ calibration grating precludes the calibration of AFM probes larger than the size of its facets. Varenberg *et al.* [85] proposed a method of calibration known as the 'improved wedge method' where the nanoscale facets of the $SrTiO_3$ substrate were replaced with a silicon calibration grating which allowed the calibration of probes with larger diameters. The formulation of the improved wedge

method also followed from the solution of the force balance at the tip-substrate contact. Li *et al.* [86] noted that the validity of these equations used in the wedge methods breaks down if the apex of the probe is offset from the shear center axis of the cantilever. Tip offset can be especially pronounced in colloid probes where the probes are mounted manually to the cantilevers, although variations in cantilever material properties and manufacturing imperfections often cause significant offset even in integrated tips. Li *et al.* propose a diamagnetic levitation based calibration technique for the direct calibration of lateral and normal forces. Other methods have been proposed which eliminate the need for tip contact during calibration which is useful for functionalized probes which are susceptible to damage during calibration. Cannara *et al.* [87] proposed a calibration technique where the probe is moved horizontally against a GaAs rigid support to induce a torsional deflection thereby reducing the probability for tip damage. However, with all classical calibration methods, pre-measurement adjustments of the laser position and PSD mirror tilt directly alter the calibration by changing the optical lever arm, thus introducing measurement uncertainties.

Lateral force calibration: Method development

Existing calibration methods preclude accurate measurement of nanoscale friction due to both the inherent complexity of force transduction as well as propagated uncertainties in an AFM. In order to facilitate accurate measurement of quantitative friction at the nanoscale, an *in-situ* method of lateral force calibration is required which reduces measurement uncertainties due to prior adjustment of the AFM components and to account for manufacturing artifacts such as shear-center offset. Such a method should (1) allow simultaneous measurement and calibration to

eliminate the possibility of changes to the optical lever arm or damage to tip functionality, (2) eliminate measurement uncertainties due to shear-center misalignment, piezo-tube misalignment and PSD crosstalk, (3) enable friction calibration for all forms of reciprocating contacts, irrespective of probe geometry without reliance on calibration substrates.

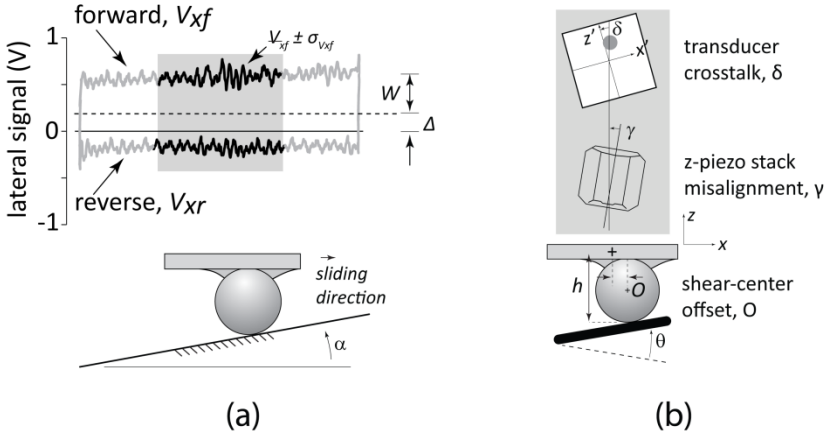

Figure 17 An illustration of the general contact of an AFM probe, showing (a) the resulting friction loop from sliding on a nominally tilted substrate, which results in non-zero W and Δ, and (b) typical instrument misalignments which affect measured friction.

A representative friction loop obtained during the reciprocating motion of the AFM probe is shown in figure 17(a). The friction loop obtained in the AFM is identical to macroscale tribometer friction loops (discussed earlier) with the exception that the normal and lateral deflections are measured in volts rather than Newton. Similar to earlier friction loops, the average and standard deviation within the central portion of the friction loop is evaluated to eliminate the effect of direction reversals at the two ends of the wear track. As before, the friction coefficient may be determined

from the friction loop as: $\mu = 0.5 \cdot (\bar{V}_{xf} - \bar{V}_{xr})/\bar{V}_z$. Using the law of propagation of uncertainty and the standard deviation in friction coefficient measurement, an estimate of measurement uncertainty may also be determined [88].

As illustrated in figure 17(a), we define the friction loop width (W) and friction loop offset (Δ) as: $W = (\bar{V}_{xf} - \bar{V}_{xr})/2$ and $\Delta = (\bar{V}_{xf} + \bar{V}_{xr})/2$. These definitions of loop width and offset have been adopted from the original wedge method [84]. Qualitatively, the friction loop width is a measure of the interfacial friction while the friction loop offset derives from a combination of shear-center offset and angular misalignment between the cantilever and substrate. The wedge methods by Ogletree *et al.* and Varenberg *et al.* rely on calibration substrate with known wedge angles [84, 85]. In the current 'Extended Wedge Method', the closed-loop motion of the piezo, which adjusts z-height to maintain a constant normal force (measured as V_z) is used to directly measure the substrate tilt angle (θ) relative to the piezo x-axis.

The extended wedge method incorporates instrument misalignments in order to reduce or eliminate measurement uncertainty in friction. One of the sources of error in measured friction is an angular misalignment (γ) between the cantilever horizontal axis and the piezo horizontal axis, illustrated in figure 17(b). Additionally, angular misalignment δ of the PSD relative to measurement axes, shown in figure 17(b), contributes to transducer crosstalk and has been identified as an important source of measurement error [81]. In the wedge method, Ogletree *et al*. note that although the determination of friction coefficient and calibration ratio can be made using a single wedge angle, a two-slope technique becomes necessary to eliminate errors due to crosstalk. Although the AFM is susceptible to measurement errors from a variety of sources, the experimental nanotribology literature suggests that the most significant

measurement errors are driven by transducer-piezo misalignment, tip-cantilever shear-center offset, and non-zero probe radii [81, 86, 89-91]. As a result, piezo misalignment (γ), shear-center offset ratio (O/h) and probe radius (R/h) are explicitly included in the formulation of the extended wedge method.

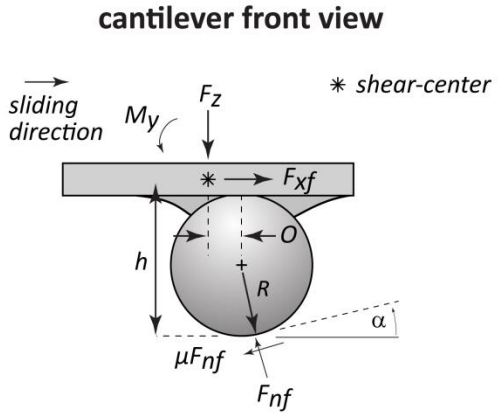

Figure 18 Free-body diagram of the AFM probe in sliding contact with a tilted substrate, showing interfacial forces as well as the forces and moments applied at the cantilever shear center. The length of the cantilever extends into the plane of paper.

A free-body diagram of the AFM probe in sliding contact with a generalized substrate is shown in figure 18. For derivational purposes here, the motion of the probe from left to right is referred to as 'forward sliding' (subscript *f*) while the motion right to left is referred to as 'reverse sliding' (subscript *r*). The direction of contact forces changes between the two sliding directions; their combination yields a friction loop and is used for deriving the expressions for friction coefficient and calibration ratio.

The wedge angle α shown in figure 18 represents the effect of misalignment between the wedged surface and the horizontal axis of the transducer (PSD), and consists of the physical tilt of the surface θ and the angular misalignment γ of the piezo relative to the cantilever horizontal axis. Mathematically then, $\alpha = (\theta - \gamma)$. In this schematic, the length of the cantilever extends into the plane of paper. Due to a lateral sliding motion, the tip experiences contact forces F_{nf} and μF_{nf}, while the cantilever shear center also experiences a torsional moment M_y. The schematic shown here applies to any probe geometry; in integrated pyramidal probes, the probe radius R approaches 0 (typically < 10nm). A force balance in the vertical direction gives

$$F_z = F_{nf} \cdot \cos(\alpha) - \mu \cdot F_{nf} \cdot \sin(\alpha)$$

$$F_{nf} = \frac{F_z}{(\cos(\alpha) - \mu \cdot \sin(\alpha))}$$

A force balance in the horizontal direction, together with the expression for F_{nf} gives,

$$F_{xf} = \mu \cdot F_{nf} \cdot \cos(\alpha) + F_{nf} \cdot \sin(\alpha)$$

$$= F_z \cdot \left(\frac{\mu \cdot \cos(\alpha) + \sin(\alpha)}{\cos(\alpha) - \mu \cdot \sin(\alpha)}\right) = F_z \cdot A$$

Where A is defined for conciseness as $(\mu \cdot \cos(\alpha) + \sin(\alpha))/(\cos(\alpha) - \mu \cdot \sin(\alpha))$.

A moment balance about the point of contact yields,

$$M_{yf} = F_{xf} \cdot \big(h - R \cdot (1 - \cos(\alpha))\big) - F_z \cdot (O + R \cdot \sin(\alpha))$$

$$\Rightarrow M_{yf} = F_z \cdot \big(A \cdot h - O - A \cdot R \cdot (1 - \cos(\alpha))\big) - R \cdot \sin(\alpha)) \qquad (7)$$

Where O is the tip-offset, R is the probe radius and h is the probe height, as illustrated in figure 18. Similarly, writing the force and moment balance equations for reverse sliding yields:

$$F_{xr} = -\mu \cdot F_{nr} \cdot \cos(\alpha) + F_{nr} \cdot \sin(\alpha)$$

$$= F_z \cdot \left(\frac{-\mu \cdot \cos(\alpha) + \sin(\alpha)}{\cos(\alpha) + \mu \cdot \sin(\alpha)}\right) = F_z \cdot B$$

$$M_{yr} = F_{xr} \cdot \big(h - R \cdot (1 - \cos(\alpha))\big) - F_z \cdot (O + R \cdot \sin(\alpha))$$

$$\Rightarrow M_{yr} = F_z \cdot \big(B \cdot h - O - B \cdot \mathrm{R} \cdot (1 - \cos(\alpha))\big) - R \cdot \sin(\alpha)) \quad (8)$$

Where B is defined for conciseness as $(-\mu\cdot\cos(\alpha)+\sin(\alpha))/(\cos(\alpha)+\mu\cdot\sin(\alpha))$. Next, we define calibration constants C_z and C_x for the normal and lateral PSD deflections, respectively, as $C_z = F_z/V_z$ and $C_x = F_x/V_x$, where F_z and F_x are the corresponding vertical and lateral forces at the contact. Similarly, the moment about the shear center M_y can be rewritten in terms of the calibration constant C_x as $M_y = F_x \cdot h$, or alternatively as $M_y = C_x \cdot V_x \cdot h$. Substituting these for F_z, M_{yf} and M_{yr} in (7), we obtain

$$C_x \cdot V_{xf} \cdot h = C_z \cdot V_z\big(A \cdot h - O - A \cdot \mathrm{R} \cdot (1 - \cos(\alpha))\big) - R \cdot \sin(\alpha))$$

$$V_{xf} = \left(\frac{V_z}{S}\right)\left(A - \frac{O}{h} - A \cdot \frac{R}{h} \cdot (1 - \cos(\alpha)) - \frac{R}{h} \cdot \sin(\alpha)\right) \quad (9)$$

Where $S = C_x/C_z$ is the ratio of lateral and normal calibration constants. Similarly, for the reverse sliding we obtain

$$C_x \cdot V_{xr} \cdot h = C_z \cdot V_z\big(B \cdot h - O - B \cdot \mathrm{R} \cdot (1 - \cos(\alpha))\big) - R \cdot \sin(\alpha))$$

$$V_{xr} = \left(\frac{V_z}{S}\right)\left(B - \frac{O}{h} - B \cdot \frac{R}{h} \cdot (1 - \cos(\alpha)) - \frac{R}{h} \cdot \sin(\alpha)\right) \quad (10)$$

Recalling that friction loop and offset are defined as $W = (\bar{V}_{xf} - \bar{V}_{xr})/2$ and $\Delta = (\bar{V}_{xf} + \bar{V}_{xr})/2$, the values of W and Δ can be determined using the expressions for V_{xf} and V_{xr} in (9) and (10). In the original wedge method, the quantities W' and Δ' are

defined as the rate of change of friction loop width and offset with respect to the normal force voltage, such that $W' = dW(V_{xf}, V_{xr})/dV_z$ and $\Delta' = d\Delta(V_{xf}, V_{xr})/dV_z$. Retaining these definitions of *W'* and *Δ'*, from (9) and (10), we obtain

$$W' = \left(\frac{1}{2 \cdot S}\right)\left(A - B - \frac{R}{h} \cdot (1 - \cos(\alpha)) \cdot (A - B)\right)$$

$$W' = \left(\frac{1}{S}\right) \cdot \left(\frac{\mu}{cos^2\alpha - \mu^2 \cdot sin^2\alpha}\right)\left(1 - \frac{R}{h} \cdot (1 - \cos(\alpha))\right) \quad (11)$$

$$\Delta' = \left(\frac{1}{2 \cdot S}\right)\left((A + B) - \frac{R}{h} \cdot (1 - \cos(\alpha)) \cdot (A + B) - 2\frac{O}{h} - 2\frac{O}{h} \cdot \sin(\alpha)\right)$$

$$\Delta' = \left(\frac{1}{S}\right)\left(\left(\frac{(1+\mu^2) \cdot \sin(\alpha) \cdot \cos(\alpha)}{cos^2\alpha - \mu^2 \cdot sin^2\alpha}\right)\left(1 - \frac{R}{h} \cdot (1 - \cos(\alpha))\right) - \frac{O}{h} - \frac{R}{h} \cdot \sin(\alpha)\right) \quad (12)$$

The effects of transducer crosstalk due to PSD misalignment in the original wedge method were circumvented by adopting a two-slope calibration approach. Ogletree *et al.* measured the values of both the quantities W' and Δ' on the two facets of their $SrTiO_3$ calibration grating. A similar approach is adopted in the extended wedge method, whereby the quantities in (11) and (12) are evaluated on two opposing wedge angles of the substrate. Recognizing *S* that the calibration ratio remains unchanged if the AFM optics are not perturbed, rearranging (11) and (12) to reveal an expression for *S*, and writing the resulting equations for both wedge angles, we obtain:

$$S = \frac{1}{W_1'} \cdot \left(\frac{\mu_1}{cos^2(\alpha_1) - \mu_1^2 \cdot sin^2(\alpha_1)}\right)\left(1 - \frac{R}{h} \cdot (1 - \cos(\alpha_1))\right) \quad (13)$$

$$S = \frac{1}{\Delta_1'}\left(\left(\frac{(1+\mu_1^2)\cdot\sin(\alpha_1)\cdot\cos(\alpha_1)}{cos^2(\alpha_1) - \mu_1^2 \cdot sin^2(\alpha_1)}\right)\left(1 - \frac{R}{h}(1 - \cos(\alpha_1))\right) - \frac{O}{h} - \frac{R}{h} \cdot \sin(\alpha_1)\right) \quad (14)$$

$$S = \frac{1}{W_1'} \cdot \left(\frac{\mu_2}{cos^2(\alpha_2) - \mu_2^2 \cdot sin^2(\alpha_2)}\right)\left(1 - \frac{R}{h} \cdot (1 - \cos(\alpha_2))\right) \quad (15)$$

$$S = \frac{1}{\Delta_1'}\left(\left(\frac{(1+\mu_2^2)\cdot\sin(\alpha_2)\cdot\cos(\alpha_2)}{cos^2(\alpha_2) - \mu_2^2 \cdot sin^2(\alpha_2)}\right)\left(1 - \frac{R}{h}(1 - \cos(\alpha_2))\right) - \frac{O}{h} - \frac{R}{h} \cdot \sin(\alpha_2)\right) \quad (16)$$

Where subscripts 1 and 2 denote first and second wedge configuration with $\alpha_1 = (\theta_1 - \gamma)$ and $\alpha_2 = (\theta_2 - \gamma)$. With these four equations in S, the quantities W_1', W_2', Δ_1', Δ_2', θ_1 and θ_2 are determined directly from the experimental measurements with the AFM. In the system of four equations however, the number of unknowns (μ_1, μ_2, γ, O/h, R/h and S) needs to be reduced from six to four in order to obtain a unique solution. The radius of the probe R and tip length h are typically either known in advance, or determined with SEM imaging. As a result, R/h is considered a known quantity in the extended wedge method. Measurement errors due to uncertainties in estimated values of R/h are evaluated later.

From the remaining unknowns, one more parameter needs to be eliminated in order to make the system of equations tractable. The sensitivity of the measured friction coefficient to the omission of each variable is mathematically determined to ascertain which parameters may be neglected without appreciable errors in calibration. Interfacial friction coefficients were simulated to yield corresponding simulated values for W_1', W_2', Δ_1' and Δ_2'. The actual physical conditions which were simulated were $\mu_2 = 2 \cdot \mu_1$, $\gamma = 1°$, $O/h = 1$, $R/h = 0$, and $\theta = \pm 8.5°$. These imposed friction coefficients

were then compared with the values calculated by the extended wedge method; the error in friction coefficient was separately determined for each of the following three assumptions: $\mu_1 = \mu_2$; $\gamma = 0$; and $O/h = 0$. The results for this analysis are shown in figure 19.

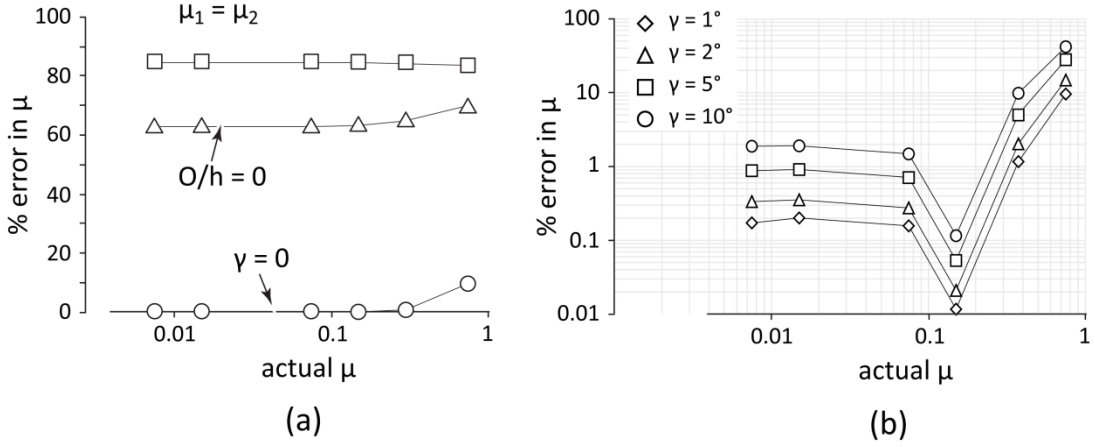

Figure 19 Results of the sensitivity analysis of the extended-wedge method showing (a) the error in evaluated friction coefficient as a result of assumed values of μ_1, μ_2, O/h or γ, and (b) the error in evaluated friction coefficient as a function of angular piezo-tilt misalignment angle (γ). The actual physical conditions which were simulated were $\mu_2 = 2 \cdot \mu_1$, $\gamma = 1°$, $O/h = 1$, $R/h = 0$, and $\theta = \pm 8.5°$. Only the omission of piezo-tilt misalignment yields negligible error in measured friction for values between 1° and 10°.

As shown in figure 19(a), the assumption of equal friction coefficients on the two wedge angle leads to large (~ 85%) errors in calculated friction coefficient. Next, the effects of neglecting tip-offset are considered. Although the errors in calculated friction coefficients are reduced, as shown in figure 19(a), they are still significant at ~60%. Finally, the effect of neglecting piezo-tilt misalignment on calculated friction

coefficient is considered for $\gamma = 1°$ in figure 19(a). The results suggest that while omitting tip-offset and frictional variability lead to high errors in measured friction coefficient, the errors associated with omitting a piezo-tilt misalignment are relatively small. Next, the value of the simulated piezo tilt was increased to 2°, 5° and 10° to determine error sensitivity. As shown in figure 19(b), error in measured friction remains low for nearly all values of friction coefficient and γ. As the actual friction coefficient value approaches unity, the error due to an unrealistically high (=10°) piezo-tilt misalignment approaches ~40%. Since this assumption yields reasonably low errors in measurement for expected ranges of friction coefficients and piezo-tilt misalignments (~1°) only the assumption that $\gamma = 0$ is adopted in the extended wedge method. No assumptions are introduced for frictional variability (i.e., $\mu_1 \neq \mu_2$) and tip-offset (i.e., $O/h \neq 0$).

The value of tip radius and the ensuing ratio R/h was considered a known quantity, since its value may be determined using optical or electron imaging methods. The error in measured friction associated with tip-radius measurement uncertainty was determined using simulated values of R/h and friction coefficient, as before. Three R/h values of 0.4, 0.04 and 0.004 were considered; these correspond to a colloidal probe ($2.R \sim h$), an intermediate tip ($2.R < h$) and a sharp, integrated tip ($2.R << h$). As shown in figure 20, frictional errors associated with integrated tips remain below 5% for a radius uncertainty as high as 1000%.

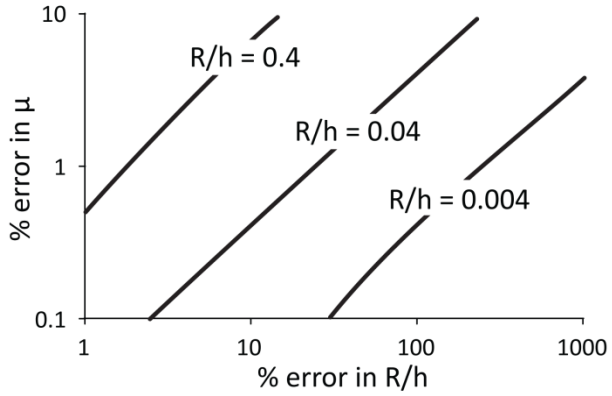

Figure 20 Simulated error in friction coefficient determined by the extended wedge method as a function of error in *R/h*. Uncertainty in *R/h* values of integrated probes (where *R/h* ~ 0.004) results in a negligible error in friction. A 10% error in measurement of colloidal probe *R/h* (where *R/h* ~ 0.4) yields frictional uncertainty of 10%.

On the other hand, a 10% error in the measurement of a colloidal probe radius results in a nearly commensurate error in friction. It is important to note that *R/h* values of 0.4 are typical of large colloidal probes, where the typical probe diameter often exceeds 1μm. Due to the large probe size, errors associated in the measurement of probe diameters are typically less than 10%. Assuming an uncertainty of 20% in cantilever thickness and propagating these errors in the measurement of *R/h*, we find that typical uncertainty in the value of *R/h* for colloidal probes is better than 5%. For the integrated probes where tip radius is much smaller relative to tip height, the error in friction measurement remains small even for large uncertainty in radius measurement.

Lateral force calibration: Experimental validation

The extended wedge method consists of solving the system of four equations 13-16 for the unknown values of μ_1, μ_2, O/h and S, given a known value of R/h and the assumption that $\gamma = 0$. Validation of the extended wedge method with an AFM is precluded by a lack of traceable force standards and the indeterminate misalignments within the instrument. Since the method is general, validation of the extended wedge method was performed on a calibrated microtribometer. Additionally, the transducer stage on the microtribometer can be misaligned ($\gamma \neq 0$) to test sensitivity to nonzero γ. A schematic of the microtribometer is shown in figure 21.

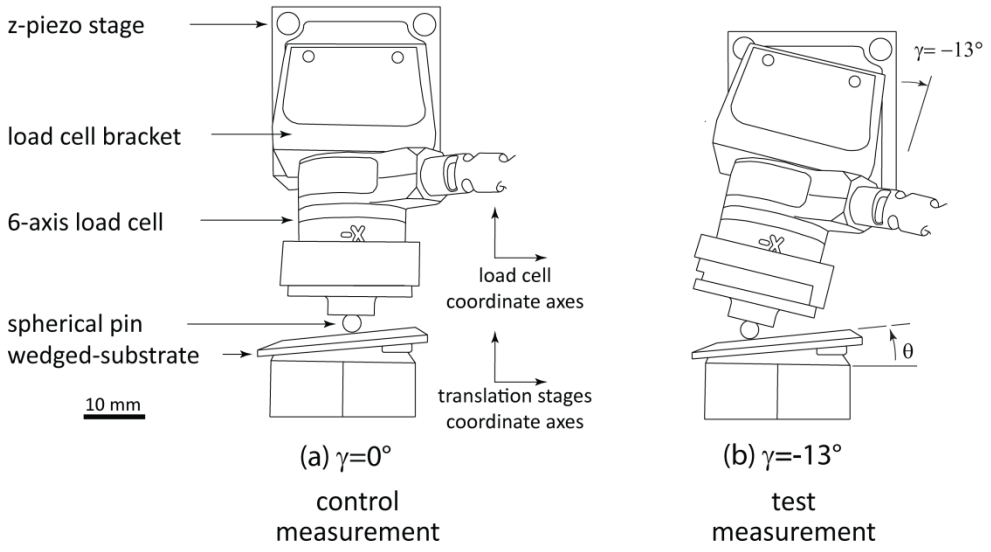

Figure 21 Schematic of the microtribometer configuration used for validation of the extended wedge method (a) control measurement, where $\gamma = 0°$ and (b) test measurement, where $\gamma = -13°$.

The microtribometer is functionally identical to the AFM. It consisted of a transducer stage and two nanopositioning stages, one each for the horizontal and

vertical directions. Contact forces were measured with a six-axis load cell (ATI Industrial Automation), which was factory-calibrated to an uncertainty of 3mN. The horizontal and vertical nanopositioning stages (PI piezoelectric stage) had a nominal uncertainty of 5nm and 1nm, respectively. Experiments were conducted with a ¼" 440C steel ball sliding against a silicon wafer, mounted to tilt stage and lubricated with lithium grease. A 200μm wear track was created with a sliding speed of 500μm/s. Normal force was increased between 0.2V and 1V, in increments of 0.2V (corresponding to 0.2-1N, in increments of 0.2N) using closed-loop feedback on the vertical piezo-stage. Similar to an AFM, the tilt angle was determined using the motion of the vertical piezo stage relative to the horizontal piezo stage.

Microtribometer validation of the extended wedge method consisted of three measurements, namely the standard, control and test measurement. For the standard measurement, the friction coefficient was measured directly from the calibrated load cell. For the control measurement, the extended wedge method was used to evaluate the friction coefficient based on recorded values of raw voltage in the normal and lateral directions. In the control measurement, the transducer stage was kept orthogonal to the translating stage, as shown in figure 21(a). The test measurement was identical to the control measurement with the exception that the transducer stage was tilted to an angle $\gamma = -13°$ to simulate a non-zero piezo-tilt in the instrument, although per the extended wedge method, γ was set as 0 in equations 13-16.

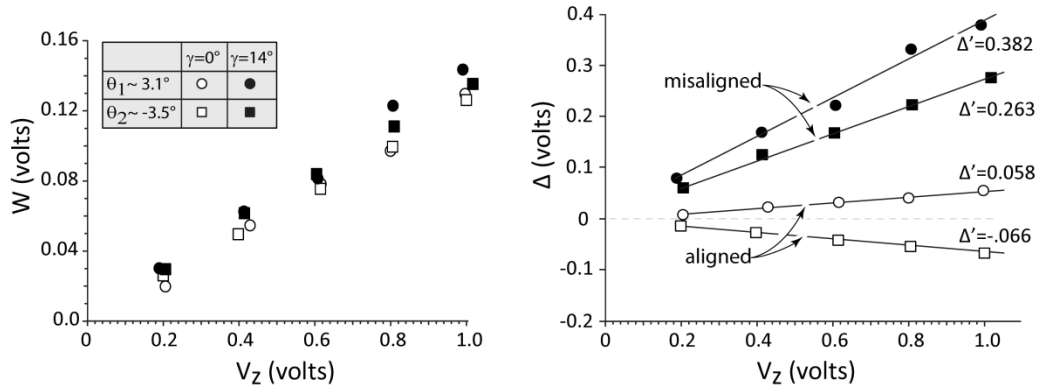

Figure 22 Results of the validation measurements performed on the microtribometer, showing (a) values of W obtained for the control and test measurements and (b) values of Δ obtained for the control and test measurements. The raw data for the control and test measurements are given in Appendix A.

The values of W_1, W_2, Δ_1 and Δ_2 obtained from the control and test measurement are plotted as a function of V_z in figure 22. The values of W_1' and W_2' are similar, suggesting that the friction coefficients in both aligned and misaligned configurations (and for both wedge angles) are similar. Using the values of W_1', W_2', Δ_1' and Δ_2' obtained from these plots, friction coefficients of 0.141 ± 0.007 and 0.125 ± 0.010 were obtained for the control and test measurement, respectively. These compare well with the standard test friction coefficient of 0.132 ± 0.008 obtained from the calibrated load cell. The friction coefficients determined by the extended wedge method were not statistically different from each other or from calibrated values. Therefore, the method is robust and insensitive to unknown values of γ in the range (-13°, 13°).

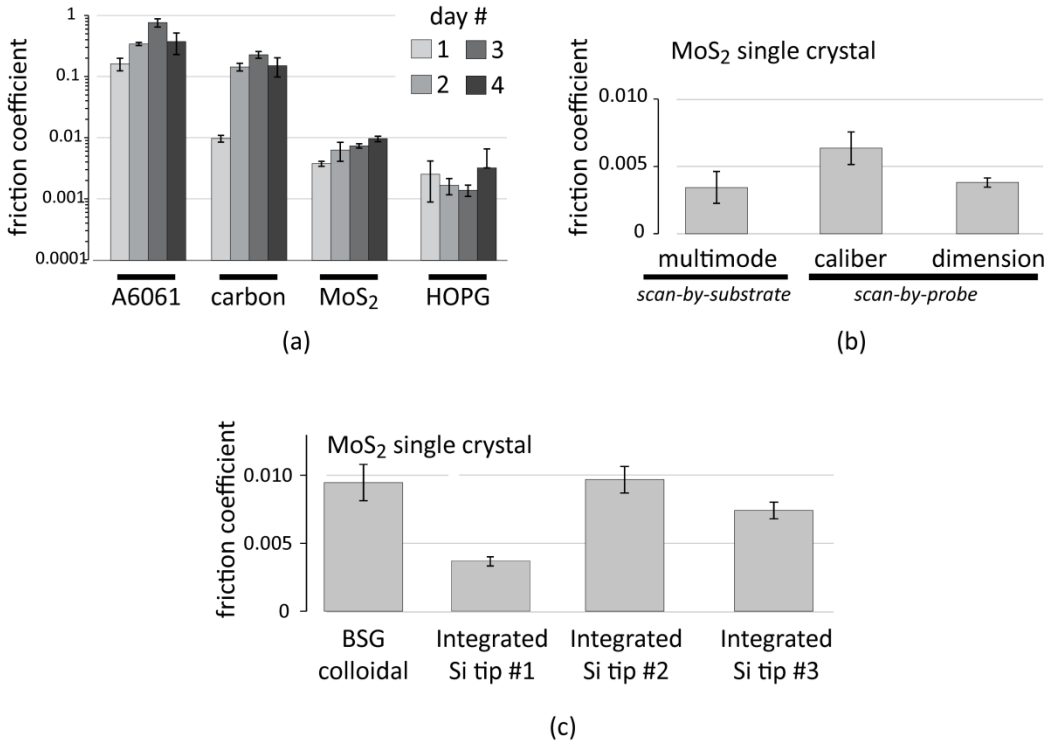

Figure 23 Results of the nanoscale friction measurements performed as part of the extended wedge method validation, showing (a) friction coefficients obtained on four substrates over a prolonged testing period, (b) friction coefficients measured on single crystal MoS_2 but with different AFM platforms, and (c) friction coefficient measured on single crystal MoS_2 but with different probes. The extended wedge method gives repeatable measurement of friction across several orders of magnitude on different substrates, and irrespective of measuring apparatus or probe size on single crystal MoS_2.

Measurements of nanoscale friction were also made using different probes, with different platforms (described later) and on different substrates to assess measurement repeatability with the extended wedge method and an AFM. Figure 23 shows friction coefficient values obtained for polished aluminum alloy (A6061), graphitic carbon, cleaved MoS_2 single crystal and cleaved highly oriented pyrolytic

graphite (HOPG). These measurements were performed over a period of several days, as indicated, and the results show statistically significant trends in friction coefficient which vary across three orders of magnitude for the four materials. Measurements using different probes and on different AFM platforms with the single crystal MoS_2 substrate also show repeatable friction coefficients, reflecting the applicability of the method to nanoscale friction measurements regardless of tip shape or instrument choice. It is worth noting that unlike the Caliber and the Dimension, which are scan-by-probe AFM, the Multimode V is a scan-by-substrate AFM where the measurement optics remain stationary while the substrate is translated via a piezoelectric stage.

LFM measurements

Nanoscale tribological measurements were made with commercial AFM platforms. Nanoscale friction measurements were performed either on a Bruker Dimension 3100 AFM or a Bruker Caliber AFM, indicated as applicable, both operating in contact mode. These two AFMs were used interchangeably as experiments showed no difference in the measured friction (tested on single crystal MoS_2) between instruments (as shown in figure 23). Friction measurements were performed with either an integrated silicon probe or a colloidal borosilicate glass (BSG) probe, both attached at the end of a silicon cantilever with a manufacturer reported nominal stiffness of 1.6 N/m (FORTA series cantilever from AppNano Inc.). The integrated silicon probe has a nominal height of 14 μm and unworn tip radius < 10nm. The silicon probes were preworn against the intended substrate to reduce wear during measurements. SEM measurements of the worn probes gave an estimated, actual tip radius of 70 ±50 nm ($R/h \sim 0.006$). Colloidal BSG probes affixed at the end of FORTA cantilevers had a nominal diameter of 12 μm ± 2 μm.

Initial measurements of friction on different substrates were aimed largely at validating the extended wedge method and ensuring repeatability, and were performed with the integrated silicon probe. Subsequent measurements probing the nanoscale tribology of MoS_2 were conducted with both the colloidal probe as well as the integrated probe.

Nanoscale friction measurements (with a given AFM) were made by repetitive, single-line scans (10μm track at ~ 1 Hz sliding frequency) under the ambient air conditions, at 25°C. The substrates were wedged on a custom rotary stage with locating positions (via spring-loaded ball in socket joints), separated by 180° to produce two different wedge angles. Multiple scans were performed at nominal force set-point voltages of 1, 3, and 5V for both wedge configurations. Values from the two wedge angles of W' and Δ' thus determined at these three set-point voltages is then used for determining the calibration ratio S and the friction coefficient μ. Repeat measurements were performed for any given substrate at different spatial locations to determine a nominal value and the associated standard deviation.

Environmental Control

Macroscale friction measurements for both ambient and elevated temperature tribometry were performed in an environmentally controlled glovebox (Vacuum Atmospheres Co.). It was of interest to study the tribological response of MoS_2 when subject to oxygen and water exposure, both individually as well as with a combination of both. To enable this, tribometry was performed in four different environments, namely dry nitrogen (lacking both O_2 and water), humid nitrogen (water-only), dry air (oxygen-only) and standard lab air (combination of both oxygen and water).

A dry nitrogen environment was introduced by initially purging the glovebox with 99.998% pure nitrogen gas until the moisture content was reduced to below 400 parts per million (ppm). This was followed by constant closed-system recirculation of this environment through a purifier system, which enabled desiccation of the glovebox to below 10ppm of water content. In all dry nitrogen tribological tests, the water content was maintained below 300ppm.

The isolated effects of water on friction were studied in a 'humid nitrogen' environment, which was established by passing the 99.9998% dry nitrogen through a water bubbler. The humidified nitrogen gas with the desired water content was then introduced to the chamber. A dry air condition on the other hand was established by passing standard lab air through a silica gel desiccant before being introduced to the glovebox. As with dry nitrogen, the dry air water content of the glovebox was kept below 300ppm. Finally, standard lab air was passed into the glovebox to study the combined effects of oxygen and water.

Water content in any given environment was accurately measured using a combination of two instruments. Moisture content for low humidity conditions was measured using a trace moisture analyzer (GE VeriDri) between the range 10-2500 ppm. Moisture content above 2500ppm (~10% RH) in ambient conditions was measured with a hygrometer (Omega RH411). It is worth noting that water content measured in ppm may be converted to an equivalent value of relative humidity using the expression [92]

$$\frac{100}{RH} = \frac{e_s}{P} \cdot \left(1 + \frac{10^6}{ppm_v}\right)$$

Where RH is the relative humidity measured in per cent, P is the moist air pressure measured in millibar, e_s is the water saturation pressure in millibar and ppm_v is the

equivalent water content in parts per million by volume (ppm). For typical measurements, P=1013.5 millibar and e_s=29.6 millibar, at 25°C.

Energy Dispersive X-Ray Spectroscopy

Changes in surface chemistry and the contribution in particular of oxidation to MoS_2 lubrication were quantified using energy dispersive x-ray spectroscopy (EDS). EDS measurements were performed on a Zeiss Auriga 60 scanning electron microscope at a chamber pressure of 10^{-8} torr. The extent of oxide formation or removal at the sliding wear track is determined by comparing the value of oxygen Kα peak integrated over a region of interest (figure 24).

Low magnification SEM imaging (5X magnification) is first used to select three-to-five locations either inside or outside the wear track. These locations in low-magnification serve as fiducial markers for locating the same region during subsequent (post-anneal or post-roast) EDS measurements. At each of these locations, actual EDS maps are generated at high-magnification (10,000X). Reported values of O Kα in this work refer to the integrated counts generated by collecting an EDS maps over this high-magnification region. In order to facilitate direct comparison between different measurements and locations, the O Kα signal is integrated for 20 frames at an accelerating voltage of 1.5 keV for all scans. The low accelerating voltage value of 1.5 keV promotes surface sensitivity of the measurement, with the sample penetration depth estimated to be less than 30nm [93].

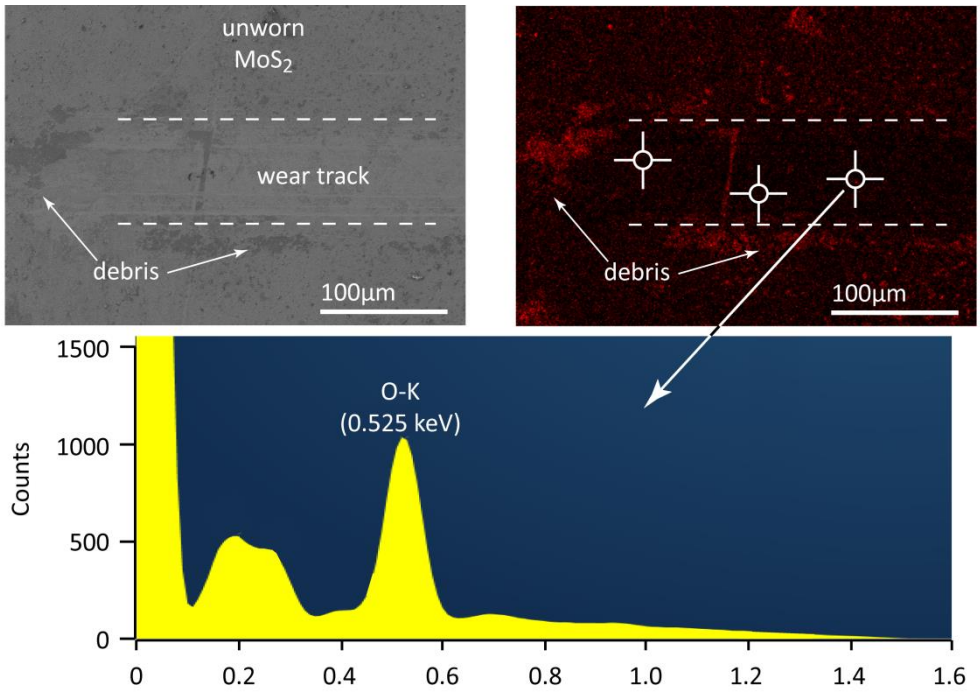

Figure 24 Illustration of the EDS measurement methodology. EDS spectra were generated from raster-scans at high magnification (10,000x), at several distinct fiducial locations within the wear scar. The value of the O Kα counts for each of these spectra was used to quantify the degree of surface oxidation.

Chapter 5

RESULTS

Effects of Environment and Temperature on MoS_2 Friction

Transient wear measurements were made in a nominally dry environment (moisture content less than 500ppm) and in standard lab air (50% RH). Interrupted images of the MoS_2 wear track were taken at 0, 1, 10, 50, 100, 500, 1000, and 5000 cycles using the method described earlier.

Representative profiles of the wear track cross-sections at different interruption intervals in dry and humid sliding are shown in figure 25. In all cases, track width is of the order of 100μm or smaller. In humid air sliding, observable wear begins at 100 cycles, with appreciable loss of volume occurring after 500 cycles. This increase in wear volume (depth of profile) occurs simultaneous with the lateral growth of wear track, indicated by the transverse separation distance between material pile-up. In contrast, observable wear in dry air sliding occurs only after 1000 cycles and wear depth and width is observed to be only a fraction of values in humid air. Interestingly, initial sliding in dry air causes a small but observable re-deposition of material within the wear track (most pronounced at 100 cycles), which is likely a consequence of debris consolidation during sliding. It is worth noting that the pile-up at the edge of the wear track consists of discrete fragments of debris, well outside the contact region, and is distinct from plastic deformation which is negligible for the sections shown.

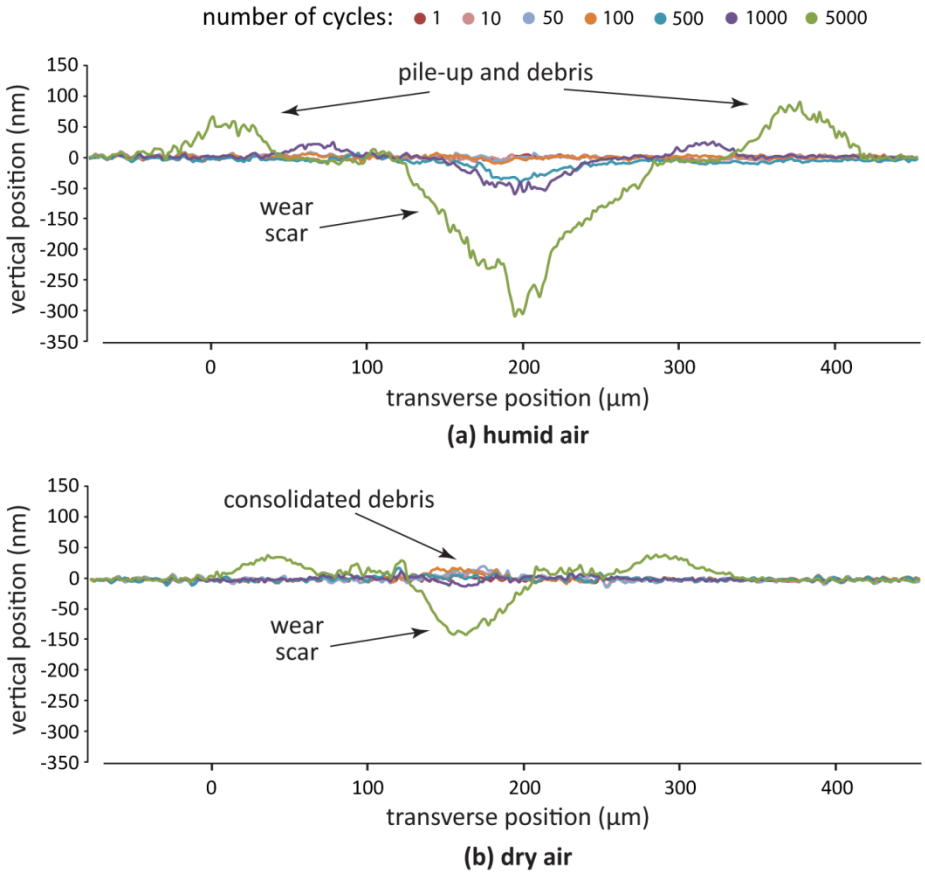

Figure 25 Cross-sectional wear profiles of MoS_2 sliding against a steel ball as a function of sliding cycles, obtained in (a) humid air (50%RH) and (b) dry air (<1% RH). Sliding in humid air creates deeper wear scars and more pronounced pile-up than dry air.

Three repeat experiments each in the two environments were conducted and mean values of wear volumes are reported in figure 26. Values of standard deviation for the repeat experiments were compared with the uncertainty of the technique (described in Chapter 4); the higher of two values is shown in figure 26 as error bars.

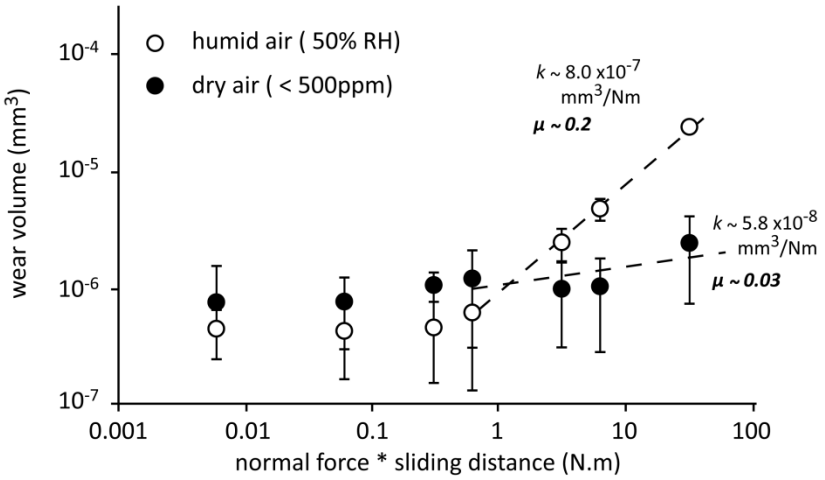

Figure 26 Wear volume of MoS_2 sliding in dry and humid air, plotted as a function of the product of normal load and sliding distance. Sliding in humid air yields steady state wear rates more than an order of magnitude higher than dry air. Interestingly, friction coefficient correlates with wear rate.

Wear rate (k) was evaluated using the expression in equation (5). As shown in figure 26, a low initial (<500 cycles) wear rate of MoS_2 is observed in both dry and humid environments. Although wear rate in humid air begin to increase after 500 cycles, the wear rate in dry air remains relatively low. Wear rate at the end of test were measured to be $8 \cdot 10^{-7}$ mm^3/Nm and $5.8 \cdot 10^{-8}$ mm^3/Nm in humid and dry air, respectively. As shown in figure 26, increasing wear in humid conditions increases the interfacial friction whereas low wear in dry conditions yield significantly lower friction coefficients. Friction coefficients can therefore be used as a metric for film condition, and will be used as an *in-situ* probe of interface conditions.

Friction coefficient of MoS_2 measured at ambient temperature in dry nitrogen, dry air, humid nitrogen and humid air are shown in figure 27. Each of the four

measurements in different environments was made by sliding a fresh steel ball against a fresh, unworn part of the MoS_2 coating.

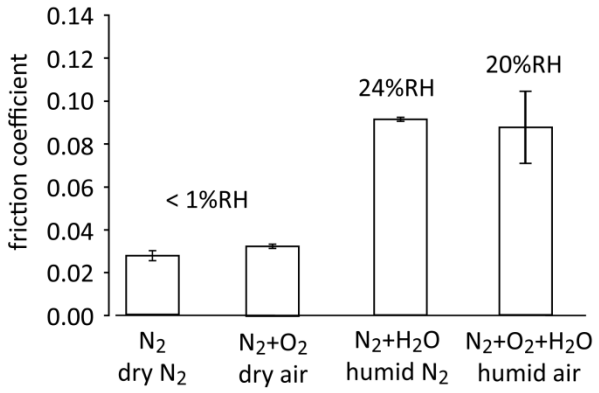

Figure 27 Steady friction coefficient of MoS_2 sliding in different environments at ambient temperature. Addition of oxygen to the sliding environment causes a negligible change in friction, although an increase in water partial pressure causes a commensurate increase in friction.

As shown in figure 27, a steady state friction coefficient of 0.027 ± 0.002 was observed in dry N_2. In dry air (N_2+O_2), a friction coefficient of 0.033 ± 0.001 was observed, suggesting that the additional oxygen in the sliding environment had a negligible effect on friction. On the other hand, the addition of water to dry N_2 in the absence of oxygen (i.e. humid nitrogen) causes friction to increase significantly to 0.09 ± 0.001. In the presence of environmental oxygen and water (humid air), a friction coefficient of 0.13 ± 0.002 was observed. The presence of oxygen in the sliding environment does not contribute to friction at room temperature, through oxidation or otherwise; the addition of water to the environment however causes a commensurate increase in friction (friction at 60% RH is higher than friction at 24%

RH), irrespective of the presence of oxygen. This result is consistent with the hypothesis that water impeded lamellar shear, either directly or through oxidation. It is consistent with the oxidation hypothesis only if oxidation is more likely in water than in oxygen.

General trends in the temperature-dependent friction for various environments are shown in figure 28. In dry nitrogen, very little effect of increasing temperature is seen on the value of friction coefficient up to 250°C. The friction coefficient of 0.027 increased to 0.050 with a temperature increase from 25°C to 250°C. In dry air, a low friction coefficient of 0.033 at room temperature increases steadily with temperature, reaching a value of 0.09 at 250°C. Since oxidation is thermally activated, this trend is consistent with increased friction due to oxidation.

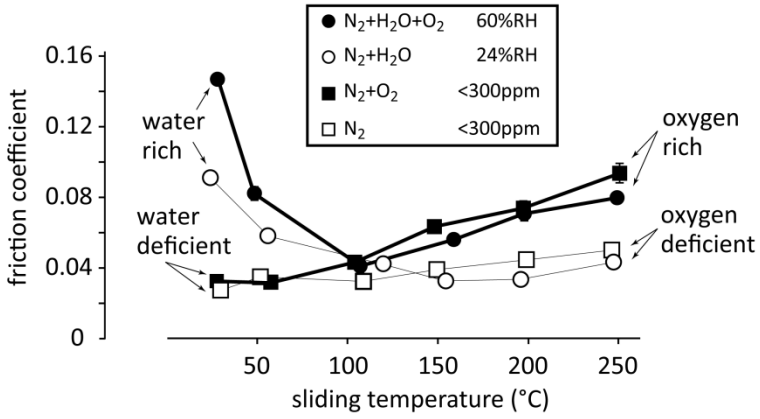

Figure 28 Temperature-dependent friction of conditioned MoS_2 in various environments. At ambient temperature, water drives the friction response of MoS_2 irrespective of the presence of oxygen. At elevated temperatures, friction increase with increasing oxygen and temperature. Transition for all environments occurred at 100°C.

For both humid air and humid nitrogen environments, a relatively high value of friction coefficient is observed at room temperature which decreased by over 50% as the temperature was increased to 100°C. This result is inconsistent with oxidation as a frictional driver and suggests thermally activated desiccation or slip. At higher temperatures, while the friction coefficient in the oxygen-deficient humid nitrogen remains low, the friction coefficient in an oxygen-rich humid air increases with temperature, similar to the temperature-dependent friction response in dry air. Among the four environments, it is worth noting that at ambient temperatures, water-rich environments witness the highest friction and at elevated temperatures, oxygen-rich environments show largest increases in friction.

Although oxidation is often cited as the key driver for ambient-temperature increase in MoS_2 friction, these results indicate that ambient-temperature friction is insensitive to the presence of oxygen in the sliding environment. Oxidation is a thermally activated process and yet, friction in a humid nitrogen environment reduced and then stays low with increasing temperature, which is suggestive of a thermally activated process not associated with oxidation. The possible contributions of thermally activated slip and desiccation in the observed results were investigated through controlled annealing experiments. Samples were heated in air but tested at room temperature; this test desiccates the sample but eliminates the possibility of thermally activated slip proposed by Hamilton *et al.* [59]. In this experiment, a 50-cycle friction measurement was made on an unworn MoS_2 coating with a fresh pin, at ambient temperature and in ambient (humid) air. After sliding, the MoS_2 coating was annealed at 50°C for 15 minutes and cooled to room temperature in the absence of sliding. A second 50-cycle friction measurement was then performed on the same

wear track. The coating was subsequently annealed at 75°C, 100°C, 150°C and 200°C, each for 20 minutes, with friction measured at room temperature for 50 cycles between successive anneals on the same wear track. The results of this fixed temperature annealing experiment are shown in figure 29(a). The friction coefficient at room temperature for pre-anneal sliding has a typical humid-air value of ~ 0.13. However, after the initial 50°C anneal, friction coefficient under identical sliding conditions (room temperature and 45% RH) is seen to reduce to ~ 0.12. Subsequent periods of annealing further reduce the friction coefficient to approximately 0.07. These results demonstrate that the friction reducing effect of temperature is partially or entirely due to thermally-activated desiccation. Interestingly, because adsorption is essentially instant on the time-scales of the experiments, the results suggest that the water content of the coating bulk is strongly influencing interfacial friction.

The results of this annealing experiment are compared to values obtained during sliding *at* a temperature of 200°C in figure 29 (b). During sliding at elevated temperature in the same environment (figure 29b), friction reaches an optimum and increases with increased temperature thereafter. The only thermally activated process we have considered that would be expected to increase friction is oxidation. Therefore, the results suggest that oxidation outcompetes desiccation at this temperature. This increase was only observed when oxygen was present and the results suggest that elevated temperatures in the presence of oxygen cause oxidation, which increases friction. Although both experiments witness a peak coating temperature of 200°C, only heating in the absence of sliding (annealing) results in the gradual reduction of friction. At steady state, friction is reduced in room temperature air if the coating is annealed before sliding despite the possibility of oxidation during annealing and

nearly instant adsorption of environmental water to the surface at room temperature, after annealing. The result is consistent with the removal of a surface oxide formed during exposure to high annealing temperatures in the presence of oxygen. Once removed, ambient temperatures are insufficient to restore the oxide layer and friction remains relatively low until sufficient time has passed to allow equilibration of the water content in the coating.

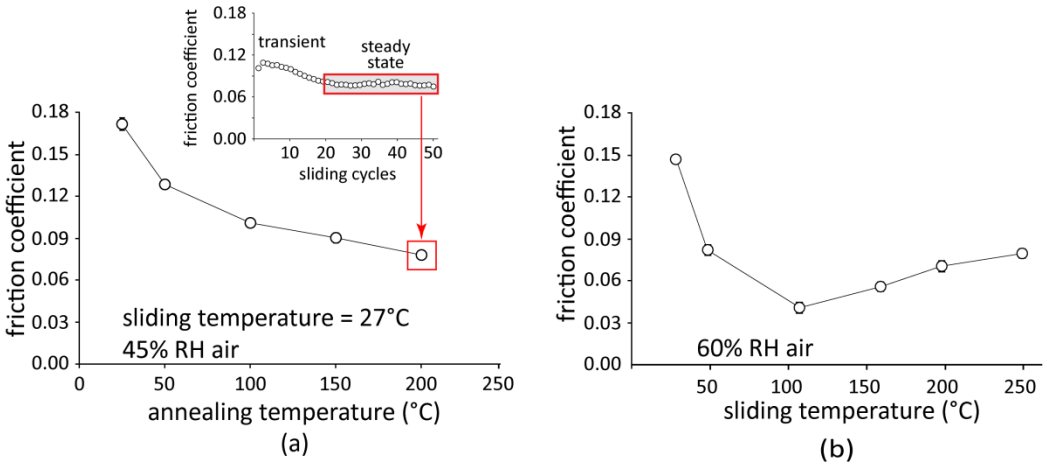

Figure 29 Results of annealing experiments conducted to elucidate the role of thermal conditioning. Annealing MoS_2 in the absence of high-temperature sliding, as in (a), results in a gradual decrease in friction. This contrasts with high friction obtained during sliding *at temperature*, as in (b). The gradual reduction in annealed MoS_2 friction is indicative of the role of thermal desiccation of coating sub-surface.

Friction data from Figures 28 and 29 indirectly suggest that oxygen is more likely than water to cause oxidation. EDS measurements were made to more directly determine the relative likelihood of oxidation as function of temperature in the presence of oxygen and water individually. A wear track was created by sliding 50

cycles to remove existing surface contamination, and the worn track was annealed first at 75°C and then at 250°C in each of dry air, dry nitrogen and humid nitrogen; a fresh wear track was created for each environment. The purpose of annealing was to accelerate oxidation, were it to occur in the given environment. EDS measurements at four locations were made prior to annealing, after annealing at 75°C and after annealing at 250°C; each of these three sets of measurements were made on the four nominally identical locations to enable a direct comparison driven entirely by the temperature and eliminate non-oxidative artifacts (such as surface heterogeneity). This procedure was repeated for each of the three environments.

The procedure for EDS measurements involved removing the coating from the control environment and inserting it in the SEM chamber (at ~ 10^{-8} torr), with the duration of ambient exposure no longer than 10 minutes. It must be stressed here that since EDS measurements are performed in high vacuum, the observed changes are necessarily due to non-volatile reaction products (oxides) on the surface, and not physically adsorbed water or oxygen. There results of these EDS measurements are shown in figure 30. In dry air, the extent of oxides increases with increasing annealing temperature, although a statistically significant increase in oxidation is observed only at 250°C ($p<0.05$). No evidence of oxidation is found in the case of the humid nitrogen environment; no change in the O Kα values is observed after annealing at 75°C or 250°C, indicating that oxygen and not water in the environment drives the formation of oxides, which is a thermally activated process. A similar insensitivity to annealing temperature of oxidation is expectedly seen for annealing in dry nitrogen.

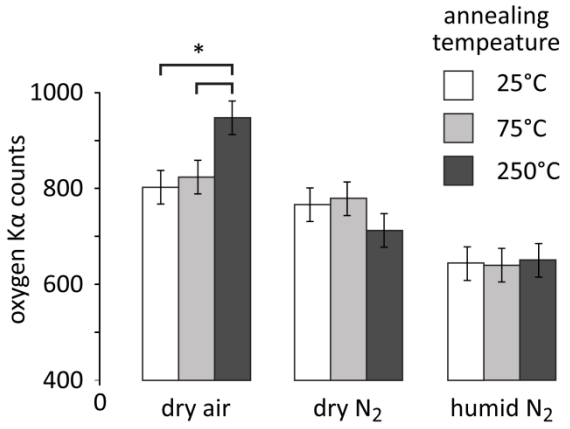

Figure 30 Mean values of O Kα counts as a function of annealing MoS_2 at different temperatures and in different environments. Only annealing in an oxygen-rich environment (dry air) led to an increase in surface oxides. No such increase is measured in a humid nitrogen environment. The asterisk represents a confidence interval with $p < 0.05$.

Examining the frictional transients in figure 29 (a, inset) reveals initially elevated friction consistent with results at temperature. The rapid reduction may be due to the removal of surface adsorbed water or oxides formed during annealing. EDS measurements following high temperature annealing confirm that oxygen, not water drives the formation of surface oxides of MoS_2 (figure 30). Of interest then is the effect these surface oxides have on the friction of MoS_2. To investigate this, a sliding friction measurement was made on a previously unworn MoS_2 coating in ambient humidity conditions (45% RH) and at ambient temperature. This MoS_2 coating was previously annealed to 250°C in humid air in addition to prolonged storage, in order to promote formation of surface oxides. An initial wear track 5mm long was created by sliding a single cycle; for cycles 2 and 3, the wear track length was reduced to 4.5mm, leaving 0.5mm of the original wear track unchanged. Similar decrements in wear track

length were made to yield 0.5mm segments of the total track which had ultimately experienced 1, 3, 5, 10, 15, 20, 30, 40, 50 and 100 sliding cycles (within a total track of 5mm). At the end of 100 cycles of sliding, the MoS_2 coating was transferred to the SEM for EDS analysis at the different segments of the 5mm track. EDS spectra were collected at multiple locations within each segment to verify repeatability. The friction coefficients and O Kα values corresponding to different sliding cycle segments are shown in figure 31.

The starting friction coefficient of 0.2 quickly drops to a steady-state value of 0.13 after the 25-cycle mark. Similarly, the EDS O Kα values within the wear track start at a high value of approximately 1200 counts for the unworn coating, dropping to a steady-state value of around 550 counts after the 25-cyle mark as well. The nearly identical trends in both friction coefficient and the O Kα counts with progressive sliding demonstrate that (1) oxides form at the surface of MoS_2 in the presence of oxygen and in this case, accelerated by annealing in dry air, (2) the extent of surface oxidation directly correlates to the interfacial friction coefficient and (3) wear progressively removes these oxides, lowering the friction. The correlation of transient friction coefficient with the oxide content is significant since it helps explain the contribution of non-volatile oxides, in addition to the adsorbed species to the often-observed phenomenon where the resumption of sliding after a brief pause in air results in a high value of friction which quickly drops with progressive sliding.

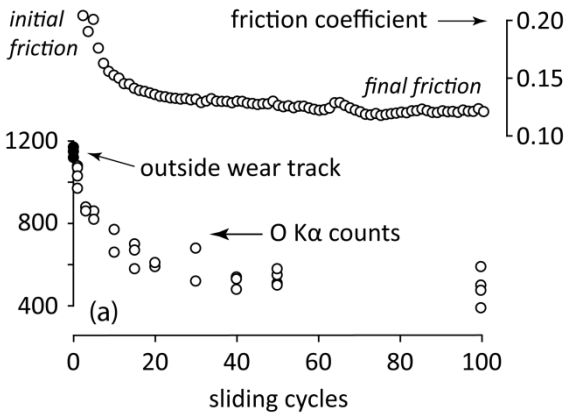

Figure 31 Values of friction coefficient as well as O Kα counts measured as a function of transient sliding cycles. A decrease in transient friction coefficient correlates with a decrease in measured surface oxygen, indicating that the removal of surface oxides due to wear results in a reduction in friction coefficient.

High temperatures promote surface oxidation as well as desiccation of bulk water, and subsequent sliding promotes the removal through wear of the surface oxides yielding a low, steady state friction even in humid conditions. Figure 32 shows results of two experiments in dry air which compare the competition between wear and oxidation. For the first experiment, friction was measured at room temperature after annealing at different temperatures for 15 minutes each in dry air. In the second experiment, friction was measured *at elevated temperature*, also in dry air. The order of temperatures was randomized to exclude artifacts of thermal history (shown by numerals 1-5 in figure 32). It is seen that post-anneal sliding shows a familiar reduction in friction, from a high initial to a low steady-state values typical of dry air. The friction coefficient measured at-temperature increases with increasing temperature; friction coefficient at 250°C is 0.1, almost four times its value at room temperature after annealing at 250°C.

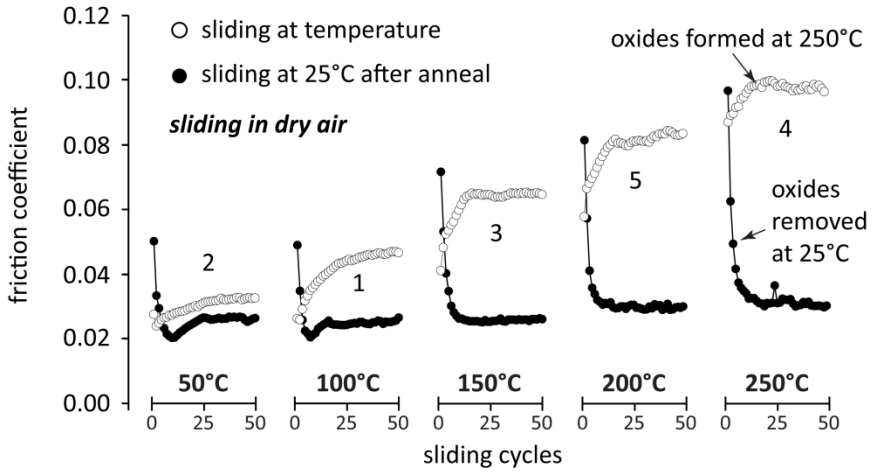

Figure 32 Results of friction measured in dry air as a function of annealing temperature as well as sliding temperature.

Interestingly, friction coefficient values obtained from high temperature sliding correlate not only with the sliding temperature, but also with the corresponding values of initial friction of the post-anneal test, at that temperature. These results reflect the direct competition between oxidation and wear – at elevated temperatures, the rate of oxide formation outpaces the rate of its removal, which is manifest in the sustained high friction (proportional to the surface temperature). At room temperature, wear of the previously formed oxide layer (during annealing) outpaces the negligible rates of ambient-temperature oxidation, yielding low steady state values of friction.

Annealing at elevated temperature in the presence of oxygen accelerates the process of surface oxidation, which is removed by wear. The effect of annealing temperature and environment were next studied by repeating the experiment in each of the four environments – dry nitrogen, humid nitrogen and humid air, in addition to dry air (resulting in four unique wear tracks). The results from this experiment are shown in figure 33.

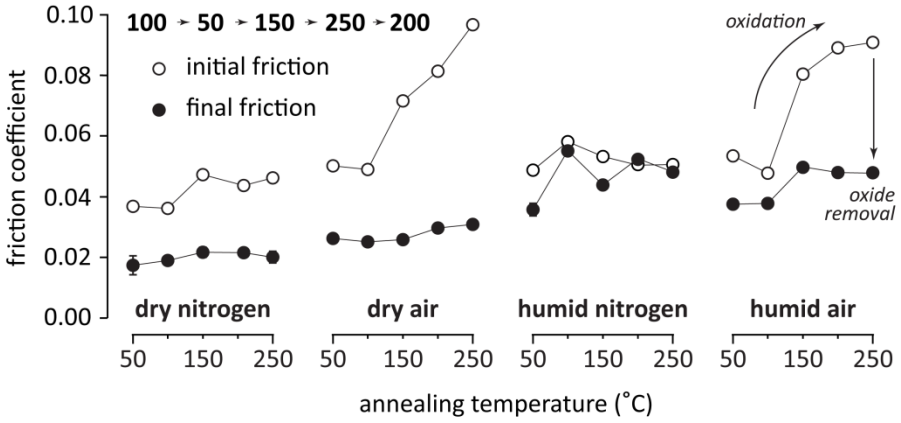

Figure 33 Results of annealing experiments performed to elucidate the effects of annealing temperature and environment on oxidation. Initial friction increases with temperature only in oxygen-rich environments, whereas final friction depends only on the presence of water in the environment. Low values of final friction, even in humid environments is attributed to thermal desiccation of MoS_2.

For the dry nitrogen environment, an initial friction of 0.04 ± 0.005 reduces to a final value of 0.02 ± 0.002 irrespective of annealing temperature. A similar range of initial to final friction decrease is seen for dry air, but only for 50°C and 100°C. At elevated temperatures, initial friction in dry air increases with increasing temperature although the final friction in dry air does not show any dependence on the annealing temperature. The increasing initial friction with temperature is indicative of greater surface oxidation; however this surface oxide is removed in all cases after sliding at room temperature. The trends in initial friction also confirm the absence of thermal history artifacts – the observed initial friction is directly driven by the annealing temperature and not the thermal history of the coating. In humid air, the trends in initial and final friction with temperature are similar to those in dry air; however the final friction in humid air shows a slight increase relative to dry air for all

temperatures. Lastly, annealing in humid nitrogen is observed to have no effect on the initial friction coefficient. The initial friction coefficient in humid N_2 is similar to initial values in dry N_2, final friction values in humid N_2 are similar to final values in humid air. Both initial and final friction coefficients in humid N_2 have a value of approximately 0.04. It is worth noting that the two environments which show an increase in initial friction with temperature both contain oxygen; the two environments with a lack of observable dependence of initial friction on temperature are those which lack oxygen. Furthermore, the two environments with marginally lower final friction are environments without water (dry air and nitrogen); both environments rich in water vapor show a higher final friction (humid air and nitrogen). These results show that (1) oxygen (not water) drives MoS_2 oxidation and the rates of oxidation are appreciable only at temperatures higher than 100°C (2) high temperature friction is governed by oxygen (and oxidation), while ambient temperature friction is affected by oxidation initially but, since oxides are rapidly worn away, these do not affect steady state friction which is driven solely by water (independent of oxidation). These results also reinforce the previous observation that surface oxide layers formed in the presence of oxygen are removed through sliding, leaving a 'clean' interface.

The experiments thus far have explored the individual effects of different environments and temperature on MoS_2 friction. There are numerous applications (for instance, space vehicle launch or re-entry), where humidity may vary along with temperature *during* operation. In such instances, the effects of humidity and thermal history become pertinent and are therefore explored next. The hypothesis that thermal and tribological conditioning affects transition to high friction was tested using variable humidity and temperature testing.

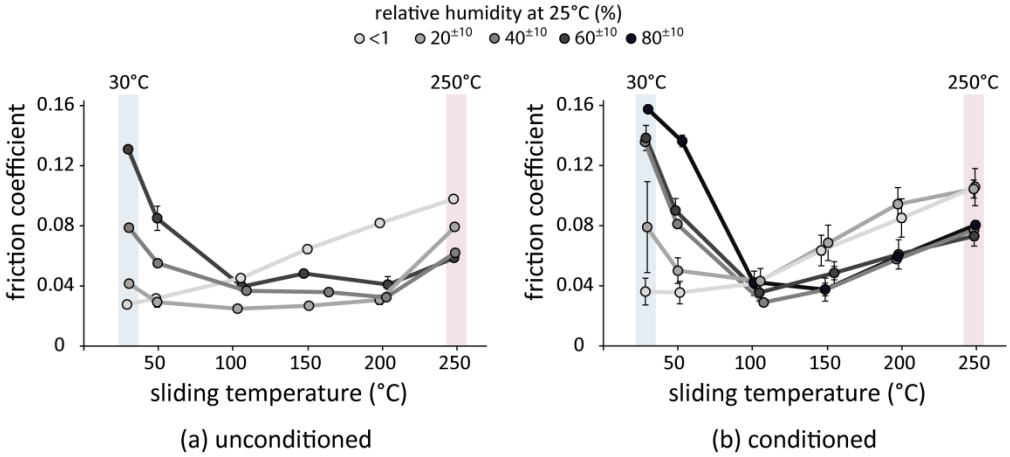

Figure 34 Friction coefficients of unconditioned and conditioned coatings plotted as a function of sliding temperature and humidity. Friction increases with humidity at ambient-temperature and decreases with increasing humidity at 250°C. For the unconditioned coating, transition occurs at 200°C whereas conditioned coatings transition at 100°C.

Temperature-dependent friction coefficients of conditioned and unconditioned coatings in different relative humidity environments are shown in figure 34. The results demonstrate two competing behaviors contribute to the environment and temperature-dependent friction of MoS_2. Interestingly, there is a transition temperature, presumably related to the onset of oxidation, where water-driven effects are replaced by oxidation-driven effects on friction. This temperature will be defined as the transition temperature. For both coatings at all values of humidity, friction coefficient initially reduces with temperature reaching a minimum at the transition temperature and increases with temperature thereafter. An exception to this trend is the sliding in dry air, where friction increases monotonically with temperature.

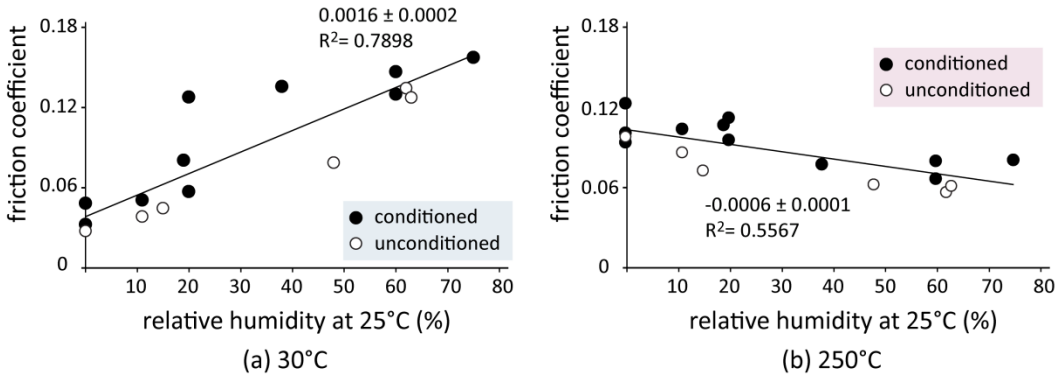

Figure 35 Temperature-dependent friction of conditioned and unconditioned coatings plotted as a function of humidity. At ambient temperature, friction for both coatings increases with humidity, although a saturation is observed for the conditioned coating at ~20%RH. At elevated temperature, friction *reduces* with increasing humidity, suggesting a masking effect of added moisture at these temperatures.

Furthermore, for both conditioned and unconditioned coating, the friction coefficient at any temperature before transition increases with increasing humidity whereas for temperatures higher than transition, friction coefficient is seen to *reduce* with increasing humidity. The trend of reducing friction with increasing humidity at elevated temperatures is contrary to the generally observed moisture-dependence of MoS_2 friction. The trends in friction with humidity for sliding at 30°C and 250°C for both conditioned and unconditioned coatings are shown in figure 35.

In practice, thermal conditions will also vary and these results suggest very specific frictional hysteretic effects. Thermal cycling experiments were conducted to test for consistency. To that extent, temperature-dependent friction was measured not only as the temperature increased (increasing rates of oxidation), but also as the temperature decreased (reducing oxidation rate). 50-cycle friction coefficients were measured from 25°C to 250°C (*ramp-up)*, and then to 25°C (*ramp-down)*. Friction

measured during a thermal ramp-up and ramp-down results in a frictional hysteresis loop, as illustrated in figure 36, with their width and orientation depending strongly on the environment. Frictional hysteresis loops from high-temperature sliding in different environments are shown in figure 36(a).

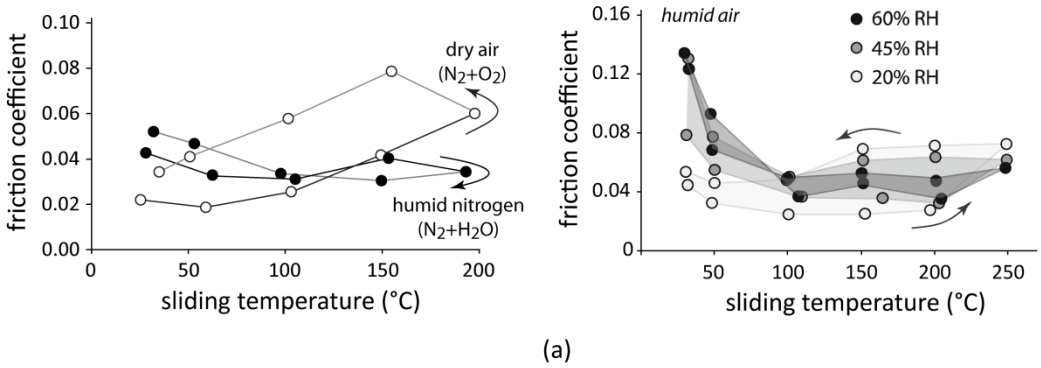

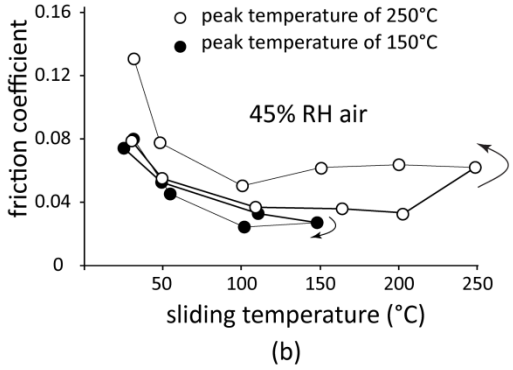

Figure 36 Frictional hysteresis during a thermal cycle (25°C-250°C-25°C), as a function of (a) sliding environment and (b) peak temperature. A strongly oxidizing environment results in a large hysteresis loop whereas increasing moisture reduces its magnitude. A reduction in peak temperature from 250°C to 150°C also reduces the magnitude of the hysteresis loop. These results suggest the contribution of residual oxides at the interface to the measured values of friction.

The dry air friction coefficient increases with temperature up till 250°C, as expected, but continues to increase even when the coating is cooled from 250°C to 200°C. The friction coefficient begins to decrease only when the coating temperature reaches below 150°C. Ramp-down friction coefficient is higher than the ramp-up friction coefficient for all temperatures, as shown. In contrast, thermal cycling in humid nitrogen results in the formation of a relatively narrow hysteresis loop, also shown in figure 36(a, left). More crucially, the friction coefficient *decreases* when the coating is cooled from 250°C to 200°C, and subsequent values at lower temperatures are comparable to values during ramp-up. The orientation and width of the dry air hysteresis loop suggests that high-temperature friction effects persist even after the coating begins to cool to lower temperatures, either due to residual oxidation or entrainment of oxide fragments.

With subsequent wear and reduced rates of oxidation at 150°C, the friction begins to decrease, although ramp-down friction is still higher than corresponding ramp-up friction in dry air. In contrast, the absence of oxidizing species in humid nitrogen result in low friction for all elevated temperatures; ambient friction is high due to the direct contributions of water. In the presence of both water and oxygen, synergies in the frictional hysteresis response are observed, as shown in figure 36(a, right). Although an increase in ramp-down friction relative to ramp-up friction is observed for all values of ambient relative humidity, the width of the hysteresis loop gradually reduces with increasing humidity. This suggests that while the increase in ramp-down friction, per se, relative to ramp-up friction is driven by the mere presence of oxygen, increasing moisture in the sliding environment suppresses the formation of oxides at higher temperatures, thereby causing a reduced *extent* of frictional increase

during ramp-down. A similar oxide suppression mechanism may be achieved if the surface temperatures are reversed before appreciable oxidation rates are realized. As shown in figure 36(b), even in an otherwise identical humid air environment, reversing surface temperatures after a peak value of 150°C results in a hysteresis loop reminiscent of sliding in humid-nitrogen. Comparing the hysteresis loops corresponding to peak temperatures of 250°C and 150°C, in figure 36(b), it is evident that reversal at 150°C prevents the formation of interfacial conditions which promote residual oxidation; hysteresis loops for thermal cycling in humid air till 150°C are similar to hysteresis loops generated in humid nitrogen with peak temperatures of 250°C. This observation is significant because although thermal conditioning and or elevated temperature may be used to reduce friction coefficients, this is limited due to the formation of irreversible interfacial products which result in an altered hysteresis response.

Role of Oriented Nanoscale Tribofilms

A key hypothesis in the lubrication of MoS_2 is that basally oriented nanoscale tribofilms drive its macroscale friction response. A typical friction experiment causes significant subsurface stresses that are thousands of times deeper than the extent of these films. It is therefore extremely difficult to probe their role in friction reduction. The stress-fields in an AFM measurement do not exceed the depth of these films. Therefore, single-asperity AFM contacts provide a unique opportunity to probe the influence of surface orientation and subsurface water content on MoS_2 friction. AFM-based measurements are uniquely suited to test the hypotheses that (1) nanoscale oriented tribo-films reduce friction (2) tribofilms approach the structure and function of single crystal MoS_2 (3) desiccation and oxidation affect nanoscale friction as they affect macroscale.

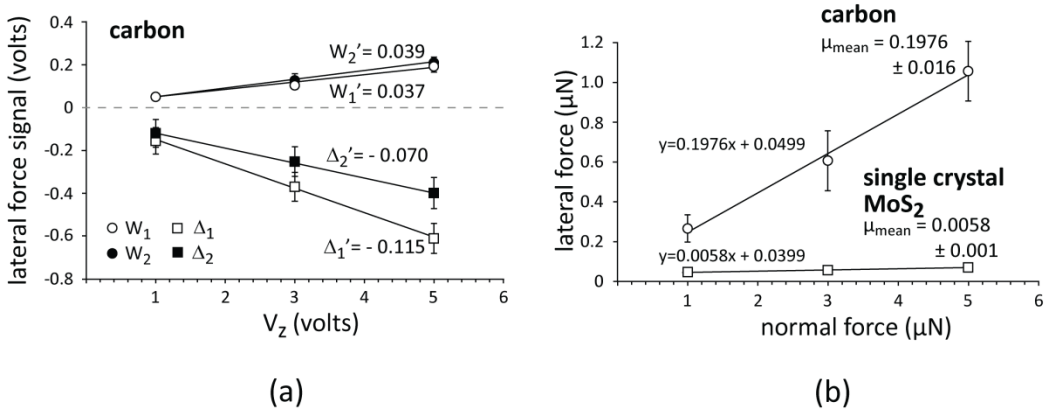

Figure 37 Raw and calibrated nanoscale friction measured on carbon and single crystal MoS_2, showing (a) the values of friction loop width and offset as a function of normal load, and (b) linear fits between calibrated friction and normal force for carbon and single crystal MoS_2, which yield friction coefficient.

Nanoscale friction measurements were performed on MoS_2 coatings in order to explore length-scale effects of desiccation and oxidation, and how these drive the macroscale tribology. Nanoscale friction measurements using the extended wedge method, developed in Chapter 4, and the Dimension AFM were initially performed on carbon and single crystal MoS_2 substrates, using integrated silicon probes. These measurements were performed under ambient humidity conditions on polished (Ra ~ 150nm) 99.999% graphite (from Kurt J. Lesker Co.), referred to as carbon, and cleaved (Ra < 1nm) single crystal MoS_2. The values of W' and Δ' at the two wedge angles for the carbon substrate are shown in figure 37(a).

As seen in figure 37(a), the two wedge angles yield values of 0.039 and 0.037 for W', indicating similar friction on both wedge angles. Error bars represent the standard deviation in the independent repeat measurements; statistical variation within a single measurement was typically an order of magnitude smaller. Negative friction loop offset slopes of -0.070 and -0.115 were obtained for both wedge angles with the carbon substrate. This trend is more similar to the misaligned microtribometer validation result, where both wedge angles gave similar slopes for loop offset (figure 22), than to either the aligned microtribometer or the original wedge method results (figures 16 and 22). Calibrated values of lateral and normal force on the carbon and single crystal substrates are shown in figure 37(b). Using a least squares linear fit, friction coefficients of 0.1976 and 0.0058 were obtained for the two substrates, respectively. The friction coefficient of single crystal MoS_2 in humid air is far below that of graphite despite general fact that humidity increases friction of MoS_2 and reduces friction of graphite

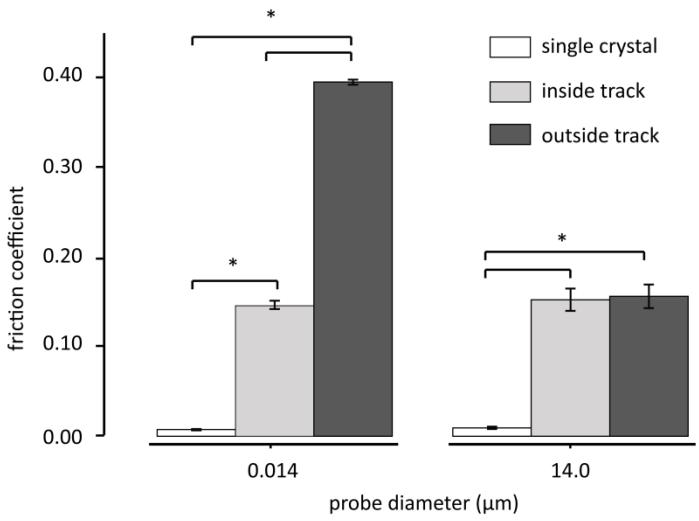

Figure 38 Nanoscale friction coefficient measured on worn and unworn sputtered MoS_2 coating, as a function of probe diameter. Small probe diameters show a statistically significant difference in friction on the worn and unworn coating, which is absent for the 14μm diameter probe. The asterisk represents a confidence interval with $p < 0.05$. Errors bars indicate standard error in the measurements, which were made at 25°C, in a 50% RH ambient environment.

Values of friction measured on worn and unworn MoS_2, and single crystal MoS_2 are shown in figure 38. Single crystal shows a significantly lower value of friction than sputtered MoS_2. Nanoscale friction measured within the wear track is significantly lower than friction measured on the unworn MoS_2 with an integrated 14nm probe. Measurements with this probe give high surface sensitivity and provide a direct evidence for the formation of friction-reducing oriented tribofilms in the wear track. It is worth noting that even with the formation of these tribofilms and the nearly 4X reduction in friction from 0.4 to 0.12, the friction coefficient of this oriented film is still an order of magnitude higher than friction coefficient of single crystal MoS_2.

Friction measured on worn and unworn sputtered MoS_2 coatings is also seen to show a strong dependence on tip diameter. Friction on the unworn coating measured with an integrated probe is observed to be significantly higher than friction within the wear track whereas unworn friction with a colloidal probe shows little difference from friction measured in the wear track with either probe. The differences in nanoscale friction as a result of different probe size is indicative of a distinct length-scale effects, likely driven by the differences in contact radii or interaction volumes activated by the differences in probe radii [77]. The nearly similar friction inside and outside the wear track with the larger probe suggests that the larger contact areas are able to cause microstructure reorientation *in-situ*. Furthermore, single crystal MoS_2 is observed to remain unaffected by these scaling artifacts, and represents the ideal low friction microstructure, which is only weakly approximated by the formation of oriented tribofilms in the wear track.

A similar scaling effect is observed in the effects of moisture on measured nanoscale friction. Contributions of bulk absorption and desiccation to the nanoscale friction of MoS_2 were investigated through controlled annealing. Annealing measurements involved heating the MoS_2 substrate to 110°C for 15 minutes. Friction with the AFM was measured both before and after annealing; values obtained with the integrated and colloidal probes were compared with those obtained at the macroscale with a ¼" diameter balls. Figure 39 shows results of these tests.

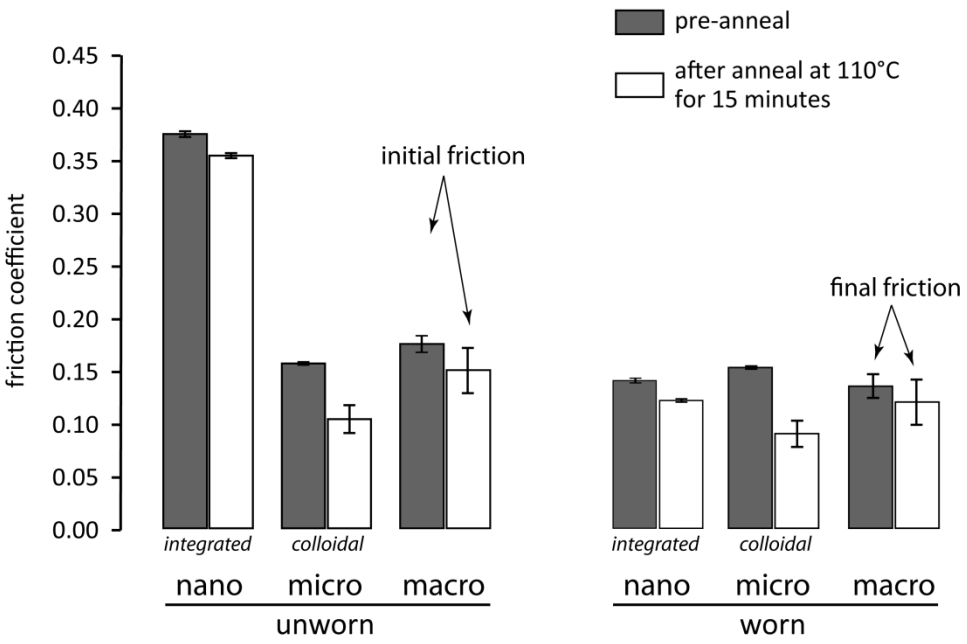

Figure 39 Friction coefficient measured as a function of coating thermal history, and scale of measurement. Nanoscale friction measured with an AFM and a colloidal probe show a reduction in friction for both unworn and worn MoS_2 coatings, similar to the decrease observed post-annealing in the macroscale friction measured with the HTT. No such decrease in post-annealing friction is however observed for the single crystal MoS_2. Friction was measured at 25°C, and in a 50% RH ambient environment.

On the unworn MoS_2, the integrated probe registers the largest friction coefficient of 0.40, which reduces to only 0.35 after annealing. In contrast, both the microscale colloidal probe and the macroscale ball register relatively low values of pre-annealing friction, which reduces after annealing. A similar decrease in the post-annealing friction coefficient relative to pre-anneal is observed for the integrated probe sliding on the worn surface. Friction on the wear track measured by the integrated probe reduces from 0.15 to 0.12, whereas friction measured by the colloidal probe reduces by almost the same extent as the macroscale friction. Using the maximum subsurface shear stress depth of a Hertzian contact as a first-order approximation of

the depth of subsurface interaction as a function of contact size scale, it is seen that the integrated nanoscale probe has an interaction depth less than 3 nm. This compares with an interaction depth of approximately 50 nm for the colloidal probe, whereas the interaction for macroscale contact encompasses the thickness of the coating. The high friction measured by the nanoscale probe on the unworn coating suggests sensitivity to surface oxides, which appear to be intrinsically high-friction. This value of friction is only marginally reduced due to annealing, which shows that even for this surface layer which would nominally experience instant water adsorption, the desiccation of the bulk is able to bias surface friction to a reduced value. The extent of frictional reduction post-annealing is higher for larger sized-probes, which is again suggestive of the increased effects of the desiccated bulk at those length-scales. Although these interaction depths demonstrate that the integrated probe has short-range interaction, the MoS_2 subsurface enables low friction not by bulk lamellar shear, but instead by acting as a sink for the near-surface moisture. Friction measurements on the worn and unworn coatings at different probe-scales confirm the role of oriented tribofilms as well as the surprising effect of bulk desiccation on nanoscale surface friction.

Chapter 6

DISCUSSION

The lubrication behavior of MoS_2 shows a complicated dependence on environmental constituents as well as temperature of the sliding interface, in addition to the effects of thermal and sliding history, and size-scale. Previous studies have hypothesized that water increases ambient-temperature friction by generating oxides of MoS_2, which inhibit easy lamellar shear. Other authors have suggested a range of other mechanisms, ranging from polar bonding to capillary condensation to physical and chemical adsorption, but these hypotheses have been dismissed in the favor of the other due to conflicting experimental observations. This comprehensive study explains the apparent contradiction, showing that direct physical interactions with water and oxidation strongly affect the tribology of MoS_2. The results show that these effects are competitive and depend on the conditions in a logical manner that is consistent with all of the results in the literature surveyed here.

Water is generally hypothesized to induce oxidation of MoS_2, however the results of this study refute this mechanism. Ambient temperature friction of MoS_2 in different environments reported in this work is consistent with trends which have already been reported in the literature. Similar low values of friction are observed in dry nitrogen and dry air, which increase proportionally with the extent of water saturation. At elevated temperatures however, the trends in lubricity are reversed and increasing water reduces friction in the presence of oxygen. The fact that water causes a breakdown of lubrication at ambient temperature while oxygen causes a breakdown

at elevated temperature sliding suggests the existence of distinct mechanisms of lubrication at different temperatures. Oxidation is a thermally activated process and an increase in friction with temperature in the presence of oxygen alone suggests that water does not participate in such oxidation. The role of oxygen in causing increased oxidation is further confirmed with EDS measurements of MoS_2 coating surfaces annealed alternatively in humid nitrogen and dry air. These EDS measurements provide direct evidence for the oxygen-driven oxidation of MoS_2 at elevated temperature and also show the inability of water to oxidize MoS_2 on its own. These chemical spectroscopy results are also consistent with high-temperature increases in friction which are observed for oxygen-rich environments, and are absent for environments lacking oxygen even in the presence of water.

Instead of the irreversible oxidation pathway, this study also confirms that the effect of water on MoS_2 friction is largely physical and reversible. Interestingly, the effects of water on ambient-temperature friction are composed of both a surface adsorption as well as a bulk-diffusive component. For coatings *annealed,* but not rubbed at elevated temperatures, room temperature friction measured in humid air after annealing is observed to reduce progressively with annealing. Annealing the MoS_2 coating in a given environment (with or without ambient oxygen and oxidation) results in the removal of water from the *bulk* of the coating, which results in drying of the MoS_2 coating. This desiccation of the bulk of the coating is distinctly different from the removal of water adsorbed to the surface. Surface adsorption occurs instantaneously with the introduction of atmospheric humidity and surface adsorbed water is removed equally instantaneous with the introduction of dry air or vacuum (such as in an SEM). Cooling an annealed MoS_2 coating in a humid environment

permits surface adsorption, however a frictional reduction after annealing is evidence that the desiccated bulk drives the friction response of annealed MoS_2 since diffusion of water back into this bulk occurs on much slower time-scales than surface adsorption.

In contrast to water, oxygen affects friction either through thermally-activated oxidation during sliding (at elevated temperature) or through remnant surface oxides formed during prior thermal cycling. The effects of the latter during room-temperature sliding on friction are limited to transient sliding. Oxides formed at elevated temperatures (in the presence necessarily of oxygen) are progressively removed with each sliding cycle when ambient-temperature sliding is imposed. The extent of surface oxides formed at high temperature and subsequently removed during transients is proportional to the sliding environment and the extent of thermal activation – oxidation increases in surplus oxygen with increasing temperature. Interestingly, the introduction of moisture at elevated temperatures actually *reduces* the ability of oxygen to oxidize MoS_2 and increase its friction. Given the lack of thermal-activation at room temperature, removal during transients reveals an unoxidized and desiccated MoS_2 coating which is able to sustain lower friction in nominally humid environments.

Guided by these observations, a model of MoS_2 lubrication is proposed, as illustrated in figure 40. In a typical MoS_2 coating, surface oxides form in the presence of oxygen, facilitated by longer exposure and higher temperature. Exposure to moisture does not cause oxidation, but causes diffusion of water into the bulk of the coating which increases with increasing partial pressure of atmospheric water as well as the exposure duration. At ambient temperatures, steady friction is driven by the

moisture content of the bulk (and to an extent of the environment) and not the oxide content at the surface. Annealing at high temperatures causes the desiccation of absorbed water. Annealing in the presence of oxygen however also leads to the formation of surface oxides. Sliding transients at ambient temperatures remove these surface oxides, leaving behind a nominally unoxidized surface as well as greatly desiccated subsurface, the combination of which yields low friction even in nominally humid air.

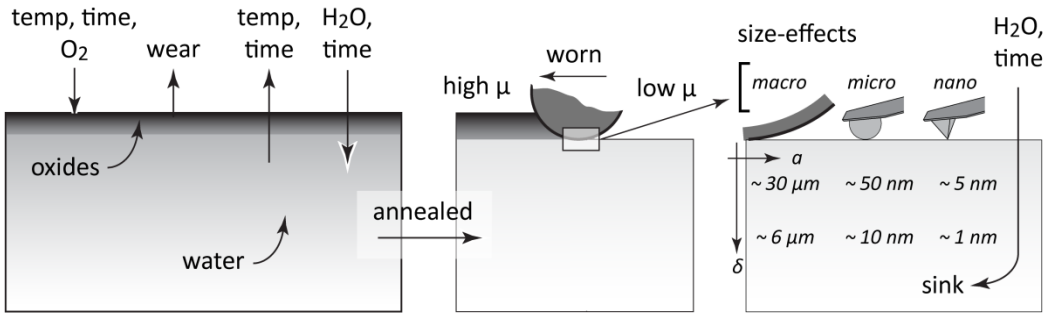

Figure 40 A schematic representation of the lubrication model of MoS_2. Increasing time and temperature in the presence of oxygen increases surface oxidation, but also increases desiccation of the bulk. In contrast, bulk diffusion of water increases with increased humidity and time. Annealing invariably removes this bulk water, and subsequent wear removes surface oxides yielding low values of steady friction.

At the most fundamental level, the macroscale friction of MoS_2 in response to the condition of its surface or sub-surface is driven by properties of its nanoscale tribofilms. Measurements of nanoscale friction with the AFM show a direct evidence for the formation of nanoscale tribofilms during macroscale sliding. These nanoscale tribofilms directly reduce macroscale friction within MoS_2 wear tracks by forming

highly oriented layers of MoS_2 lamellae. Friction measured on the *perfectly* ordered single crystal MoS_2 with the AFM was found to be almost an order of magnitude lower still. Single crystal MoS_2 represents the ideal microstructure for achieving low friction, however sliding induced grain reorientation on sputtered MoS_2 achieves only a fraction of the lubricity of this ideal microstructure. Interestingly, friction measurements of these tribofilms show a strong dependence on the nanoscale and microscale contact size. The higher friction on unworn MoS_2 for the integrated probe is likely driven by the shallow penetration volume, smaller contact radii and higher surface sensitivity, which in the case of the unworn surface probes a surface dominated by previously formed oxides. In the absence of a predominantly oxide-rich surface for the worn and annealing MoS_2 coating, the integrated probe is able to measure the intrinsic nanoscale friction of MoS_2 in humid air. In contrast, the larger contact radii of the colloidal and macroscale probes are more likely to activate a larger interaction area and volume, in addition to causing reorientation *in-situ*, given the lower values of friction.

Effects of bulk desiccation on the nanoscale friction are observed even at the small length-scales probed by the integrated probe which are indicative of the role of the desiccated bulk as a sink for moisture at the surface. Surprisingly, despite sliding in 50% RH humidity and with the smallest subsurface interaction volume, the integrated probe demonstrates significant reductions in nanoscale friction post-annealing. Nanoscale friction at this fundamental level is therefore driven by synergies between bulk desiccation and depending on the length-scales probes, *in-situ* microstructure orientation or high surface sensitivity driven by a shallow interaction volume. The effects of annealing become more pronounced with increase length-

scales, however increasing length-scales also introduces the possibility of *in-situ* grain reorientation, as noted earlier, which also leads to reduced friction.

The frictional behavior of MoS_2 at elevated temperatures differs significantly from the trend at ambient temperature. A key difference, as noted earlier, is that unlike ambient temperature, temperature-dependent friction of MoS_2 *increases* with the introduction of oxygen partial pressure and remains insensitive to the introduction of water partial pressure alone. Although seemingly contradictory, these trends in fact follow from observations of ambient behavior. It is necessary to recognize that elevated temperature induces oxidation of surface layers of MoS_2. In the absence of continued thermally-assisted oxidation, as in annealing experiments, sliding causes the removal of these surface oxides. During sliding *at-temperature,* the rate of oxide removal due to wear competes now with a positive rate of oxide formation due to thermal energy. The equivalence of these two processes is illustrated in figure 32, which compares the friction measured after annealing at specified temperature with friction measured during sliding at those temperatures. Interestingly, starting friction of annealed coatings is nearly identical to the steady state values of friction obtained during high-temperature sliding. At higher temperatures, rates of oxidation far outweigh the rates of their removal, which leads to increased friction. This mechanism explains why temperature-dependent friction of MoS_2 is much higher in dry air than humid nitrogen – the former promotes far more oxidation than the latter. When present together in the environment, moisture and oxygen work synergistically to affect the temperature-dependent friction of MoS_2. Interestingly, moisture at elevated temperatures acts to inhibit the ability of environmental oxygen to oxidize MoS_2. As

shown in figure 35, increasing the water partial pressure during high-temperature sliding reduces friction by reducing access of oxygen to reactive MoS_2 sites either through preferential adsorption or by displacing environmental oxygen.

Figures 28, 29 and 33 consistently suggest a transition temperature of 100°C. However, figures 34 and 36 shows a transition temperature of 200°C. Such stark differences have surprisingly been observed previously; for example, this is consistent with Kubart *et al.* who observed transition at 100°C, while a transition at 350°C was observed by Muratore *et al.* [56, 57]. Oxidation occurs at extremely high temperatures in some cases, and approaches practical operating temperatures in others. While it is difficult to trace the differences to anything specific in disparate studies, the observation of 100°C variation here allows controlled experimentation. The only identifiable difference between the experiments in figures 28-33 and 34 and 36, is the conditioning of the coating. Those experiments exhibiting 100°C transition temperature were conditioned (slid during thermal cycling). In figures 34 and 36, tests were conducted on fresh interfaces.

A primary distinguishing feature of the conditioned coating relative to the unconditioned coating is the presence of wear debris, transfer film and tribofilms at the sliding interface of the former. In order to elucidate the contribution of these third bodies to the variations in transition temperature, their morphological evolution at the ball surface was examined. Figure 41 shows optical micrographs of the transferred layers formed on the steel ball after sliding on the MoS_2 coating under various conditions.

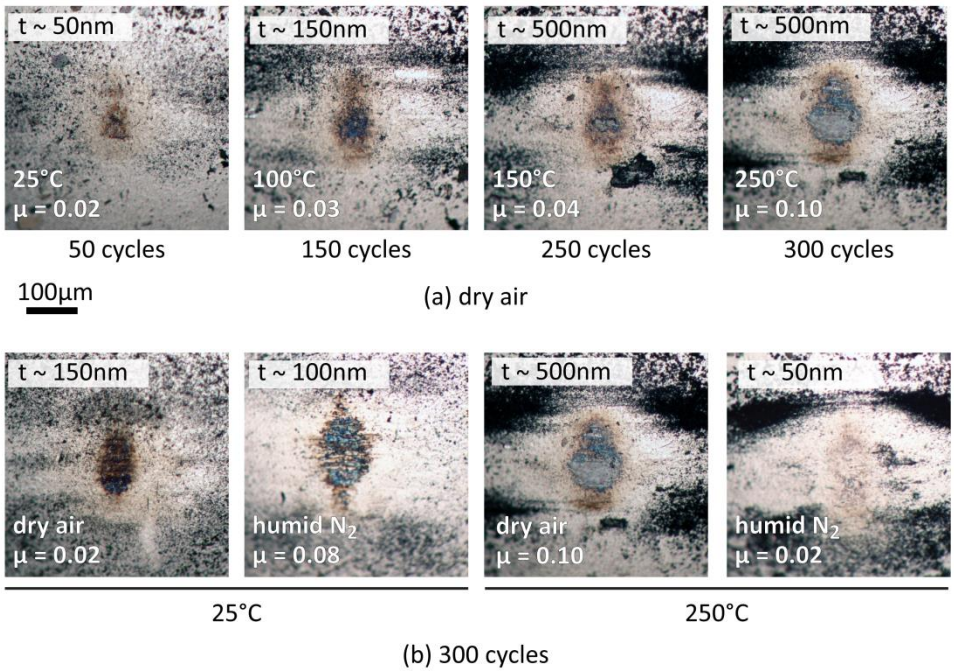

Figure 41 Morphology of transfer films formed on the steel ball sliding against an unconditioned coating (a) in dry air, at different temperatures (b) in dry air and humid nitrogen when sliding at 25°C and 250°C. Measured increases in friction correlate with increased coverage and thickness of oxide-rich transfer films.

All images shown in figure 41 correspond to a previously unworn interface (unconditioned coating).The progressive development of transfer film on the steel ball when sliding in dry air is shown in figure 41(a). It is seen that increasing interface temperature causes the development of a progressively thicker transfer film (blue) in addition to loose debris around the contact periphery (black). It is also evident that the increase in transfer film thickness and coverage correlates also with the increasing friction coefficient at the interface, as shown. Figure 41(b) shows a comparison of transfer films formed at 25°C and 250°C, in both dry air and humid nitrogen. As noted earlier, the thickness of transfer films correlates with increasing temperatures and

oxidizing environments. Sliding in the presence of oxygen, without water and at elevated temperatures causes the greatest increase in friction, consistent with the thickest films. In contrast, sliding in the presence of water but in the absence of oxygen leads to the formation of thinner films, which also correlates with lower friction.

Upon the initiation of high-temperature sliding in an oxygen-rich environment, friction is governed in equal measure by both the balance of oxide formation and removal, as well as its residence within the transfer films of the sliding ball. A positive correlation is found between the transfer film thickness and coverage, and the prevailing interfacial friction coefficient this transfer film represents (figure 41). The formation and adherence of these oxide-laden transfer films irreversibly alters the subsequent frictional characteristics of this interface. As an illustration, thick transfer films formed during thermal cycling in a conditioned coating result in quicker transition to higher friction with increasing temperature (figure 34). In fact, through parametric experiments, it was established that the presence of transfer films on the ball has a larger effect on driving the transition temperature from 200°C to 100°C, than sliding on preworn MoS_2 wear tracks (figure 42).

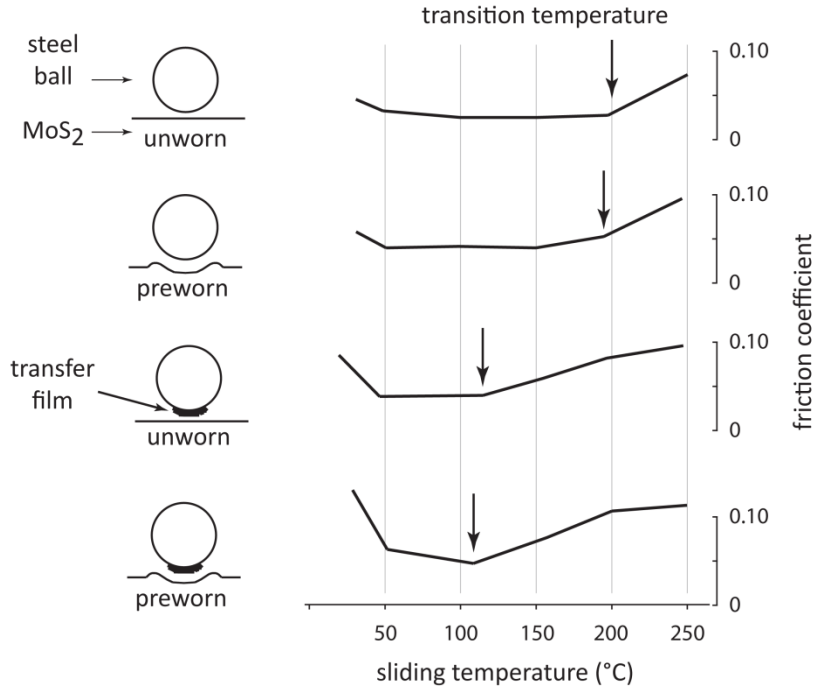

Figure 42 Contact schematic and corresponding trends of temperature-dependent friction in humid air, showing variations in transition temperature with the state of the interface.

In order to determine contributions of the coating microstructure to variations in transition temperature, temperature-dependent friction behavior of conditioned and unconditioned coatings was compared with measurements made with a control MoS_2 film. The control coating of virgin MoS_2 powder was prepared by approximating the 'excess layers' preparation method from Deacon and Goodman [29]; this coating is referred to as 'mechanically deposited' hereafter. This mechanically deposited coating was prepared from 98 % pure MoS_2 powder (McLube Co.), with nominal particle diameters ranging between 1 μm and 30 μm. A solution of MoS_2 powder was dispersed in ethanol by ultrasonication. The solution was then dripped onto a polished 440C steel substrate, and evaporation of the ethanol left a 20 μm thick MoS_2 coating

as measured with interferometry. The coating was consolidated to a thickness of approximately 1 μm after the initial sliding pass.

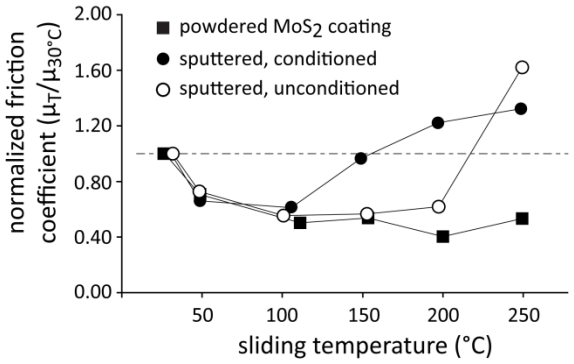

Figure 43 Friction coefficients of conditioned, unconditioned and powdered MoS_2 coatings as a function of sliding temperature. Friction coefficients have been normalized to their corresponding values at 30°C. A difference in transition temperature of the three coatings is driven by a combination of both the interfacial history and the microstructure.

Shown in figure 43, friction coefficient values for all coatings are normalized to their respective room-temperature friction coefficients to enable direct comparisons of their high-temperature behavior. The normalized friction coefficients of all three coatings are seen to be virtually identical up until a temperature of 100°C. While the conditioned and unconditioned coatings transition at 100°C and 200°C, the evaporated MoS_2 coating shows consistently low friction and did not transition at measured temperatures up until 250°C. These trends demonstrate that the transition temperature of MoS_2 coatings is strongly dependent on the condition of the interface and its microstructure.

Chapter 7

CLOSING REMARKS

A comprehensive study of lubrication mechanisms has been conducted in order to understand the contributions of moisture, oxygen, temperature, oxidation, wear and sliding thermal history and size effects to the frictional behavior of MoS_2. Following are the key findings of this work:

1. No evidence is found to support the notion that water oxidizes MoS_2 at ambient or elevated temperatures up to 250°C. The presence of oxygen in the environment is required to induce measurable oxidation at the MoS_2 surface and the rate of such oxidation increases with increasing temperature.

2. At ambient temperatures, MoS_2 friction is affected by both the environmental moisture (ambient humidity) through surface adsorption as well as the diffused moisture content of the coating bulk. Suitable annealing desiccates the MoS_2 coating, which allows for subsequent reductions in friction measured even in ambient humidity at room temperature.

3. Oxidation of MoS_2 is caused by oxygen alone. At ambient temperature, MoS_2 friction is unaffected by oxygen, whereas temperature-dependent MoS_2 friction is sensitive to oxygen and is generally reduced by increasing moisture. In the presence of oxygen, friction increases with temperature, with or without the presence of moisture in the sliding environment.

4. The contribution of MoS_2 oxides to friction at ambient temperature is limited to the first few cycles of sliding only. During this period, surface oxides (formed due to prior thermal cycling) are gradually removed due to wear. Transient wear exposes the nominally non-oxidized MoS_2 subsurface; measured friction on this surface responds only to the prevailing concentration of water in the bulk and the ambient.

5. During sliding at elevated temperature in the presence of oxygen, the rate of oxidation outpaces the rate of removal which leads to increased friction. At a given temperature (after transition), an increase in water partial pressure in the presence of oxygen causes a *reduction* in friction, possibly due to a masking by water against MoS_2 oxidation.

6. Transition to high friction at elevated temperature is a strong function of the contact history as well as coating microstructure. Interfaces which consist of transfer films (oxide-rich) formed during previous thermal cycles are observed to transition to high friction earlier than previously unworn interfaces.

7. AFM measurements show a strong evidence for frictional reduction as a result, at least in part, of the formation of sliding-induced tribofilms within the sliding wear tracks. A quantifiable decrease in nanosccale friction is measured in the wear tracks as a consequence of these tribofilms. Friction coefficients on the perfectly ordered single-crystal MoS_2 are still an order of magnitude lower than these values of worn friction coefficient.

8. Changes in the probe size directly influences the measured values of nanoscale friction, suggesting a strong dependence of friction on the contact length-scale. Although nanoscale probes achieved high surface sensitivity, friction coefficients measured by the micron-sized AFM probes were similar to the macoscale, suggesting the formation of tribofilms *in-situ* with these.

9. A reduction in friction is observed after annealing for both the nanoscale and microscale probes, suggesting a strong overriding effect of the desiccated bulk over surface adsorption in driving the friction response at these length-scales.

Design Considerations

Based on the findings of this study, the following attributes of MoS_2 solid lubrication are recognized for improving tribological performance and reliability of machine components:

1. Coating structure: As noted in the present study, the extent of diffused moisture plays a significant role in both the macroscale and nanoscale friction of MoS_2. Significant differences were also found between sputtered and single crystal MoS_2. Owing to the diffusive nature of moisture, it seems plausible that a control of coating density and microstructure would improve lubrication. Improving coating density or designing a microstructure which mimics single crystal MoS_2 can be expected to inhibit the diffusion of water into the bulk of the coating, thereby reducing the frictional sensitivity to water.

   Differences in the lubrication behavior are also observed between sputtered and mechanically deposited MoS_2 coatings. Sputter deposition is known to result in non-stoichiometric coatings ($MoS_{x<2}$); the effect of stoichiometry, and indeed other differences from a pristine compound that may arise during a vacuum-deposition process are equally pertinent aspects of MoS_2 coating design.

2. Thermal cycling: Temperatures below 100°C effectively dry the coating and resistive heating of the interface may be used prevent failure when operating in cool humid conditions as during terrestrial testing of satellites.

REFERENCES

1. Jost, H.P., *The Introduction of a New Technology, Report from the Committee on Tribology.* Her Majesty's Stationary Office, London, 1966.

2. Jost, H.P., *Tribology: How a word was coined 40 years ago.* Tribology and Lubrication Technology, 2006. **62**(3): p. 24-28.

3. Rabinowicz, E., *Friction and wear of materials*. 2nd ed. 1995, New York: Wiley. xv, 315 p.

4. Stachowiak, G.W., A.W. Batchelor, and Hazel M. Hussong Fund., *Engineering tribology*. 3rd ed. 2005, Amsterdam ; Boston: Elsevier Butterworth-Heinemann. xxiv, 801 p.

5. Bahadur, S., *The development of transfer layers and their role in polymer tribology.* Wear, 2000. **245**(1-2): p. 92-99.

6. Bahadur, S. and D. Tabor, *The wear of filled polytetrafluoroethylene.* Wear, 1984. **98**(0): p. 1-13.

7. Erdemir, A., *Genesis of superlow friction and wear in diamondlike carbon films.* Tribology International, 2004. **37**(11-12): p. 1005-1012.

8. Erdemir, A., et al., *Characterization of transfer layers on steel surfaces sliding against diamond-like hydrocarbon films in dry nitrogen.* Surface & Coatings Technology, 1995. **76-77**(1-3): p. 559-563.

9. Scharf, T.W. and I.L. Singer, *Role of third bodies in friction behavior of diamond-like nanocomposite coatings studied by in situ tribometry.* Tribology Transactions, 2002. **45**(3): p. 363-371.

10. Scharf, T.W. and I.L. Singer, *Monitoring transfer films and friction instabilities with in situ Raman tribometry.* Tribology Letters, 2003. **14**(1): p. 3-8.

11. Roberts, E.W., *Thin Solid Lubricant Films in Space.* Tribology International, 1990. **23**(2): p. 95-104.

12. Burris, D.L., et al., *Polymeric nanocomposites for tribological applications.* Macromolecular materials and engineering, 2007. **292**(4): p. 387-402.

13. Wahl, K.J. and W.G. Sawyer, *Observing Interfacial Sliding Processes in Solid-Solid Contacts.* Mrs Bulletin, 2008. **33**(12): p. 1159-1167.

14. Singer, I.L., et al., *Role of third bodies in friction and wear of protective coatings.* Journal of Vacuum Science & Technology A, 2003. **21**(5): p. S232-S240.

15. Dvorak, S.D., K.J. Wahl, and I.L. Singer, *In situ analysis of third body contributions to sliding friction of a Pb-Mo-S coating in dry and humid air.* Tribology Letters, 2007. **28**(3): p. 263-274.

16. Donnet, C., et al., *Super-low friction of MoS2 coatings in various environments.* Tribology International, 1996. **29**(2): p. 123-128.

17. Scharf, T.W., P.G. Kotula, and S.V. Prasad, *Friction and wear mechanisms in MoS2/Sb2O3/Au nanocomposite coatings.* Acta Materialia, 2010. **58**(12): p. 4100-4109.

18. Hu, J.J., et al., *Transmission electron microscopy analysis of Mo-W-S-Se film sliding contact obtained by using focused ion beam microscope and in situ microtribometer.* Tribology Letters, 2008. **32**(1): p. 49-57.

19. McCook, N.L., et al., *Wear resistant solid lubricant coating made from PTFE and epoxy.* Tribology Letters, 2005. **18**(1): p. 119-124.

20. Roberts, E.W., *Space tribology: its role in spacecraft mechanisms.* Journal of Physics D-Applied Physics, 2012. **45**(50).

21. Lancaster, J.K., *A Review of the Influence of Environmental Humidity and Water on Friction, Lubrication and Wear.* Tribology International, 1990. **23**(6): p. 371-389.

22. Miyoshi, K., *Solid Lubrication Fundamentals and Applications*. 2001: CRC Press. 416.

23. Yang, J.-F., et al., *Tribological properties of transition metal di-chalcogenide based lubricant coatings.* Frontiers of Materials Science, 2012. **6**(2): p. 116-127.

24. Lansdown, A.R., *Molybdenum disulphide lubrication*. 1st ed. Tribology series, 35. 1999, Amsterdam: Elsevier.

25. Spalvins, T., *A Review of Recent Advances in Solid Film Lubrication.* Journal of Vacuum Science & Technology a-Vacuum Surfaces and Films, 1987. **5**(2): p. 212-219.

26. Winer, W.O., *Molybdenum Disulfide as a Lubricant - a Review of Fundamental Knowledge.* Wear, 1967. **10**(6): p. 422-&.

27. Fleischauer, P.D., *Fundamental-Aspects of the Electronic-Structure, Materials Properties and Lubrication Performance of Sputtered Mos2 Films.* Thin Solid Films, 1987. **154**(1-2): p. 309-322.

28. Peterson, M.B. and R.L. Johnston, *Friction and Wear Investigation of Molybdenum Disulfide. I. Effect of Moisture.* NACA, Cleveland, OH, 1953.

29. Deacon, R.F. and J.F. Goodman, *Lubrication by Lamellar Solids.* Proceedings of the Royal Society of London Series a-Mathematical and Physical Sciences, 1958. **243**(1235): p. 464-482.

30. Bisson, E.E., et al., *Friction, wear, and surface damage of metals as affected by solid surface films.* NACA Report 1254, 1956: p. 91-111.

31. Midgley, J.W., *The Frictional Properties of Molybdenum Disulfide.* Journal of the Institute of Petroleum 1956. **42**: p. 312-315.

32. Pritchard, C. and J.W. Midgley, *The effect of humidity on the friction and life of unbonded molybdenum disulphide films.* Wear, 1969. **13**(1): p. 39-50.

33. Waghray, H., T.S. Lee, and B.J. Tatarchuk, *A study of the tribological and electrical properties of sputtered and burnished transition metal dichalcogenide films.* Surface & Coatings Technology, 1995. **76-77**(1-3): p. 415-420.

34. Renevier, N.M., et al., *Coating characteristics and tribological properties of sputter-deposited MoS2/metal composite coatings*

deposited by closed field unbalanced magnetron sputter ion plating. Surface & Coatings Technology, 2000. **127**(1): p. 24-37.

35. Roberts, E.W., *Towards an optimised sputtered MoS2 lubricant film.* Proceedings of the 20th Aerospace Mechanisms Symposium (co-sponsored by National Aeronautics and Space Administration, the California Institute of Technology and Lockheed Missles and Space Company, Inc.), 1986: p. 103-119.

36. Muratore, C. and A.A. Voevodin, *Control of molybdenum disulfide basal plane orientation during coating growth in pulsed magnetron sputtering discharges.* Thin Solid Films, 2009. **517**(19): p. 5605-5610.

37. Donnet, C. and A. Erdemir, *Historical developments and new trends in tribological and solid lubricant coatings.* Surface & Coatings Technology, 2004. **180**: p. 76-84.

38. Bolster, R.N., et al., *Preparation by Ion-Beam-Assisted Deposition, Analysis and Tribological Behavior of Mos2 Films.* Surface & Coatings Technology, 1991. **46**(2): p. 207-216.

39. Muratore, C. and A.A. Voevodin, *Chameleon Coatings: Adaptive Surfaces to Reduce Friction and Wear in Extreme Environments.* Annual Review of Materials Research, 2009. **39**: p. 297-324.

40. Martin, J.M., et al., *Superlubricity of Molybdenum-Disulfide.* Physical Review B, 1993. **48**(14): p. 10583-10586.

41. Ross, S. and A. Sussman, *Surface Oxidation of Molybdenum Disulfide.* Journal of Physical Chemistry, 1955. **59**(9): p. 889-892.

42. Haltner, A.J. and C.S. Oliver, *Effect of Water Vapor on Friction of Molybdenum Disulfide.* Industrial & Engineering Chemistry Fundamentals, 1966. **5**(3): p. 348-355.

43. Pardee, R.P., *Effect of Humidity on Low-Load Frictional Properties of a Bonded Solid Film Lubricant.* ASLE Transactions, 1972. **15**(2): p. 130-142.

44. Panitz, J.K.G., et al., *The Tribological Properties of Mos2 Coatings in Vacuum, Low Relative-Humidity, and High Relative-Humidity Environments.* Journal of Vacuum Science & Technology A-Vacuum Surfaces and Films, 1988. **6**(3): p. 1166-1170.

45. Stewart, T.B. and P.D. Fleischauer, *Chemistry of Sputtered Molybdenum-Disulfide Films.* Inorganic Chemistry, 1982. **21**(6): p. 2426-2431.

46. Fleischauer, P.D., *Effects of Crystallite Orientation on Environmental Stability and Lubrication Properties of Sputtered Mos2 Thin-Films.* ASLE Transactions, 1984. **27**(1): p. 82-88.

47. Dudder, G., et al., *Environmental Effects on the Tribology and Microstructure of MoS2-Sb2O3-C Films.* Tribology Letters, 2011. **42**(2): p. 203-213.

48. Johnston, R.R. and A.J.W. Moore, *Water Adsorption on Molybdenum Disulfide Containing Surface Contaminants.* Journal of Physical Chemistry, 1964. **68**(11): p. 3399-3406.

49. Holinski, R. and J. Gänsheimer, *A study of the lubricating mechanism of molybdenum disulfide.* Wear, 1972. **19**(3): p. 329-342.

50. Colbert, R.S., *The Role of Water on the Tribological Properties of Molybdenum Disulphide Films*, in *Mechanical and Aerospace Engineering*. 2012, University of Florida: Gainesville, FL. p. 117.

51. Voevodin, A.A. and J.S. Zabinski, *Laser surface texturing for adaptive solid lubrication.* Wear, 2006. **261**(11â€“12): p. 1285-1292.

52. Godfrey, N. and E.C. Nelson, *Oxidation Characteristics of Molybdenum Disulfide and Effect of Such Oxidation on its Role as a Solid Film Lubricant.* NACA TN No. 1882, 1949.

53. Sliney, H.E., *High-Temperature Solid Lubricants .1. Layer Lattice Compounds and Graphite.* Mechanical Engineering, 1974. **96**(2): p. 18-22.

54. Sliney, H.E., *Solid Lubricant Materials for High-Temperatures - a Review.* Tribology International, 1982. **15**(5): p. 303-315.

55. Sliney, H.E., *Decomposition kinetics of some solid lubricants determined by elevated temperature X-ray diffraction techniques.* Proceedings of the USAF Aerospace Fluids and Lubricants Conference, 1963: p. 350-367.

56. Muratore, C., et al., *In situ Raman spectroscopy for examination of high temperature tribological processes.* Wear, 2011. **270**(3-4): p. 140-145.

57. Kubart, T., et al., *Temperature dependence of tribological properties of MoS(2) and MoSe(2) coatings.* Surface & Coatings Technology, 2005. **193**(1-3): p. 230-233.

58. Kingsbury, E.P., *Solid Film Lubrication at High Temperature.* ASLE Transactions, 1958. **1**(1): p. 121-123.

59. Hamilton, M.A., et al., *A Possible Link Between Macroscopic Wear and Temperature Dependent Friction Behaviors of MoS(2) Coatings.* Tribology Letters, 2008. **32**(2): p. 91-98.

60. Bowden, F.P. and D. Tabor, *The area of contact between stationary and between moving surfaces.* Proceedings of the Royal Society of London Series a-Mathematical and Physical Sciences, 1939. **169**(A938): p. 0391-0413.

61. Archard, J.F., *Elastic Deformation and the Laws of Friction.* Proceedings of the Royal Society of London Series a-Mathematical and Physical Sciences, 1957. **243**(1233): p. 190-205.

62. Budynas, R. and K. Nisbett, *Shigley's Mechanical Engineering Design (Mcgraw-Hill Series in Mechanical Engineering)*. 2011: McGraw-Hill Science/Engineering/Math.

63. Tabor, D., *The physical meaning of indentation and scratch hardness.* British Journal of Applied Physics, 1956. **7**(5): p. 159-166.

64. Johnson, K.L., *Contact Mechanics*. 1985: Cambridge University Press.

65. Mann, A.B., *Nanomechanical Properties of Solid Surfaces and Thin Films*. Nanotribology and Nanomechanics: An Introduction. ed. B. Bhushan. 2005: Springer.

66. Bhushan, B., *Nanotribology and nanomechanics : an introduction*. 2008, Berlin: Springer. xxviii, 1148 p.

67. Prandtl, L., *Ein Gedankenmodell zur kinetischen Theorie der festen Körper.* ZAMM - Journal of Applied Mathematics and Mechanics / Zeitschrift für Angewandte Mathematik und Mechanik, 1928. **8**(2): p. 85-106.

68. Tomlinson, G.A., *A molecular theory of friction.* Philosophical Magazine, 1929. **7**(46): p. 905-939.

69. Popov, V.L. and J.A.T. Gray, *Prandtl-Tomlinson model: History and applications in friction, plasticity, and nanotechnologies.* Zamm-Zeitschrift Fur Angewandte Mathematik Und Mechanik, 2012. **92**(9): p. 683-708.

70. Mate, C.M., et al., *Atomic-Scale Friction of a Tungsten Tip on a Graphite Surface.* Physical Review Letters, 1987. **59**(17): p. 1942-1945.

71. Carpick, R.W. and M. Salmeron, *Scratching the surface: Fundamental investigations of tribology with atomic force microscopy.* Chemical Reviews, 1997. **97**(4): p. 1163-1194.

72. Belikov, S., et al., *Theoretical modelling and implementation of elastic modulus measurement at the nanoscale using atomic force microscope.* Proceedings of the International Conference on Nanoscience and Technology, 2007. **61**: p. 1303-1307.

73. Burnham, N.A. and R.J. Colton, *Measuring the Nanomechanical Properties and Surface Forces of Materials Using an Atomic Force Microscope.* Journal of Vacuum Science & Technology a-Vacuum Surfaces and Films, 1989. **7**(4): p. 2906-2913.

74. Butt, H.J., B. Cappella, and M. Kappl, *Force measurements with the atomic force microscope: Technique, interpretation and applications.* Surface Science Reports, 2005. **59**(1-6): p. 1-152.

75. Sansoz, F. and T. Gang, *A force-matching method for quantitative hardness measurements by atomic force microscopy with diamond-tipped sapphire cantilevers.* Ultramicroscopy, 2010. **111**(1): p. 11-19.

76. Bhushan, B., *Nano- to microscale wear and mechanical characterization using scanning probe microscopy.* Wear, 2001. **251**(1-12): p. 1105-1123.

77. Fischer-Cripps, A.C., *Nanoindentation*. 2002, New York: Springer. xx, 197 p.

78. Burris, D.L. and W.G. Sawyer, *Addressing Practical Challenges of Low Friction Coefficient Measurements.* Tribology Letters, 2009. **35**(1): p. 17-23.

79. Colbert, R.S., et al., *Uncertainty in Pin-on-Disk Wear Volume Measurements Using Surface Scanning Techniques.* Tribology Letters, 2011. **42**(1): p. 129-131.

80. Burris, D.L. and W.G. Sawyer, *Measurement Uncertainties in Wear Rates.* Tribology Letters, 2009. **36**(1): p. 81-87.

81. Munz, M., *Force calibration in lateral force microscopy: a review of the experimental methods.* Journal of Physics D-Applied Physics, 2010. **43**(6): p. 063001.

82. Green, C.P., et al., *Normal and torsional spring constants of atomic force microscope cantilevers.* Review of Scientific Instruments, 2004. **75**(6): p. 1988-1996.

83. Sader, J.E., J.W.M. Chon, and P. Mulvaney, *Calibration of rectangular atomic force microscope cantilevers.* Review of Scientific Instruments, 1999. **70**(10): p. 3967-3969.

84. Ogletree, D.F., R.W. Carpick, and M. Salmeron, *Calibration of frictional forces in atomic force microscopy.* Review of Scientific Instruments, 1996. **67**(9): p. 3298-3306.

85. Varenberg, M., I. Etsion, and G. Halperin, *An improved wedge calibration method for lateral force in atomic force microscopy.* Review of Scientific Instruments, 2003. **74**(7): p. 3362-3367.

86. Li, Q., K.S. Kim, and A. Rydberg, *Lateral force calibration of an atomic force microscope with a diamagnetic levitation spring system.* Review of Scientific Instruments, 2006. **77**(6).

87. Cannara, R.J., M. Eglin, and R.W. Carpick, *Lateral force calibration in atomic force microscopy: A new lateral force calibration method and general guidelines for optimization.* Review of Scientific Instruments, 2006. **77**(5): p. -.

88. ISO, *Guide to the Expression of Uncertainty in Measurements (Corrected and Reprinted in 1995)*. 1993.

89. Prunici, P. and P. Hess, *Quantitative characterization of crosstalk effects for friction force microscopy with scan-by-probe SPMs.* Ultramicroscopy, 2008. **108**(7): p. 642-645.

90. Michal, G., C. Lu, and A.K. Tieu, *Influence of force-based crosstalk on the 'wedge method' in lateral force microscopy.* Measurement Science & Technology, 2009. **20**(5): p. 055103.

91. Varenberg, M., I. Etsion, and G. Halperin, *Crosstalk problems in scanning-by-probe atomic force microscopy.* Review of Scientific Instruments, 2003. **74**(7): p. 3569-3571.

92. Spomer, L.A. and T.W. Tibbitts, *Humidity*, in *Plant Growth Chamber Handbook*, R.W. Langhans and T.W. Tibbitts, Editors. 1997, Iowa State University: Ames, IA. p. 43-64.

93. Kanaya, K. and S. Okayama, *Penetration and energy-loss theory of electrons in solid targets.* Journal of Physics D: Applied Physics, 1972. **5**(1): p. 43.

Appendix A

EXTENDED WEDGE METHOD VALIDATION DATA

Table 1 Control measurement, positive wedge angle

V_z (V)	0.2060 ± 0.0201	0.4296 ± 0.0200	0.6168 ± 0.0202	0.8004 ± 0.0200	0.9975 ± 0.0201
V_{xf} (V)	0.0274 ± 0.0030	0.0773 ± 0.0038	0.1100 ± 0.0040	0.1373 ± 0.0058	0.1846 ± 0.0041
V_{xr} (V)	-0.0121 ± 0.0030	-0.0318 ± 0.0041	-0.0462 ± 0.0093	-0.0568 ± 0.0064	-0.0744 ± 0.0040
Δ (V)	0.0076 ± 0.0021	0.0227 ± 0.0028	0.0319 ± 0.0051	0.0402 ± 0.0043	0.0551 ± 0.0028
W (V)	0.0198 ± 0.0021	0.0546 ± 0.0028	0.0781 ± 0.0051	0.0970 ± 0.0043	0.1295 ± 0.0028
θ (rad)	0.0568 ± 0.0001	0.0566 ± 0.0001	0.0564 ± 0.0001	0.0559 ± 0.0001	0.0556 ± 0.0001

Table 2 Control measurement, negative wedge angle

V_z	0.2004 ± 0.0197	0.3982 ± 0.0198	0.6154 ± 0.0195	0.8060 ± 0.0196	1.0007 ± 0.0195
V_{xf}	0.0115 ± 0.0038	0.0221 ± 0.0067	0.0329 ± 0.0092	0.0445 ± 0.0088	0.0584 ± 0.0106
V_{xr}	-0.0406 ± 0.0039	-0.0768 ± 0.0038	-0.1178 ± 0.0042	-0.1541 ± 0.0088	-0.1934 ± 0.0040
Δ	-0.0146 ± 0.0027	-0.0274 ± 0.0038	-0.0425 ± 0.0051	-0.0548 ± 0.0062	-0.0675 ± 0.0056
W	0.0261 ± 0.0027	0.0495 ± 0.0038	0.0753 ± 0.0051	0.0993 ± 0.0062	0.1295 ± 0.0056
θ (rad)	-0.0574 ± 0.0001	-0.0576 ± 0.0001	-0.0579 ± 0.0001	-0.0581 ± 0.0001	-0.0587 ± 0.0001

Table 3 Test measurement, positive wedge angle

V_z (V)	0.1896 ± 0.0186	0.4133 ± 0.0185	0.6083 ± 0.0188	0.8070 ± 0.0186	0.9914 ± 0.0185
V_{xf} (V)	0.1090 ± 0.0054	0.2315 ± 0.0053	0.3031 ± 0.0049	0.4544 ± 0.0051	0.5227 ± 0.0049
V_{xr} (V)	0.0489 ± 0.0044	0.1067 ± 0.0044	0.1405 ± 0.0038	0.2089 ± 0.0042	0.2360 ± 0.0039
Δ (V)	0.0790 ± 0.0035	0.1691 ± 0.0034	0.2218 ± 0.0031	0.3317 ± 0.0033	0.3793 ± 0.0031
W (V)	0.0301 ± 0.0035	0.0624 ± 0.0034	0.0813 ± 0.0031	0.1228 ± 0.0033	0.1433 ± 0.0031
θ (rad)	0.0572 ± 0.0002	0.0549 ± 0.0003	0.0523 ± 0.0002	0.0481 ± 0.0004	0.0444 ± 0.0003

Table 4 Test measurement, negative wedge angle

V_z (V)	0.2067 ± 0.0182	0.4146 ± 0.0181	0.6053 ± 0.0181	0.8100 ± 0.0179	1.0180 ± 0.0178
V_{xf} (V)	0.0896 ± 0.0048	0.1867 ± 0.0051	0.2515 ± 0.0050	0.3336 ± 0.0046	0.4113 ± 0.0042
V_{xr} (V)	0.0304 ± 0.0041	0.0637 ± 0.0044	0.0839 ± 0.0041	0.1118 ± 0.0040	0.1410 ± 0.0042
Δ (V)	0.0600 ± 0.0032	0.1252 ± 0.0034	0.1677 ± 0.0033	0.2227 ± 0.0031	0.2761 ± 0.0030
W (V)	0.0296 ± 0.0032	0.0615 ± 0.0034	0.0838 ± 0.0033	0.1109 ± 0.0031	0.1352 ± 0.0030
θ (rad)	-0.0584 ± 0.0001	-0.0603 ± 0.0001	-0.0622 ± 0.0002	-0.0647 ± 0.0003	-0.0663 ± 0.0004

Table 5 Extended wedge method processed data for microtribometer validation

	θ_1°	θ_2°	Δ_1'	Δ_2'	W_1'	W_2'
Control	0.056	-0.058	0.058	-0.066	0.134	0.124
Test	0.051	-0.062	0.382	0.263	0.144	0.129

Appendix B

REPRINT PERMISSION LETTERS

AIP PUBLISHING LLC LICENSE
TERMS AND CONDITIONS

Apr 02, 2014

All payments must be made in full to CCC. For payment instructions, please see information listed at the bottom of this form.

License Number	3360820799729
Order Date	Apr 02, 2014
Publisher	AIP Publishing LLC
Publication	Review of Scientific Instruments
Article Title	The extended wedge method: Atomic force microscope friction calibration for improved tolerance to instrument misalignments, tip offset, and blunt probes
Author	H. S. Khare,D. L. Burris
Online Publication Date	May 14, 2013
Volume number	84
Issue number	5
Type of Use	Thesis/Dissertation
Requestor type	Author (original article)
Format	Print and electronic
Portion	Figure/Table
Number of figures/tables	5
Title of your thesis / dissertation	The coupled effects of environmental composition, temperature and contact size-scale on the tribology of molybdenum disulfide
Expected completion date	May 2014

AIP PUBLISHING LLC LICENSE
TERMS AND CONDITIONS

Apr 02, 2014

All payments must be made in full to CCC. For payment instructions, please see information listed at the bottom of this form.

License Number	3360820877066
Order Date	Apr 02, 2014
Publisher	AIP Publishing LLC
Publication	Review of Scientific Instruments
Article Title	The extended wedge method: Atomic force microscope friction calibration for improved tolerance to instrument misalignments, tip offset, and blunt probes
Author	H. S. Khare,D. L. Burris
Online Publication Date	May 14, 2013
Volume number	84
Issue number	5
Type of Use	Thesis/Dissertation
Requestor type	Author (original article)
Format	Print and electronic
Portion	Excerpt (> 800 words)
Will you be translating?	No
Title of your thesis / dissertation	The coupled effects of environmental composition, temperature and contact size-scale on the tribology of molybdenum disulfide
Expected completion date	May 2014

SPRINGER LICENSE
TERMS AND CONDITIONS

Apr 02, 2014

This is a License Agreement between Harmandeep S Khare ("You") and Springer ("Springer") provided by Copyright Clearance Center ("CCC"). The license consists of your order details, the terms and conditions provided by Springer, and the payment terms and conditions.

All payments must be made in full to CCC. For payment instructions, please see information listed at the bottom of this form.

License Number	3360820985529
License date	Apr 02, 2014
Licensed content publisher	Springer
Licensed content publication	Tribology Letters
Licensed content title	The Effects of Environmental Water and Oxygen on the Temperature-Dependent Friction of Sputtered Molybdenum Disulfide
Licensed content author	H. S. Khare
Licensed content date	Jan 1, 2013
Volume number	52
Issue number	3
Type of Use	Thesis/Dissertation
Portion	Figures
Author of this Springer article	Yes and you are the sole author of the new work
Order reference number	
Original figure numbers	1-7
Title of your thesis / dissertation	The coupled effects of environmental composition, temperature and contact size-scale on the tribology of molybdenum disulfide
Expected completion date	May 2014

SPRINGER LICENSE
TERMS AND CONDITIONS

Apr 02, 2014

This is a License Agreement between Harmandeep S Khare ("You") and Springer ("Springer") provided by Copyright Clearance Center ("CCC"). The license consists of your order details, the terms and conditions provided by Springer, and the payment terms and conditions.

All payments must be made in full to CCC. For payment instructions, please see information listed at the bottom of this form.

License Number	3360780763699
License date	Apr 02, 2014
Licensed content publisher	Springer
Licensed content publication	Tribology Letters
Licensed content title	The Effects of Environmental Water and Oxygen on the Temperature-Dependent Friction of Sputtered Molybdenum Disulfide
Licensed content author	H. S. Khare
Licensed content date	Jan 1, 2013
Volume number	52
Issue number	3
Type of Use	Thesis/Dissertation
Portion	Excerpts
Author of this Springer article	Yes and you are the sole author of the new work
Order reference number	
Title of your thesis / dissertation	The coupled effects of environmental composition, temperature and contact size-scale on the tribology of molybdenum disulfide
Expected completion date	May 2014

SPRINGER LICENSE
TERMS AND CONDITIONS

Apr 02, 2014

This is a License Agreement between Harmandeep S Khare ("You") and Springer ("Springer") provided by Copyright Clearance Center ("CCC"). The license consists of your order details, the terms and conditions provided by Springer, and the payment terms and conditions.

All payments must be made in full to CCC. For payment instructions, please see information listed at the bottom of this form.

License Number	3360820427647
License date	Apr 02, 2014
Licensed content publisher	Springer
Licensed content publication	Tribology Letters
Licensed content title	Surface and Subsurface Contributions of Oxidation and Moisture to Room Temperature Friction of Molybdenum Disulfide
Licensed content author	H. S. Khare
Licensed content date	Jan 1, 2013
Volume number	53
Issue number	1
Type of Use	Thesis/Dissertation
Portion	Figures
Author of this Springer article	Yes and you are the sole author of the new work
Order reference number	
Original figure numbers	1-8
Title of your thesis / dissertation	The coupled effects of environmental composition, temperature and contact size-scale on the tribology of molybdenum disulfide
Expected completion date	May 2014

SPRINGER LICENSE
TERMS AND CONDITIONS

Apr 02, 2014

This is a License Agreement between Harmandeep S Khare ("You") and Springer ("Springer") provided by Copyright Clearance Center ("CCC"). The license consists of your order details, the terms and conditions provided by Springer, and the payment terms and conditions.

All payments must be made in full to CCC. For payment instructions, please see information listed at the bottom of this form.

License Number	3360820548263
License date	Apr 02, 2014
Licensed content publisher	Springer
Licensed content publication	Tribology Letters
Licensed content title	Surface and Subsurface Contributions of Oxidation and Moisture to Room Temperature Friction of Molybdenum Disulfide
Licensed content author	H. S. Khare
Licensed content date	Jan 1, 2013
Volume number	53
Issue number	1
Type of Use	Thesis/Dissertation
Portion	Excerpts
Author of this Springer article	Yes and you are the sole author of the new work
Order reference number	
Title of your thesis / dissertation	The coupled effects of environmental composition, temperature and contact size-scale on the tribology of molybdenum disulfide
Expected completion date	May 2014
Estimated size(pages)	142

CAMBRIDGE UNIVERSITY PRESS LICENSE
TERMS AND CONDITIONS

Apr 02, 2014

This is a License Agreement between Harmandeep S Khare ("You") and Cambridge University Press ("Cambridge University Press") provided by Copyright Clearance Center ("CCC"). The license consists of your order details, the terms and conditions provided by Cambridge University Press, and the payment terms and conditions.

License Number	3360821147492
License date	Apr 02, 2014
Licensed content publisher	Cambridge University Press
Licensed content publication	MRS Bulletin
Licensed content title	Observing Interfacial Sliding Processes in Solid–Solid Contacts
Licensed content author	Kathryn J. Wahl and W. Gregory Sawyer
Licensed content date	Jan 31, 2011
Volume number	33
Issue number	12
Start page	1159
End page	1167
Type of Use	Dissertation/Thesis
Requestor type	Author
Portion	Text extract
Number of pages requested	1
Territory for reuse	World
Title of your thesis / dissertation	The coupled effects of environmental composition, temperature and contact size-scale on the tribology of molybdenum disulfide
Expected completion date	May 2014

SPRINGER LICENSE
TERMS AND CONDITIONS

Apr 02, 2014

This is a License Agreement between Harmandeep S Khare ("You") and Springer ("Springer") provided by Copyright Clearance Center ("CCC"). The license consists of your order details, the terms and conditions provided by Springer, and the payment terms and conditions.

All payments must be made in full to CCC. For payment instructions, please see information listed at the bottom of this form.

License Number	3360821268327
License date	Apr 02, 2014
Licensed content publisher	Springer
Licensed content publication	Tribology Letters
Licensed content title	Transmission Electron Microscopy Analysis of Mo–W–S–Se Film Sliding Contact Obtained by Using Focused Ion Beam Microscope and In Situ Microtribometer
Licensed content author	J. J. Hu
Licensed content date	Jan 1, 2008
Volume number	32
Issue number	1
Type of Use	Thesis/Dissertation
Portion	Figures
Author of this Springer article	No
Order reference number	
Original figure numbers	10
Title of your thesis / dissertation	The coupled effects of environmental composition, temperature and contact size-scale on the tribology of molybdenum disulfide
Expected completion date	May 2014

AIP PUBLISHING LLC LICENSE
TERMS AND CONDITIONS

Apr 02, 2014

All payments must be made in full to CCC. For payment instructions, please see information listed at the bottom of this form.

License Number	3360821400033
Order Date	Apr 02, 2014
Publisher	AIP Publishing LLC
Publication	Review of Scientific Instruments
Article Title	Calibration of frictional forces in atomic force microscopy
Author	D. F. Ogletree,R. W. Carpick,M. Salmeron
Online Publication Date	Sep 1, 1996
Volume number	67
Issue number	9
Type of Use	Thesis/Dissertation
Requestor type	Student
Format	Print and electronic
Portion	Figure/Table
Number of figures/tables	1
Title of your thesis / dissertation	The coupled effects of environmental composition, temperature and contact size-scale on the tribology of molybdenum disulfide
Expected completion date	May 2014

Harman Khare <khare@udel.edu> Wed, Apr 2, 2014 at 10:28 AM

To: mathew.mate@hgst.com

Dear Dr. Mate,

I am a PhD student at the University of Delaware, working with Dr. David Burris on the tribology (and nanotribology) of molybdenum disulfide. I wish to use a figure from your 1987 paper in Physical Review Letters in the introduction to my dissertation.

Specifically, I would like to use figure 2 from your paper titled 'Atomic-Scale Friction of a Tungsten Tip on a Graphite Surface', which appears in PRL volume 59, which shows the atomic stick-slip on HOPG.

Could you please authorize the use of this figure in my dissertation, titled 'The coupled effects of environmental composition, temperature and contact size-scale on the tribology of molybdenum disulfide'?

Thank you,
Harman Khare

Mathew.Mate@hgst.com <Mathew.Mate@hgst.com> Wed, Apr 2, 2014 at 11:43 AM

To: Harman Khare <khare@udel.edu>

Dear Harman,

I am happy to authorize the use of this figure in your thesis. Good luck with your dissertation.

Warmest regards,
Mathew Mate

AMERICAN PHYSICAL SOCIETY
One Physics Ellipse, College Park, MD 20740 · http://www.aps.org

March 24, 2014

Harman Khare
PhD Candidate, Materials Tribology Laboratory
Department of Mechanical Engineering
University of Delaware, Newark, DE 19716

Ref # 26256

Thank you for your permission request dated Mar. 16, 2014. We are pleased to grant you a non-exclusive, non-transferable permission, English rights, limited to **print and electronic format**, provided you meet the criteria outlined below. Permission is for a one-time use and does not include permission for future editions, updates, databases, translations, or any other matters. Permission must be sought for each additional use. This permission does not include the right to modify APS material.

Please print the required copyright credit line on the first page that the material appears: "Reprinted (abstract/excerpt/figure) with permission from [FULL REFERENCE CITATION] as follows: authors names, journal title, volume number, page number and year of publication. Copyright (YEAR) by the American Physical Society.

The following language must appear somewhere on the website: "Readers may view, browse, and/or download material for temporary copying purposes only, provided these uses are for noncommercial personal purposes. Except as provided by law, this material may not be further reproduced, distributed, transmitted, modified, adapted, performed, displayed, published, or sold in whole or part, without prior written permission from the American Physical Society."

Provide a hyperlink from the reprinted APS material (the hyperlink may be embedded in the copyright credit line). APS's link manager technology makes it convenient and easy to provide links to individual articles in APS journals. For information, see: http://link.aps.org/.

You must also obtain permission from at least one of the authors for each separate work, if you haven't done so already. The author's name and address can be found on the first page of the published Article.

Use of the APS material must not imply any endorsement by the American Physical Society.

Permission is granted for use of the following APS material only:

- Fig. 2, Phys. Rev. Lett. 59, 1942 – Published 26 October 1987

Permission is limited to the single title specified of the publication as follows:
A thesis entitled "The coupled effects of environmental composition, temperature and contact size-scale on the tribology of molybdenum disulfide" to be published by the University of Delaware.

If you have any questions, please refer to the Copyright FAQ at: http://publish.aps.org/copyrightFAQ.html or send an email to assocpub@aps.org.

Sincerely,

Jamie L. Casey
Circulation and Fulfillment Assistant